ABSTRACT

Title of Dissertation:	COLD ATMOSPHERIC PRESSURE PLASMA SURFACE INTERACTIONS WITH POLYMER AND CATALYST MATERIALS
	Andrew Jay Knoll, Doctor of Philosophy, 2018
Dissertation directed by:	Professor Gottlieb S. Oehrlein, Department of Materials Science and Engineering

Cold atmospheric pressure plasma (CAP) is an excellent source of reactive species because they are able to produce these species cheaply, in a variety of configurations, and in a way that can be distributed easily but there needs to be more understanding of how they specifically interact with surfaces. The goals of this dissertation are to understand what the critical reactive species reaching a surface are for particular applications. As a first step we find that a plasma in direct electrical contact with a polymer material shows high etching rate and non-uniform treatment whereas a remote regime treatment can lead to a relatively uniform treatment over the exposed to plasma area. The interaction of vacuum ultraviolet (VUV) light with polymer surfaces was found to be critical under conditions where local oxygen is displaced by noble gas flow. This VUV flux is also dependent on plasma source type, being highest for high voltage sources using noble gas flow. For a surface microdischarge (SMD) source we

find high activation energy compared with atomic oxygen etching suggesting less reactive species reaching the surface are causing surface modification. However, for an atmospheric pressure plasma jet (APPJ) source we find that the activation energy changes over treatment distance, decreasing below the value expected for atomic oxygen as the jet gets closer to the surface. Additionally we find evidence of directional etching for the close distances which becomes less directional for further distance treatments suggesting we have a contribution from high energy species at closer distances despite there being no visible contact between the plasma plume and the polymer surface. Nickel catalyst materials interacting with plasma can be enhanced to show increased breakdown of methane and production of different product species such as CO compared to just the catalyst. This catalyst material also shows carbon deposition by CO and COO^- groups by plasma treatment, though increased plasma power and temperature can then remove these groups as well.

COLD ATMOSPHERIC PRESSURE PLASMA SURFACE INTERACTIONS WITH POLYMER AND CATALYST MATERIALS

by

Andrew Jay Knoll

Dissertation submitted to the Faculty of the Graduate School of the
University of Maryland, College Park, in partial fulfillment
of the requirements for the degree of
Doctor of Philosophy
2018

Advisory Committee:
Prof. Gottlieb S. Oehrlein, Department of Materials Science & Engineering, Chair
Prof. Robert M. Briber, Department of Materials Science & Engineering
Prof. Raymond Phaneuf, Department of Materials Science & Engineering
Prof. Lourdes G. Salamanca-Riba, Department of Materials Science & Engineering
Prof. Ray Sedwick, Department of Aerospace Engineering

Acknowledgements

I would primarily like to thank Dr. Gottlieb Oehrlein for being my mentor and working with me to teach me so much about research and the field of plasma science. I would like to thank the co-authors of my publications so far to date Pingshan Luan, Dr. Elliot Bartis, Martin Lai, Dr. Shiqiang Zhang, Dr. Nick Fox-Lyon, Connor Hart, Santosh Kondeti, Dr. Peter Bruggeman, and Dr. Raitses for without their help none of my work would have been possible. We also thank Dr. Dominik Metzler, Leith Shafi, Adam Pranda, Brandon Nguyen, Chen Li, and Thomas Dabrow for their helpful discussions, insights, and thoughts on this project over the years.

I would like to thank my dissertation committee for taking the time to go through the dissertation process with me. Your feedback and discussions of this work have helped advance it significantly. I hope that this work proves to be stimulating and to be at the level you would expect from a graduate student of this University.

I gratefully acknowledge the financial support by the US Department of Energy (DE-SC0001939 and DE-SC0005105) and National Science Foundation (PHY-1004256, PHY-1415353, and CBET-1703211).

I would like to dedicate this dissertation to my family Dr. Katie, Guinness, and Artemis whom without I would never have completed this long adventure of a dissertation process. I would also like to thank my parents Joanna and Jack for being understanding and support me unconditionally in my pursuit of education over my whole life. I would like to thank my grandfather Bud for being my inspiration as a lifelong college professor who also studied plasma physics for his dissertation.

Table of Contents

List of Figures & Tables

Chapter 1: Introduction

Cold atmospheric pressure plasma (CAP) sources are being applied to increasing numbers of applications due to their versatility and relative inexpensiveness compared to traditional plasma sources. Low temperature plasma at low pressures has long been a critical tool for the processing of industrial materials. While atmospheric pressure plasma has been around for many years for ozone production, but recently the development of jet style sources to be near ambient temperature has allowed expanse to new applications.[1] Plasma medicine[2,3,4] is a recently emerging field where plasma sources have been used for wound healing[5,6] and cancer treatments[7] to name a few applications. CAP sources have also been shown to be effective for surface decontamination[8] of hospital equipment which may serve as a replacement or supplement to autoclave technology and allow for disinfection of a wider range of hospital materials. More traditional plasma applications such as adhesion[9] and thin film deposition[10] have also been shown to be possible using CAP sources instead of low pressure plasma sources. Recent applications that are currently being explored are water decontamination treatment,[11] food sterilization,[12] and catalyst enhancement.[13] Despite the wealth of applications being studied, there is a lack of understanding of exactly which of these reactive species that are produced are important for causing the surface effects seen. This problem is further complicated by the number of different atmospheric pressure plasma sources that have been developed, each which may accomplish desired effects through different plasma surface interactions.

There are numerous applications that atmospheric pressure plasma can be applied to that this work will help contribute fundamental understanding to. The use of these

atmospheric pressure plasma sources in the biological and medical fields are particularly critical to completely understand as the health of the public is at stake and is one of the critical applications that the results of this research will be applied to. Particularly interesting is the treatment of medical equipment for sterilization and the treatment of human tissue. There have been several previous studies attempting to understand how atmospheric pressure plasma treatment accomplishes biological deactivation[14,15] as well as the comparison of these processes between atmospheric pressure and low pressure plasma.[16] The results of these experiments show that it is likely that species being introduced to the biological surfaces play a role in this biological deactivation.[17] This work is entirely conducted in the far effluent of the plasma so that there is no direct electrical contact but there is comparable work that treats polymers with the plasma plume in direct contact with the polymer surface.[18,19] It is unclear from this work then how plasma contact with the surface will change the plasma surface interaction and if there could be any potential damage from this contact. This would be important to understand if these sources are used on human tissue as any damaging condition would want to be avoided if possible.

Additionally, it is unclear how different plasma sources behave compared to one another. Indeed in these cited works and the literature as a whole use different plasma sources and show different effects on polymer surfaces which raises the critical question of the role of plasma source design on the effect of the plasma treatment. There are numerous design considerations which can cause significant changes to how plasma is created by a source and therefore how this source would affect a surface. The most obvious difference is the physical construction of the plasma source with emphasis on how the powered and grounded electrodes interact with one another, if they are in contact with the

plasma directly, and their relative shape to each other. This affects the type of plasma discharge distinguishing between corona type discharges, dielectric barrier discharges, and Townshend discharges. Other critical factors include the operating frequency and if this frequency is pulsed or continuous, the gas flow composition, and the electrical behavior of the plasma source. How these individual factors influence the plasma surface interactions will be discussed throughout this dissertation with respect to individual topics.

Medical applications of CAP treatment are quickly becoming a highly studied field but there are numerous applications that atmospheric pressure plasma is just starting to be applied to. One such potentially lucrative application is the enhancement of catalytic activity and efficiency by plasma treatment during catalysis.[20] Development of this technology could potentially improve the removal of volatile air contaminants,[21] growth of carbon nanostructures,[22] decomposition of methane into useful products[23,24] or for environmental health.[25] This field of study has demonstrated that plasma can help with catalysis however it not clearly understood how the plasma surface interactions are enhancing the catalytic behavior seen. By developing this understanding, specific plasma systems and treatment conditions could be designed to optimize this process.

1.1 Objectives

The objectives of this thesis are to further the understanding of how plasma treatments interact with various surfaces and determine what plasma produced species are critical to causing desired surface effects for desired applications. Previous work has shown a correlation between surface modification and biological deactivation for one source and species.[17] However, it is unclear if this is applicable to other plasma sources and if generally

surface modification or etching of material is more important for biological deactivation. One of the primary goals of this work is to determine what the primary reactive species for causing etching and surface modification by atmospheric pressure plasma in order to better understand this biological deactivation.

There is a clear disconnect in the literature between the treatment of surface by plasma where the plasma is in direct electrical contact compared with remote non contacting treatments. This may be critical as the effect of electric field, charged species, photon emission, and surface charging may be directly impacted by this change to name a few. Another goal of this work is to distinguish some of these effects and specifically compare these two treatment conditions. For remote treatment distances we expect that primarily reactive neutral chemical species to be the important species for surface modification and etching. However, we see drastic differences between source designs even when there is no direct electrical contact. This suggests that the surface interaction may be fundamentally different between these various sources. This work will further investigate this to determine the key reactive species produced by plasma for various surface effects.

Plasma catalysis is an emerging field of research and the fundamental mechanisms are not fully understood or measured. This application is an excellent opportunity to leverage the knowledge we have gained from studying plasma polymer surface interactions to the catalysis study. The final goal of this thesis will be to investigate how the surface catalysis processes are enhanced by the introduction of plasma produced species. Understanding these processes is critical for further implementation and commercialization of the plasma catalysis technology.

1.2 Description of Materials

The focus of the majority of this work is on thin polymer film materials. Polymers are an excellent material to study due to their common use in low pressure plasma processing for the semiconductor and other industries which provides a background to compare our plasma treatments to. Additionally, they can be directly related to many biologically related molecules which allows us to use polymers as a model material to study specific reactive groups instead of more complicated biological materials. There are many examples of literature of atmospheric pressure plasma treatment of biological systems where the results are unclear due to the complexity of the materials being treated.[26,27,28] For instance polystyrene has been previously studied by atmospheric pressure plasma treatment as both a commonly used industrial polymer and as a model for how plasma will affect styrene ring structures that may be present in biological molecules.[29]

A polymethyl methacrylate (PMMA)-based 193 nm photoresist (PR193) thin film polymer of 140 and 300 nm thickness and a polystyrene (PS)-based 248 nm photoresist (PR248) thin film polymer of 400 nm thickness were used for the majority of the polymer interaction studies. These polymers have the advantage of being well studied in low pressure plasma environments for industrial semiconductor applications and being sensitive to certain wavelengths of UV light. Additionally, these materials have been exposed to carefully controlled plasma exposures at low pressure of only long lived oxygen species and the activation energy has been measured for these conditions giving us a baseline of study for the activation energy studies at atmospheric pressure. Other supplemental materials used in this work include patterned wafers involving a stacked

structure of photoresist, Si-containing Anti-Reflective Coating (SiARC) hard mask, organic planarization layer (OPL), and tetraethyl orthosilicate to investigate etching directionality. SiO_2 films with 750 nm thickness were used to investigate thermal effects of plasma treatment.

Nickel catalysts supported on Al_2O_3 and SiO_2 are used for methane decomposition studies. Powder catalyst is pressed together into pellet shapes around a ceramic to hold it together for exposure under plasma treatment.

1.3 Plasma Treatment

Atmospheric pressure plasma jets (APPJs) are one type of plasma source that utilizes a noble gas flow to direct plasma and other reactive species to surfaces. Typically small amounts of reactive gas are added to these sources to create large fluxes of desired reactive species. These sources are particularly useful for a wide variety of applications due to their ability to produce reactive species while keeping the gas temperature near room temperature and the ability to produce reactive species without large surface damage due to ion bombardment. Another common style of plasma source is a dielectric barrier discharge (DBD) which often can operate in ambient air. Traditionally these sources have been used for ozone production[30] and can involve one or more dielectric barriers with a gap where the plasma is produced. However there are many variations on this source which can compact into single layer devices and others have a gas flow integrated to assist transport of species produced. There is some overlap between these two types of plasma sources as APPJ often involved one or more dielectric barriers, however the plasma discharge can behave very differently from source to source. There has been a significant

amount of literature dedicated to modeling reactive species and how their densities change with various plasma parameters of sources.[31,32] Additionally effort has been dedicated to measuring various species such as OH,[33] O_3,[34] O,[35] and high energy photons[36] for various plasma sources. These efforts often need to be adjusted for each different plasma source which means that a vast amount of characterization would be required to fully understand each plasma source being used currently. Our approach is that is we can determine the key surface interactions that are being caused universally by various plasma sources then we can focus the characterization needed for each plasma source and benefit the field as a whole. There are several unique plasma sources used in this work. Schematic diagrams of the plasma sources is available in chapter 3, Figure 3.1.

The first plasma source that was utilized in this work is a kHz driven ring-APPJ source. This source is based on a design by Teschke et al.[37] Two copper electrodes (20 mm length and 6.35 mm ID) are wrapped around a quartz tube (4 mm ID and 6.35 mm OD) and separated by a 1.6 cm thick Teflon block are driven by a variable frequency AC waveform power supply.

The second plasma source in this work is a kHz driven pin-APPJ source. A central pin electrode with a 1 mm diameter is mounted inside a quartz tube (1.5 mm ID and 3 mm OD) with a grounded copper ring electrode (20 mm length 3 mm ID) outside the tube. The same PVM500 power supply was used as for the other kHz sources with an AC waveform.

The third source used in this work is a MHz driven pin-APPJ source. This source was designed by Bruggeman *et al*. and has been extensively characterized.[38,32,39] The design uses a 1 mm diameter tungsten pin electrode mounted inside a quartz tube (1.5

mm ID and 3 mm OD) with a grounded copper ring electrode (5.3 mm length, 3 mm ID). Details of how the power was calculated for this source can be found in detailed work done previously.[40]

The final plasma source used in this work is a kHz driven surface microdischarge (SMD) source. The phase electrode is a 5 cm square copper plate, the ground electrode is a stainless steel mesh with 50% of opening, and a 1.6 mm-thick quartz plate dielectric separates these electrodes. The same PVM500 power supply was used as for the other kHz sources with an AC waveform.

Plasma heating of the substrate is a critical factor which can influence numerous surface reactions, species reaction rates, and can lead to damage of polymers at too high of temperatures. Therefore these plasma sources have been tested to determine the temperature rise caused by plasma treatment. The gas temperature caused by plasma heating has been studied for the MHz driven pin-APPJ in previous works and has been shown to start at room temperature moving up to ~600 K depending on the power of the discharge within the plasma area. However, heating of the substrate has been measured to show significantly lower temperatures. The temperature measured directly under a treated substrate of silicon by thermocouple was found to rise less than 20 K above room temperature for all plasma treatments at the standard treatment conditions used for experiments. Specifically, the SMD source was found to give a temperature increase of 9 K over a 10 minute treatment at 3 mm distance. The kHz driven ring-APPJ source was found to increase the temperature of the substrate by 3 K over a 10 minute treatment at 16 mm distance. The MHz driven pin-APPJ source showed the largest temperature increase of 11 K over a 10 minute treatment at 8 mm distance.

However, the most critical temperature for these experiments is the temperature of the very top of the surface that is being treated. This temperature is able to be measured using ellipsometry to monitor the thickness increase of a SiO_2 thin film on top of a silicon substrate.[41] We have previously found that SiO2 is stable under plasma treatment by the MHz plasma source at 8 mm distance under normal treatment conditions and the ellipsometric data shows thermal expansion of the SiO_2 followed by a return to the original starting point post treatment suggesting no effect occurring other than thermal expansion. Using this method we have calculated that for a 10 minute treatment of the same spot on a 750 nm SiO_2 film on Si at 8 mm distance with an Ar/O_2 plasma discharge at 2 W we see a temperature increase of approximately 16 K which is very similar to that of the temperature measured using the thermocouple directly below the sample. These conditions demonstrate the most extreme plasma treatment used in chapter 4 of this work except that for that work the plasma source is constantly moving to uniformly treat a larger area of sample leading to an even lower temperature increase. Additionally in chapter 4 the substrate uses a feedback loop to control the temperature of the substrate using the thermocouple located directly below the treated sample which we have shown here is similar to the actual value of the temperature of the top of the substrate. This means that the temperature controller of the substrate can account for some of this temperature increase by the plasma jet.

Atmospheric pressure plasma sources are mounted in a vacuum chamber in order to accurately control the ambient environment surrounding the plasma source. Characterization techniques are mounted on this chamber or connected with the chamber so that the treated samples can be moved without being exposed to room air. This

vacuum chamber can also be adjusted to add specific gas flows within the chamber, heating units, and diagnostics for the plasma.

1.4 Characterization Techniques

Characterization of plasma treated materials are the focus of this work, however some gas phase characterizations were also utilized. The primary characterization techniques used in this work are outlined in the following, though other techniques may have been used for limited measurements.

Ellipsometry

Ellipsometry was conducted in situ and ex situ using an automated rotating compensator SOFIE STE70 ellipsometer in the polarizer-compensator-sample-analyzer (PCSA) configuration using a He-Ne laser (λ = 632.8 nm) at a ~72° angle of incidence. The measurement of amplitude ratio after reflection (psi) and the difference in the phase shift (delta) are converted into film thickness and modification through multilayer optical modeling.

X-ray Photoelectron Spectroscopy (XPS)

XPS analysis was conducted to determine the surface chemistry of the thin film materials. The analysis was performed with a Vacuum Generators ESCA Mk II surface analysis system employing a Mg-Kα source (1253.6 eV) at electron takeoff angles of 90° (deep probing depth ≈ 8 nm) and 20° (shallow probing depth ≈ 2-3 nm) relative to the surface. The XPS system is directly connected to the chamber holding the plasma sources through a vacuum transfer system to allow for transfer without exposure to ambient air.

Fourier-Transform Infrared Spectroscopy (FTIR)

FTIR was used to obtain the chemical composition of the polymer bulk material. The material analysis is performed ex situ with a Shimadzu FTIR spectrometer. Additionally the plasma source may be integrated with the FTIR system to investigate the gas phase species produced. The FTIR system will also be utilized to measure the effectiveness of the plasma enhancement of the methane decomposition over the catalyst material. FTIR was also conducted in attenuated total reflection (ATR) mode. The ATR was performed using an internal reflection element of Ge crystal at 60° and the spectra were obtained using a wire-grid polarizer (at 270° angle) placed between the interferometer and the ATR cell. The absorbance spectra were collected at 4 cm^{-1} resolution over 500 cm^{-1} to 3000 cm^{-1} and averaged over 20 cycles.

FTIR was also used for the catalysis work for both gas phase and surface measurements. This setup uses a Shimadzu IR Tracer 100 unit with a custom made gas cell for gas phase measurements.

Diffuse Reflectance Fourier-Transform Infrared Spectroscopy (DRIFTs)

A DRIFTs unit made by Harrick Scientific Instruments was used for this work by the name of the Praying Mantis. In addition to the praying mantis DRIFTs unit, a high temperature reaction chamber (HVC-DRM-5) was used for temperature and environment control around the catalyst sample. The reaction chamber uses two KBr windows for IR light and has a 3rd viewport which was converted into ceramic piece integrating the plasma source into the reaction chamber dome.

Scanning Electron Microscopy (SEM)

SEM analysis was done to investigate damage done to polymer surfaces as well as to determine the directionality of etching for the patterned samples. The analysis was

performed on a Hitachi SU-70 Schottky field emission gun scanning electron microscope and was done at the Maryland NanoCenter AIMLab. The combination of top down and cross sectional images allows for analysis of 3 dimensional trench structures.

High Speed Photography

High speed photography was conducted of the plasma in order to determine the structure of the plasma discharge. A Phantom v7.3 camera was utilized which has a capability of 3 Gigapixel per second.

1.5 Thesis Outline

The goal of this thesis is to advance the understanding of the critical species that are produced by atmospheric pressure plasma sources interacting with surfaces. This is critical to be able to advance plasma applications in a directed manner and predict new applications for these plasma sources.

In Chapter 2, we investigate the difference in treating a surface with a directly coupled plasma treatment compared with a remote treatment where only reactive neutral species can interact with the surface. Additionally, we investigate how parameters such as feed gas chemistry and local gas environment around the plasma jet impact the polymer interaction. These findings motivated an investigation into the high energy photons to help explain the remote treatment results.

In Chapter 3, we investigate how VUV light is produced by various plasma sources and how it can have an impact on polymer surfaces at atmospheric pressure. We find that certain sources which have noble gas flow to operate in particular produce this light. We use computer modeling to investigate how the ambient air mixes with the plasma plume

gas chemistry to see how ambient oxygen impacts the gas at the plasma plume. We also investigate the difference that occurs when adding oxygen directly to the plasma feed gas.

In Chapter 4, a well-characterized polymer film at low pressure is used to calculate the activation energy of the etching process by APPJ treatment and SMD treatment. These sources operate in very different gas chemistries, discharge voltages, frequencies, and species produced. We find that there are critical changes to the APPJ activation energy of etching over distance of treatment which suggests a change in the dominant species causing etching over this distance change. The SMD however shows consistent activation energy with less reactive species. Additionally we investigate the directionality of etching for both of these sources by looking at 3 dimensional nano-scale structures etching in silicon.

In Chapter 5, we establish a methodology for investigating a plasma catalyst system for the decomposition of methane. We use FTIR to monitor the gas phase species produced by the catalyst and plasma reactions looking for CO, CO_2, and H_2O products as well as the reduction in methane. We also use a custom DRIFTs setup which has the APPJ plasma source integrated into it to monitor surface changes occurring *in situ* during the catalysis reaction. We can correlate the findings in the gas phase to the changes we see on the surface of the catalyst from plasma exposure to learn more about the cause of the plasma catalyst enhancement.

In Chapter 6, conclusions are made from this work and future directions are discussed.

Chapter 2: Real Time Characterization of Polymer Surface Modifications by an Atmospheric-Pressure Plasma Jet: Electrically Coupled Versus Remote Mode

A. J. Knoll[1], P. Luan[1], E. A. J. Bartis[1], C. Hart[1], Y. Raitses[2] and G. S. Oehrlein[1]

1. Department of Materials Science and Engineering and the Institute for Research in Electronics and Applied Materials, University of Maryland, College Park, Maryland 20742, USA

2. Princeton Plasma Physics Laboratory, Princeton, New Jersey 08540, USA

This work is published and can be found in full by the following citation: A. J. Knoll, P. Luan, E. A. J. Bartis, C. Hart, Y. Raitses and G. S. Oehrlein, Applied Physics Letters 105, 171601 (2014)

Abstract

We characterize and distinguish two regimes of atmospheric pressure plasma (APP) polymer interactions depending on whether the electrical interaction of the plasma plume with the surface is significant (coupled) or not (remote). When the plasma is coupled to the surface, localized energy deposition by charged species in filaments dominates the interactions with the surface and produces contained damaged areas with high etch rates that decrease rapidly with plasma source to-sample distance. For remote APP surface treatments, when only reactive neutral species interact with the surface, we established specific surface-chemical changes and very slow etching of polymer films. Remote

treatments appear uniform with etch rates that are highly sensitive to feed gas chemistry and APP source temperature.

2.1 Introduction

Atmospheric-pressure plasma sources have been increasingly investigated for a wide range of applications, from biological[14,8,42] to industrial surface treatments.[43,44] Here we distinguish two modes of APPJ operation depending on if the plume is coupled to the surface and charged species dominate versus remote treatments where reactive neutrals dominate. Previous work on APPJ surface interaction has not systematically distinguished between the two interaction modes described here, despite substantial difference in the physical mechanisms, and have primarily been investigated post-treatment through methods such as biological deactivation,[45] water contact angle,[46] atomic force microscopy,[47] Fourier transform infrared spectroscopy,[48] and profilometry.[49] In this work we use a combination of *in situ* techniques including real time ellipsometry and high speed photography with post characterization techniques. We find that APP source/sample geometry, feed gas and environmental chemistry, and APP source temperature play important roles in determining the consequences of the APP-surface interactions.

2.2 Experiments and Methods

The plasma source used in this work has been described previously[14] and is based on the design by Teschke et al. called an atmospheric-pressure plasma jet (APPJ).[37] A diagram of the experimental setup is shown in Fig. 2.1(a). The plasma source consists of

two 20 mm long cylindrical copper electrodes separated by a 12 mm thick Teflon block around a 6.35 mm outer diameter, 3.7 mm inner diameter alumina tube through which 2 lpm Ar gas was flowed with or without 1% O_2 or N_2 admixtures. The plasma was generated using a high voltage power generator driven at 25 kHz. Applied voltage and voltage across measurement capacitor was monitored by using a Tektronix P6015A high voltage probe connected to a Hewlett-Packard 400 MHz oscilloscope. Power dissipated by the plasma was calculated using the Lissajous method using a 1 nF measurement capacitor (C_m).[50,51] High speed photography of the APPJ was taken using a Phantom v7.3 camera. An ellipsometer utilizing a 1.5 mW HeNe laser at 632.8 nm was used to non-invasively investigate thickness and index changes extracted through optical modeling of the ellipsometric data. Surface chemistry analysis by XPS was performed by a Vacuum Generators ESCALAB MK II surface analysis system post treatment. Surface morphology was imaged post treatment using a Hitachi SU-70 Analytical scanning electron microscopy (SEM) and through differential interference contrast microscopy. The surface studied was a 300 nm thick PMMA-based 193 nm photoresist polymer (PR193) film described previously.[17]

2.3 Results and Discussion

Figure 2.1(a) displays the two APPJ modes of operation. For the remote treatment mode, the plasma is generated with source to nozzle distance (s_n) of 15 cm and nozzle to sample distance (s_s) of 1 cm to ensure no direct electrical interaction. Plasma coupling mode is evident by filaments visually terminating at the film surface and occurs at combined distances closer than 15 cm, depending on gas chemistry and whether the

plasma is confined within the tube (small s_n) or exposed to the ambient (small s_s). The setup also allows for the addition of a removable, electrically insulating shield between the plasma and sample (not shown).

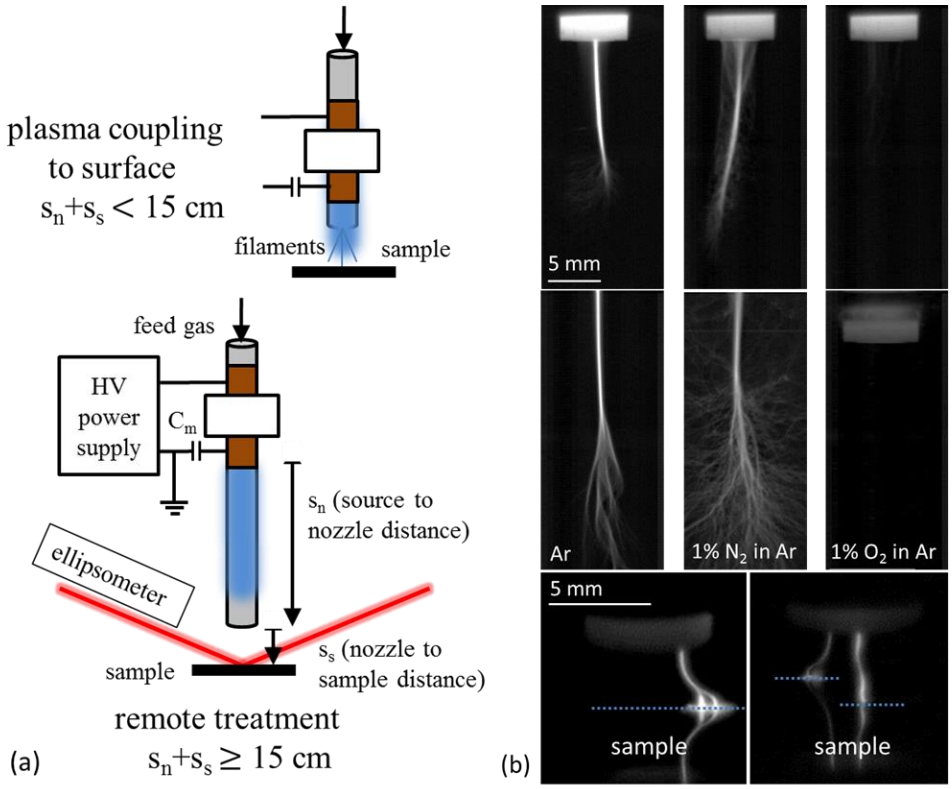

Figure 2.1: (a) Experimental setup showing two distinct operational modes: remote and closely-coupled. Plasma jet can also be exposed to ambient or confined within the dielectric tube. (b) High speed photography at 100 fps, 30 ms exposure in open air (top row) and enclosed environment matching feed gas chemistry (middle row). The bottom row shows the APPJ coupling to samples, which are marked as dotted blue lines with reflections of the plasma below them.

High speed photography of the APPJ discharge with no surface interaction is shown in Fig. 2.1(b). The APPJ was flowed into either open air (top row) or a controlled

environment matching the feed gas chemistry (middle row). Applied voltage for all gas chemistries is held constant at 14 kV peak to peak and power dissipation was measured to be 6.2 W for Ar, 9.2 W for 1% N_2 in Ar, and 11.6 W for 1% O_2 in Ar. The pure Ar plume is concentrated in one central channel and increases in length as the environment changes from air to Ar. This central channel nature has been attributed previously to the metastable state Ar ($4^3P_2^0$) with 11.6 eV, which does not have enough energy to ionize Ar (E_i = 15.8 eV), so the plasma is only formed by streamer process.[52] N_2 addition creates a comparatively diffuse plume, with discharges branching away from the central filament and extending outward when the environment matches the feed gas. This is likely due to the introduction of Penning ionization that occurs with N_2 metastable species.[53] O_2 addition to the feed gas, regardless of environment, greatly reduces the plume length and intensity. This observation suggests reduced plasma density for the addition of O_2, likely resulting from the loss of electrons by creation of negative oxygen ions[54] and is predicted by modeling O_2 addition to Ar plasma.[55] The confined geometry of the APPJ controls the gaseous environment around the plasma similar to the controlled environment shown here.

Figure 2.1(b) (bottom row) shows high speed photography with 30 μs exposure time of the plasma coupling to the surface. Images show filaments that extend outward from the source tube, sometimes several in one image. At close distances, the etch region is annular following the path of these filaments, as shown in Fig. 2.2(a). However, as the source is moved away from the sample, the diameter of the etched area shrinks from ~7 mm to 3.7 mm, matching the tube inner diameter. This agrees with previous work that shows that plasma bullet emission occurs in a ring shape.[56] Typical etch rates are locally

>100 nm/min where the filaments terminate at the surface for coupled interactions compared to the remote interaction, where etch rates are below 3 nm/min. The thickness removal is lower than similar treatments by Fricke et. al,[49] who see etch rates above 1000 nm/min at distances of 5 mm from the sample, likely due to differences in the APPJ design.

The electrically coupled surface interaction mode visibly damages the photoresist in the form of spots due to intense, localized energy deposition, leading to fast film removal. Figure 2.2(b) shows an SEM image of a damage spot which has high roughness throughout the affected area. High speed photography was used during a 0.5 second treatment and the position of each filament impact was extracted. The position of these strikes is shown in Fig. 2.2(c) and compared to the position of the significant spot damage identified by microscopy. Areas with higher densities of strikes to the surface positively correlate with visible spots. This indicates that the plasma will more likely electrically couple to previously damaged spots. The small number of spots compared to the number of filament interactions with the surface suggests that either not all filaments cause damage or that it takes many strikes before a large spot is formed. The surface area where more than 50 nm of photoresist was removed during the 30 second treatments was determined for various source to sample distances (s_n+s_s) and is shown in Fig. 2.2(d). The amount of photoresist removed decreases as distance increases and decreases more quickly when the plasma is exposed to the ambient environment. This agrees with previous work demonstrating the importance of the ambient chemistry around the APPJ.[14] This result also agrees with the images of Fig. 2.1(b) which show reduced plume

length in open air vs controlled environment matching feed gas, similar to how the plasma is confined in the APPJ tube.

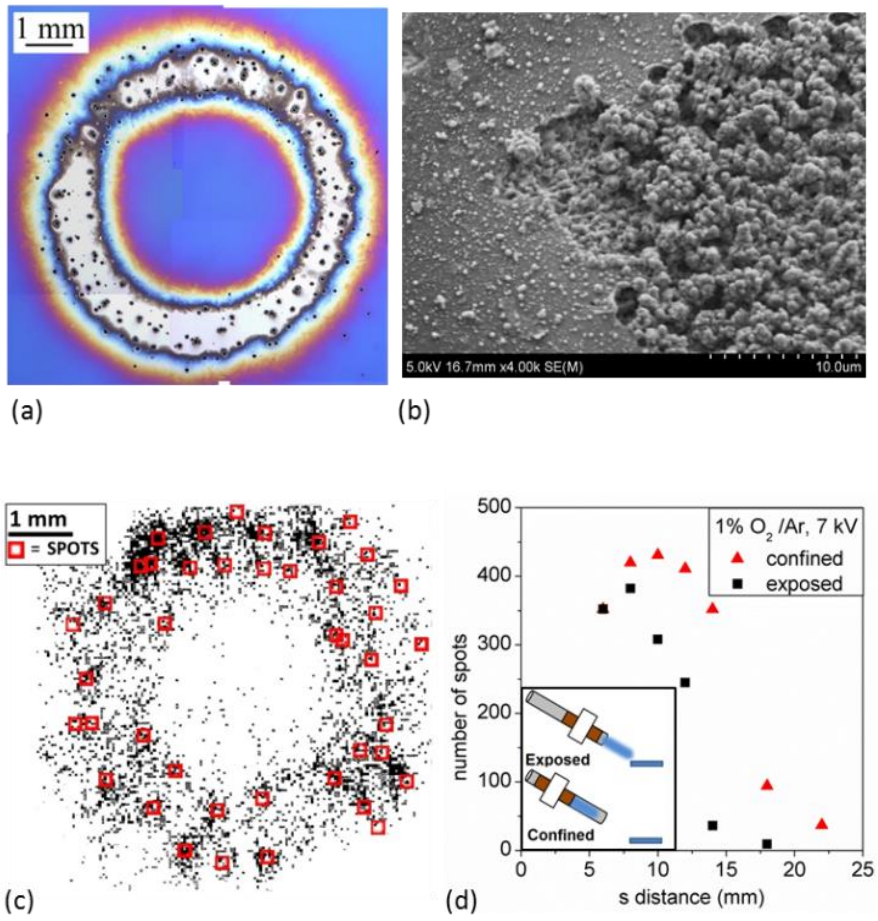

Figure 2.2: (a) 1% O_2 in Ar, s_n = 2 mm, s_s = 4 mm, 30 second treatment image with interference microscopy showing annular effect. (b) SEM image showing high roughness formed at center of a spot under same conditions described in (a). (c) Graph of where filaments hit surface (black pixels) extracted from high speed photography of 0.5 second treatment compared to actual spots seen by optical microscopy (red squares). (d) photoresist surface area etched at rates greater than 100 nm/min vs distance of source from sample ($s = s_n+s_s$) for exposed (s_n fixed at 2 mm) and confined (s_s fixed at 4 mm) conditions.

In the following we discuss remote plasma processing where direct electrical interaction with the sample is avoided. For pure Ar flowing into air, the etch rate of the PR193 film is initially low, called etch lag, and subsequently increases. The duration of this etch lag increases with the amount of time the plasma has been off as shown in Fig. 2.3(a). We found that the increase of the polymer etching rate correlated with heating of the dielectric tube. The temperature of the APPJ source was measured by an FLIR i7 thermal imaging camera and plotted vs etch rate over several experiments to make an Arrhenius plot and estimate an apparent activation energy of ~0.9 eV. Cooling the source externally with compressed air from approximately 80 °C to 50 °C showed a reduction of 0.05 nm/min in etch rate that then increased again once cooling was stopped. This slight reduction further supports the dependence of the plasma surface interaction on source temperature.

The sample was also shielded from the APPJ (using the electrically insulating shield mentioned above), preventing etching while leaving the plasma on to prevent the dielectric tube from cooling. As shown in Fig. 2.3(b), etch lag does not occur and the etch rate recovers immediately after the shield is removed. This suggests that etching is not related to sample heating during the treatment since the sample would have ample time to cool while shielded. The sample temperature was estimated to increase by less than 30 °C during a 30 minute argon treatment by measuring the refractive index changes of bulk Si.[41]

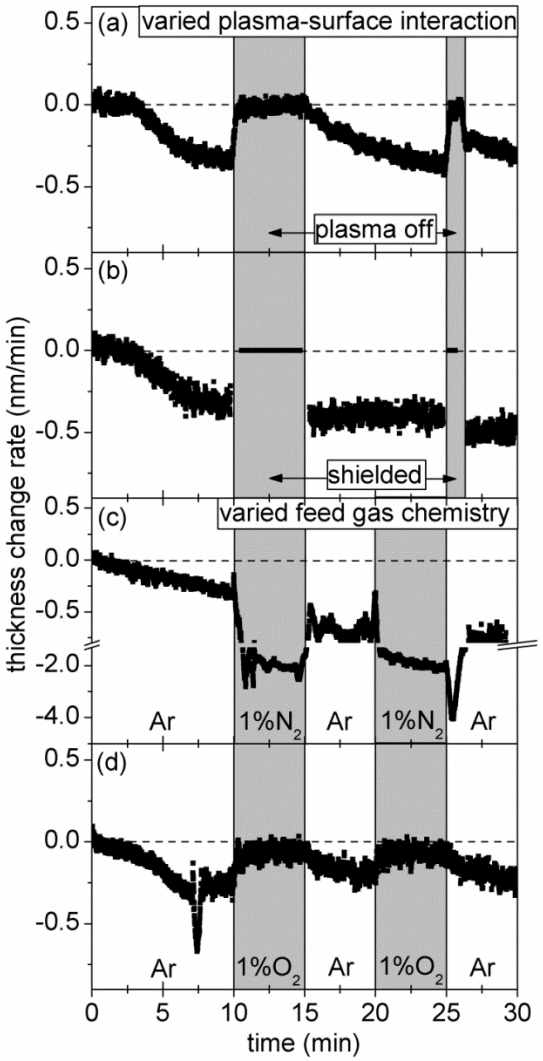

Figure 2.3: Remote treatment ($s_n + s_s = 16$ cm) at 14 kV_{p-p} thickness change rate vs time for (a) cycled Ar plasma on and off, (b) cycled Ar treatment by shielding the sample from the plasma, (c) cycled Ar and Ar/N_2 treatment, and (d) cycled Ar and Ar/O_2 treatment.

Feed gas chemistry at constant applied voltage plays a large role in determining plasma properties[57,53] as well as etching and surface modifications. Figures 2.3(c)-(d) shows a comparison of a remote treatment with alternating pure Ar and 1% N_2 or O_2 admixture to Ar under same electrical characteristics for high speed photography work. Etch rate for N_2/Ar increases to ~2.0 nm/min, which is several times greater than for pure

Ar. N_2/Ar plasma tends to extend further down the APPJ tube at similar conditions than other gas chemistries and shows increased power dissipation from pure Ar, which likely explains the increased etch rate. O_2/Ar has reduced etch rates of ~0.05 nm/min compared to pure Ar, which saturates at ~0.5 nm/min, despite having increased dissipated power. This decrease mirrors the drop in emission intensity seen in the high speed photography.

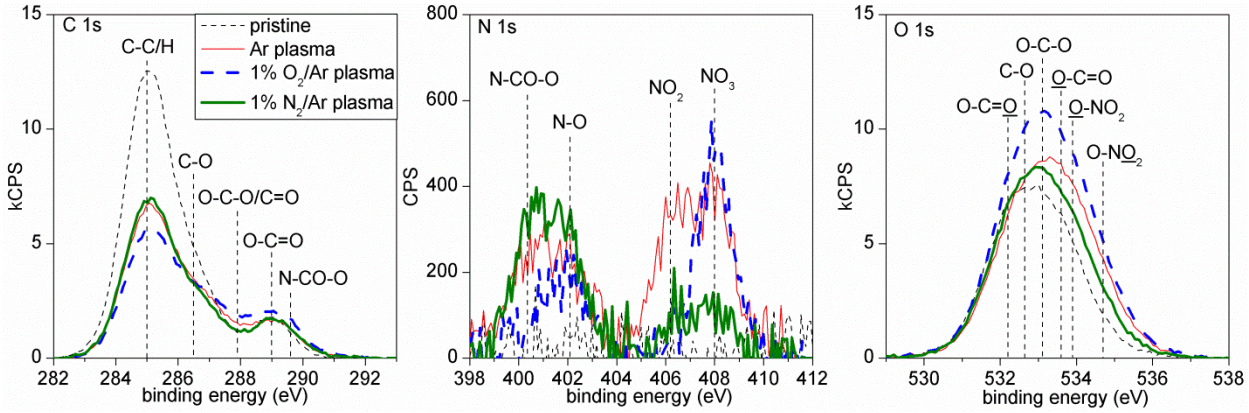

Figure 2.4: XPS spectra taken after 30 min remote treatment for (s_s + s_n) = 16 cm comparing surface chemistry (~3 nm probing depth) of pristine PR-193 for Ar, 1% O_2/Ar, and 1% N_2/Ar treatments.

While oxygen addition to the feed gas reduces the etch rate, increased oxygen uptake at the surface is seen in XPS surface analysis. The oxygenation of the surface for the pure Ar and N_2/Ar treatments likely comes from plasma interactions with ambient air. All three gas chemistries also show the formation of NO_x species at the surface. The O_2 treatment shows increased species with greater oxygen content such as NO_3 whereas the N_2 treatment shows much less NO_3 and increased species that have greater N:O ratios.

2.4 Conclusions

In conclusion, the consequences of APP surface interactions are highly dependent on the interaction modes described here due to the distinct physics governing charged versus neutral species. Understanding what types of species dominate the interaction with the surface is critical to the operation of APP sources and control of surface functionalization. Average polymer etch rates are significantly higher when the plasma couples directly to the surface and produces localized damage as compared to the remote plasma mode interaction, which induces slow uniform etching and subtle surface chemical modifications. In the remote case, etch rate and surface modifications are highly dependent upon feed gas chemistry, APPJ source temperature, and plasma interaction with the environment.

2.5 Acknowledgements

The authors gratefully acknowledge financial support by the US Department of Energy (DE-SC0001939 and DESC0005105) and National Science Foundation (PHY1004256). We also thank D. Metzler, C. Li, and E. Merino for their helpful discussion and collaboration on this project.

Chapter 3: Cold Atmospheric Pressure Plasma VUV Interactions with Surfaces: Effect of Local Gas Environment and Source Design

A. J. Knoll[1], P. Luan[1], E. A. J. Bartis[1],V. S. S. K. Kondeti[2], P. J. Bruggeman[2], G. S. Oehrlein[1]

1. Department of Materials Science and Engineering & Institute for Research in Electronics and Applied Physics, University of Maryland, College Park, Maryland 20742, USA

2. Department of Mechanical Engineering, University of Minnesota, Minneapolis, Minnesota, 55455, USA

This work is published and can be found in full by the following citation: A. J. Knoll, P. Luan, E. A. J. Bartis, V. S. S. K. Kondeti, P. J. Bruggeman, G. S. Oehrlein. Plasma Processes and Polymers 13(11): 1069-1079

Abstract

This study uses the different responses of 193 nm and 248 nm photoresist (PR) materials by vacuum UV photons in combination with several cut-off wavelength optical filters as a diagnostic to examine the relative importance of VUV induced surface modifications for different cold atmospheric pressure plasma (CAPP) sources. We compare the contribution of VUV to surface modifications from four different plasma sources: an argon based kHz driven ring-APPJ, an argon based kHz driven pin-APPJ, an argon based

MHz driven pin-APPJ, and a kHz driven surface microdischarge (SMD) source in air. The kHz-driven ring-APPJ showed the largest ratio of VUV surface modification relative to the total surface modification introduced, whereas the MHz APPJ showed the largest overall surface modification and a much smaller VUV induced component. Additionally the MHz APPJ shows increased total thickness reduction and reduced VUV effect as oxygen is added to the feed gas, a condition that is often used for practical applications. This observation is consistent with the large O density previously measured for this jet. Polymers treated by the open air operated SMD showed no thickness reduction. Experiments show that VUV photons are primarily causing modifications for the kHz driven ring-APPJ. We examine the influence of noble gas flow from the APPJ on the local environment and model this gas flow at different oxygen concentrations and compare to experiments with varied starting chamber oxygen. The local environment has a decisive impact on polymer modification from VUV emission as O_2 readily absorbs the Ar excimer wavelength.

3.1 Introduction

Atmospheric pressure plasma jets (APPJs) are one very commonly used plasma source which usually operates with a noble gas such as Ar or He to reduce the voltage required for plasma ignition. CAPP sources are useful due to their ability to create large fluxes of reactive species at low gas temperatures. There has been a significant amount of work dedicated to modeling these reactive species produced by various types of sources[31,32]. In conjunction with this modeling, there have been many reports on characterization of various reactive species for specific plasma sources such as OH[33],

O_3[34], O[35], and high energy photons[36]. Part of the work below focuses on a particular CAPP source and conditions in which VUV photons are shown to play a dominant role, as is detailed in this manuscript.

There has been other work showing that VUV photons can be generated from CAPP sources, though they focus on aspects other than surface modification. Reuter *et al*.[35] has measured the VUV produced by a MHz pin-style, Ar fed APPJ (kINPen) using a VUV-monochromator under vacuum utilizing a MgF_2 window at the entrance to the monochromator. They also measure the effect of adding small amounts of oxygen to the environment just beyond the plasma end, though their primary interest is measuring the atomic oxygen produced by the source over various distances. Schneider *et al*.[58] published work specifically differentiating VUV/UV from other reactive particles using a specially designed MHz glow discharge APPJ utilizing He/O_2 mixtures which can separate VUV from other reactive species that follow the gas flow convection. They focus mainly on bacteria and biological macromolecule treatment but also look at amorphous carbon films as a model polymer. They found that the VUV photons caused the a-C:H films to harden which reduced etching from other sources (mainly atomic oxygen). They also show that VUV photons alone are relatively ineffective at deactivating bacteria whereas combined VUV and reactive species treatment has the largest effect. Dufour *et al*.[59] discusses VUV emission from a He and O_2 admixture MHz frequency plasma torch (AtomfloTM by SurfX). They propose that the mechanism for surface modification is based on a He_2* excimer which emits at near 60 nm. They also observe that small admixtures of oxygen decrease this VUV emission significantly. There has also been work published looking at the effect of a single plasma source on plasma

ashing of photoresist materials recently[60]. This paper uses a MHz plasma source utilizing He/O_2 mixtures at 3 mm distance from source to substrate. These conditions lead to very high etch rates on the order of 100 nm/min for 20 Watt power dissipation and are attributed primarily to atomic oxygen.

However each of these works generally focus on a single specific type of CAPP source. Some of these sources are driven by kHz or MHz frequencies, operated with different noble gases such as He and Ar, have varied electrode configurations, different dielectric materials, and different electrical properties based on these factors, causing each of them to work differently. One of the goals of this work is to compare a variety of CAPP sources under similar conditions and see how the source type influences the effect on the surface. In particular, we are interested in determining how the relative importance of vacuum ultraviolet induced surface modifications of polymers varies for the different CAPP sources. Much of the literature also focuses on determining which reactive species exist very close to or within the plasma plume itself. Here we focus on a remote treatment, where the plasma is not in contact with the surface being investigated, which leads to a more uniform and mild exposure of the surface as only longer lived reactive species can reach the surface. Additionally this means that very little ionized species reach the surface so sputtering by ions does not occur.

This paper will cover the investigation of a kHz ring-style APPJ source fed by Ar gas flow to determine the dominant species involved in surface modification for a remote treatment. This surface modification was determined to be high energy photons by comparing indirect treatments to those with line of sight and optical filters primarily. The effect of local environment gas composition is investigated to show that this is critical for

the transmission of VUV photons as they are readily absorbed by oxygen species. Finally we compare the effect of VUV for 4 different CAPP sources and under some selected operating conditions to show for which conditions VUV may play the most dominant role compared to other reactive species in the surface modification.

3.2 Experiments and Methods

3.2.1 Plasma Sources

This work investigates four separate cold atmospheric pressure plasma sources. The sources are shown in figure 3.1 and their properties are summarized in table 1.

1. kHz driven ring-APPJ source: This source is based on a design by Teschke et al.[37], and is shown in figure 3.1 a). Two copper electrodes (20 mm length and 6.35 mm ID) are wrapped around a quartz tube (4 mm ID and 6.35 mm OD) and separated by a 1.6 cm thick Teflon block are driven by a variable frequency AC waveform power supply (PVM500, Information Unlimited, Amherst, NH, USA). The applied voltage is measured by a high voltage probe (Tektronix P6015A) connected to an oscilloscope (Hewlett-Packard 54504A) with a 400MHz bandwidth. The standard operating conditions for this jet are 24 kHz, 14 kV_{p-p} voltage, 3.5 Watts dissipated power, 3 cm end of nozzle to sample distance (with plasma contained within the quartz tube), and 2 standard liter per minute (slm) Ar flow rate which corresponds to a 2.6 m/s gas velocity. The power for all kHz driven sources was determined use the Lissajous method using a 10

nF capacitor on to measure the current on the ground of the plasma source[50].

2. kHz driven pin-APPJ source: This source is shown in figure 3.1 b). A central pin electrode with a 1 mm diameter is mounted inside a quartz tube (1.5 mm ID and 3 mm OD) with a grounded copper ring electrode (20 mm length 3 mm ID) outside the tube. The source is operated at 24 kHz, 6 kV_{p-p} applied voltage, 1.5 Watts dissipated power, and with 1.5 slm of Ar flow which corresponds to a gas velocity of 8.0 m/s. The total distance was 3 cm from the end of the nozzle to the sample (with the plasma contained within the quartz tube). The same PVM500 power supply was used as for the other kHz sources with an AC waveform.
3. MHz driven pin-APPJ source: This source was designed by Bruggeman *et al*. and has been extensively characterized[38],[32],[39] and is shown in figure 3.1 c). The design uses a 1 mm diameter tungsten pin electrode mounted inside a quartz tube (1.5 mm ID and 3 mm OD) with a grounded copper ring electrode (5.3 mm length, 3 mm ID). The standard operating conditions of the MHz jet are 13.5 MHz modulated driven frequency with a 0.2 on/off duty cycle (20% on time, 80% off time), a time-averaged power dissipation of 3.5 Watts, a gas flow of 1.5 slm which corresponds to a gas velocity of 8.0 m/s, and a distance from jet nozzle to sample of 1.5 cm. Details of how the power was calculated for this source can be found in detailed work done previously[40]. Operating conditions were kept as close to previous work as possible to make it comparable.

4. kHz driven SMD source: This source is a kHz driven surface microdischarge source and is shown in figure 3.1 d). The phase electrode is a 5 cm square copper plate, the ground electrode is a stainless steel mesh with 50% of opening, and a 1.6 mm-thick quartz plate dielectric separates these electrodes. The source is operated at 42 kHz, 6 kV_{p-p} applied voltage, in ambient air, with 3 mm distance from the metal mesh to the sample. The same PVM500 power supply was used as for the other kHz sources with an AC waveform. The SMD style source, due to its different design and operation, operates at about 6.5 watts total dissipated power but over a much larger area of discharge. This source serves as a reference for the large number of plasma sources which are not jet styles.

3.2.2. Description of Materials

Polymethyl methacrylate (PMMA) based 193 nm photoresist (PR193) with 300 nm film thickness and polystyrene (PS) based 248 nm photoresist (PR248) with 400 nm film thickness were used for these experiments. These materials have been extensively investigated previously along with details of their chemical structures, and they show significantly different behavior when exposed to VUV radiation[61].

3.2.3 Surface Characterization

The primary surface characterization technique in this work was an ellipsometer utilizing a 1.5 mW HeNe laser at 632.8 nm which was used to non-invasively investigate thickness and index changes measured in real-time and extracted through optical

modeling of the ellipsometric data. The data extracted from this modeling is given in terms of thickness loss as the area measured by the laser spot is the same for all samples. Fourier transform infrared spectroscopy (FTIR) was conducted using a Shimadzu IRAffinity in attenuated total reflection (ATR) mode. The ATR was performed using an internal reflection element of Ge crystal at 60° and the spectra were obtained using a wire-grid polarizer (at 270° angle) placed between the interferometer and the ATR cell. The absorbance spectra were collected at 4 cm^{-1} resolution over 500 cm^{-1} to 3000 cm^{-1} and averaged over 20 cycles. Images taken of samples post treatment were performed using a differential interference contrast microscope equipped with a digital camera.

3.2.4 Experimental Conditions

All plasma sources were mounted in a vacuum chamber with a 43 liter volume. The chamber can be evacuated and refilled with a controlled gas chemistry for various treatments. During experiments, this gas flow was not continued to prevent disruption of reactive species convection to surface. When not specified the chamber was filled with dry air prior to the start of the experiment. The operating distance was chosen for each source to be just far enough away to not cause arcing or any filament interaction from the source with the sample, which we call the remote treatment regime.

This paper primarily investigates comparing jet type plasma sources fed by pure Ar feed gas unless otherwise specifically stated. The Ar used for this is 99.998% pure and gas lines are evacuated and refilled with pure Ar prior to experiments.

MgF_2 and sapphire (or alumina) optical filters are used to narrow down that wavelength of VUV emission that affects surface modification. The MgF_2 filter has a

cutoff wavelength of 114 nm and sapphire filter has a cut off wavelength of 142 nm. When used the filters are placed directly on top of the sample to prevent air between the filter and the sample.

3.3 Results and Discussion

3.4.1 Comparison of Plasma Sources

In this work we find that a kHz driven ring-APPJ operated so that the plasma does not directly contact the surface primarily causes polymer thickness loss due to VUV emission. This explains behavior previously seen for this source where less thickness loss occurred for oxygen addition to the feed gas[62]. While high energy photons are clearly the critical species inducing polymer modifications for remote treatment by a kHz driven ring-APPJ source, it is unclear if results seen for other atmospheric pressure plasma sources were consistent with this finding. The physical sources and selected operating conditions are shown in figure 3.1.

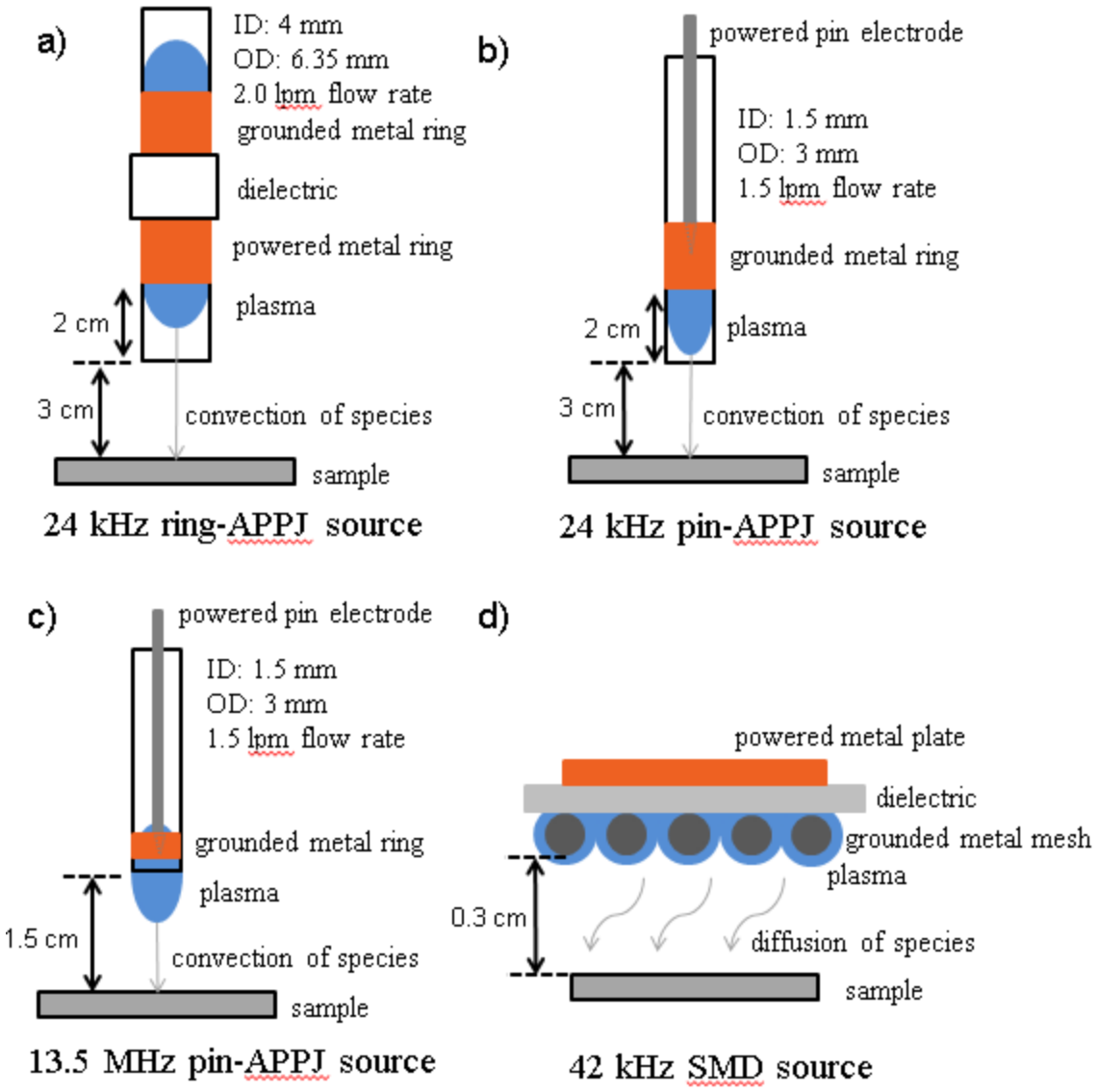

Figure 3.1: Noble gas (Ar) fed a) kHz driven ring APPJ with two ring electrodes outside quartz tube, b) kHz driven pin APPJ with grounded metal ring outside quartz tube and powered pin electrode inside, and c) MHz driven pin APPJ with grounded metal ring outside quartz tube and powered pin electrode inside. Ambient air operated d) kHz driven surface microdischarge source.

Table 3.1: Comparison of a 20 minute plasma treatment in an air environment with Ar feed gas where applicable comparing with and without a MgF_2 filter.

source	dissipated power for Ar (Watts)	applied voltage for Ar (kV_{p-p})	gas flow rate (lpm)	tube inner diameter (mm)	driving freq.	average thickness loss rate without MgF_2 filter (nm/min)	average thickness loss rate with MgF_2 filter (nm/min)	relative importance of VUV effects
MHz pin APPJ	3.5	0.15	1.5	1.5	13.5 MHz	10.29	0.11	1.1%
kHz ring APPJ	3.5	14.0	2.0	4.0	24 kHz	0.749	0.153	20.4%
kHz pin APPJ	1.5	6.0	1.5	1.5	24 kHz	0.012	0.005	6.6%
SMD	6.5	6.0	-		42 kHz	0.0	0.0	-

The comparison between each source with and without a MgF_2 filter over a PR193 sample is shown in table 3.1. The MHz pin-APPJ has the largest thickness loss rate without a MgF_2 filter. With the MgF_2 the thickness loss rate is approximately 1% of the thickness loss rate without the filter, suggesting that for this source, long lived reactive species play an important role in the etching process. However it is clear that there are some high energy photons being produced with this source as well. The kHz ring-APPJ, which has been investigated in previous work, shows the largest ratio of thickness loss rate with a MgF_2 filter as compared to without. The kHz driven pin-APPJ shows reduced thickness loss rate for both conditions compared with the ring-APPJ and the VUV component is smaller. Finally, the kHz driven SMD source, operating in O_2 and N_2 mixed environments (including air), shows no thickness reduction for either condition. It should be noted that the overall treatment area for the MHz pin APPJ and the kHz pin

APPJ sources is slightly smaller than that of the kHz ring APPJ which would be important for calculating the exact efficiency of material removal but is outside the scope of this work.

There are several possible differences between the sources that could lead to varied influence of VUV. The three APPJ type sources all show some VUV modification, likely related to the noble gas. The SMD source operates in open air normally with no gas flow. While VUV photons can be produced in air, the VUV emission is typically less abundant than excimer emission in argon and the absorption length is also of the order of 100 μm or less preventing VUV photons to reach the substrate[63], therefore no VUV effect was expected for the SMD source. The ring-APPJ source has no electrode in direct contact with the plasma which means that it requires a much higher operating voltage than the other sources for gas breakdown. In addition, the sources with an inner powered pin electrode in contact with the plasma exhibit a higher electron density since the electrode can emit electrons directly into the plasma, though it can also possibly disrupt the gas flow compared with the ring only source. This configuration also likely produces higher local electric field strength near for the pin electrodes than for the double ring electrodes. Another parameter that likely has a strong influence is the driving frequency. The plasma density and composition will be higher for the MHz source compared with the kHz sources due to changes in relaxation time for the plasma generated which leads to a much higher reactive species density for the MHz source than the kHz sources. In addition, the power density of MHz source is also significantly larger than for the kHz sources for the investigated conditions enhancing further the reactive species density. There are additional small differences between the sources such as a 1.5 lpm flow rate for

the MHz jet compared with the 2 lpm flow rate for other sources. The distance from the plasma to the sample was kept to a minimum distance without the plasma directly touching the sample which leads to a difference in the overall distance from the source electrodes to the sample.

The impact of higher energy photons on thickness loss is highly dependent on local oxygen content as will be shown in this analysis. APPJ sources that operate with noble gas often have small admixtures of reactive gas species introduced to provide tailored reactive species for certain applications. The addition of oxygen, to produce atomic oxygen and other reactive species, has been shown previously to be a crucial addition to certain APPJ sources that operate close to or in contact with the sample surface[19],[64]. The introduction of oxygen to the feed gas of the MHz APPJ source shows less thickness loss with a MgF_2 filter in place over the sample, which corresponds to only the VUV effect (see Fig. 3.2). This result matches well with previous work by Dufour who show this decreased VUV effect with molecular oxygen addition to the feedgas[65]. Additionally, the addition of oxygen quenches the metastables that are responsible for the formation of Ar excimer and the VUV radiation.

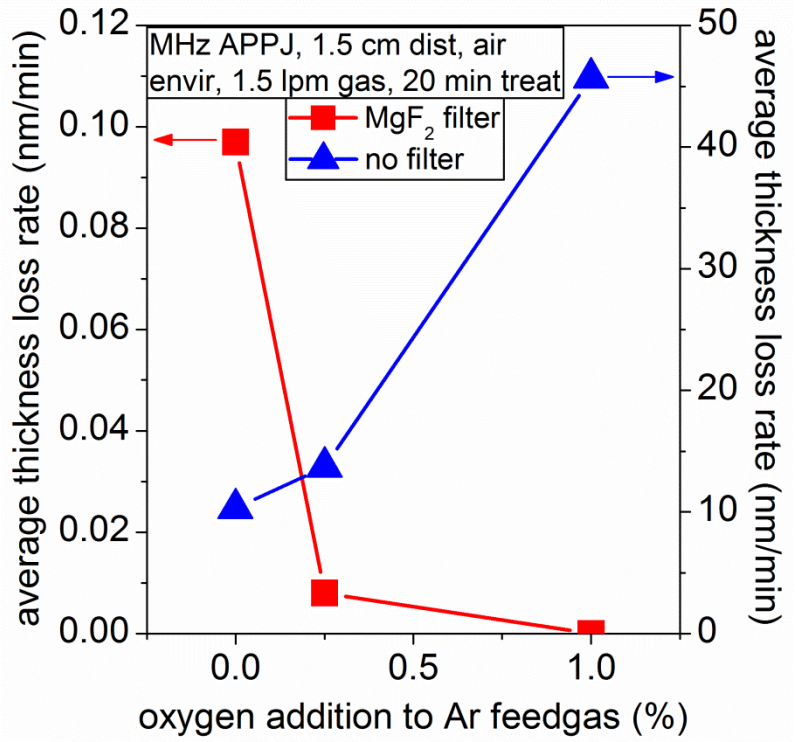

Figure 3.2: Oxygen addition to MHz APPJ feedgas decreases average thickness loss rate through a MgF_2 filter but increases average loss rate for no filter for 20 minute treatment.

The MHz APPJ shows the opposite effect without the MgF_2 filter in place, showing more thickness loss with increasing oxygen addition to the feed gas. This increased effect is due to the primary surface modification species being a reactive radical, likely atomic oxygen. It has been reported that this particular MHz APPJ source produces atomic oxygen densities on the order of 10^{16} cm^{-3} for similar conditions used here[66]. This increased thickness loss rate is further evidence that the type of APPJ source used is critical with respect to the surface effect needed as different reactive species have vastly different surface effects.

3.4.2 Role of VUV in Surface Modification

The kHz driven ring-APPJ source has the highest ratio of modification from VUV compared to total modification so this source was chosen to further investigate the effect of VUV. The details of this source are shown in figure 3.1 a) and has been described above. The standard operating conditions that are used are 24 kHz, 14 kV peak-to-peak voltage, 3 cm end of nozzle to sample distance (with the plasma contained within the quartz tube), 2 standard liter per minute (slm) Ar flow rate into an air environment within a vacuum chamber, and a standard treatment time of 20 minutes.

In order to initially determine the importance of VUV we first tested whether the reactive species involved in the PR193 modification are highly directional. This is tested by removing line of sight treatment from plasma to sample. This was first shown by using a quartz tube with a bend in it to allow reactive species to travel to the surface but not photons and keep the same total distance from the surface to the plasma. This geometry showed no thickness reduction or modification effect. A grounded metal mesh placed directly over the sample was used to confirm that line-of-sight interaction is key. Treatments with the metal mesh showed a clear transfer of the mesh pattern onto the PR193 sample as shown by images of samples post treatment in figure 3.3 a) and b). These images were taken post treatment using the differential interference microscope. In order to further narrow the suspected species down, a MgF_2 filter with a cutoff wavelength of 114 nm was placed directly over the sample above the metal mesh which still showed the pattern transfer to the PR193 film. This confirmed that the primary reactive species causing surface modification for this plasma source are high energy photons. The effect was not as visible on PR248 as it is more resistant to modification by

high energy photons[67]. Certain structures of PR248 are still susceptible to modification by high energy photons, such as the ring structure, but overall the material is more stable.

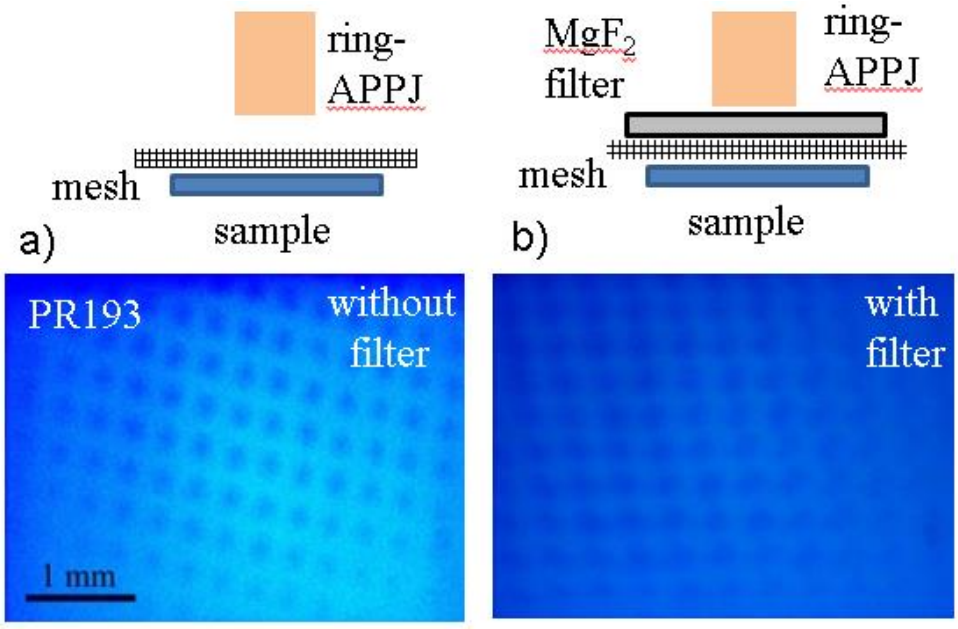

Figure 3.3: Exposure of PR193 photoresist material to different sources with metal mesh between source and sample. (A) The ring-APPJ source with no filter and (b) the ring-APPJ source with a MgF_2 filter both show pattern transfer.

The kHz driven SMD source was also investigated using the metal mesh with and without the MgF_2 filter. No surface modification was seen for either case. There are several differences between the SMD and ring-APPJ but primarily the SMD operates in open air whereas the primary gas in the APPJ case is argon. This provides evidence that the photons are directly related to the presence of noble gas and suggest excimer radiation.

Multiple optical filters were used to determine the wavelength of the high energy photons. The modification of PR193 is seen when a MgF_2 filter is over the sample but no modification is seen if a sapphire (alumina) filter is used instead. This is shown in figure 3.4 along with the effect for no filter and the comparison to PR248. This suggests that the wavelength of the high energy photons that are causing this modification is between 114 and 142 nm, which is in the vacuum ultraviolet range. This provides evidence that the emission is due to Ar_2* excimer species which emits in a continuum spectrum around 125 nm[68]. It is also possible that there are some contributions to this emission from impurities in the Ar gas flow. This Ar_2* excimer state is created by a three-body collision process involving argon metastable states[69]. Emission from this species has been characterized by previous work[35], but the effect it has on surfaces has been limited to disinfection[58]. The modification seen without any filter in place is greater than with an MgF_2 filter. This increase without the MgF_2 filter may be due to some attenuation from the MgF_2 filter as the transmission drops quickly near the cutoff wavelength. It may also be due to some emission from the Ar emission lines at 104.9nm ($^1P_1$ - $^1S_0$) and 106.7 nm ($^3P_1$- $^1S_0$) which would be cutoff entirely by the filter. Finally the increased effect could be due to some interaction from very long lived reactive species.

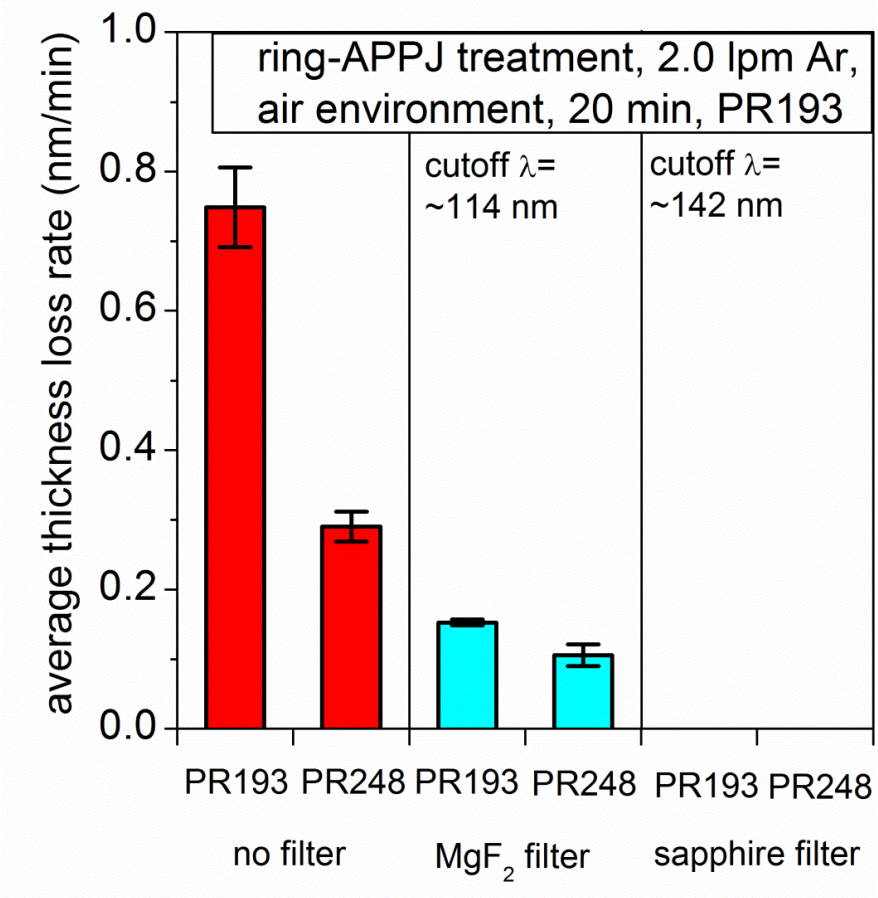

Figure 3.4: Average thickness loss rate measured by ex-situ ellipsometry of PR193 and PR248 photoresist material with various types of high energy photon filters directly over the sample.

Photoresist surface modification was measured by attenuated total reflection Fourier transform infrared spectroscopy (ATR-FTIR). PR193 and PR248 were measured in their pristine state, after a treatment with a MgF_2 filter over the sample, and after a treatment with no filter as shown in figure 3.5 a) and figure 3.5 b) respectively. We would expect VUV to affect only the top 100 nm of the films but if this layer is modified than we should still see a difference in the FTIR spectra. PR193 shows degradation of the

C=O bonding and reduction of the C-O-C bonding after treatment with both the MgF_2 filter and without any filter. PR248 shows only slight reduction in the C-O-C bonding. These results are similar to previous FTIR analysis of photoresist introduced by VUV photons using low pressure plasma[70]. Figure 3.5 c) shows the approximate structure of these two polymers and shows the most likely bonds that would break and reform upon VUV irradiation. These reductions correspond to the signal that is shown in the FTIR and are also seen previously in the literature. This provides supporting evidence that we are seeing VUV modification of these photoresist polymers by atmospheric pressure plasma.

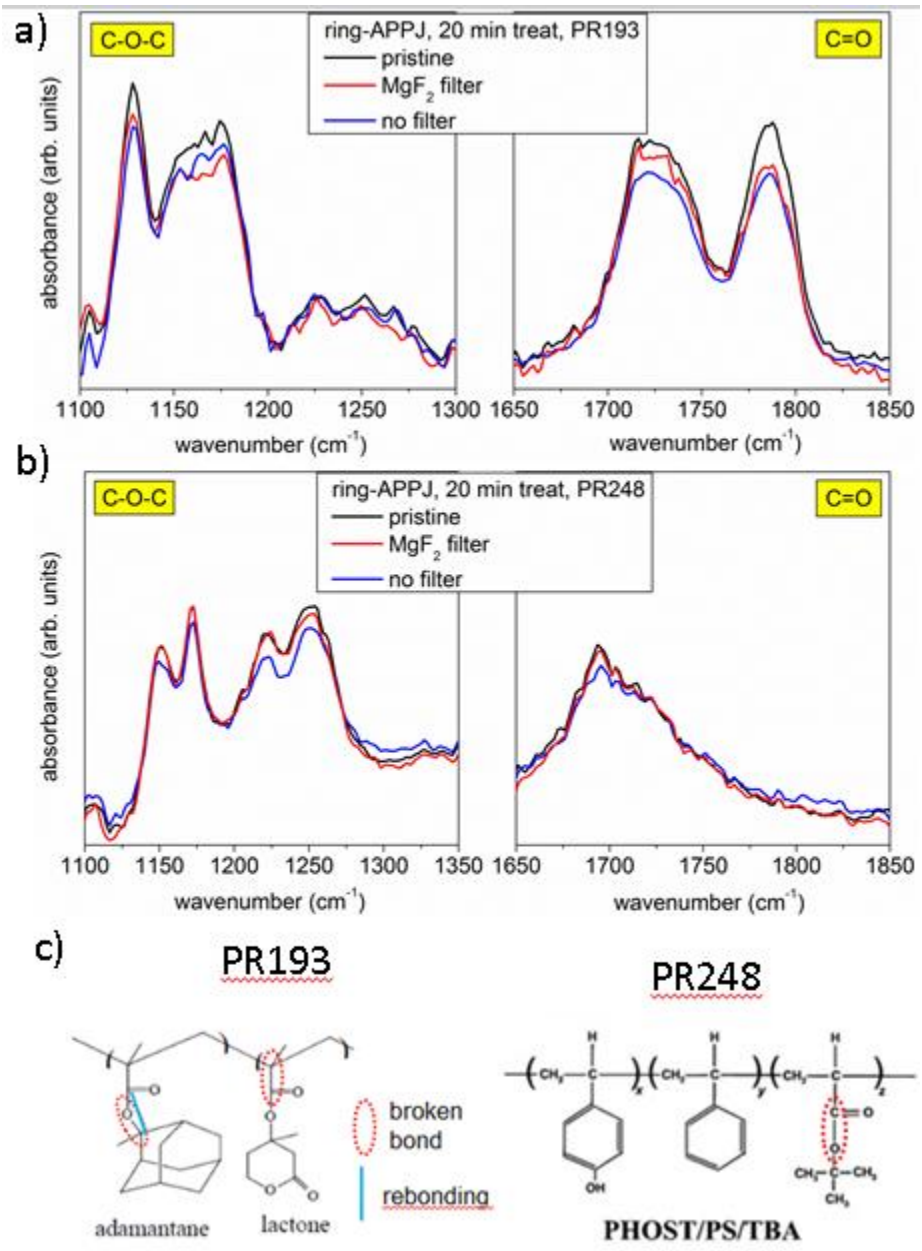

Figure 3.5: ATR-FTIR of (a) PR193 and (b) PR248 photoresist materials showing changes in bulk polymer structure, specifically in the C-O-C and C=O bonding. (c) The chemical structure of these photoresist materials and the proposed changes to them are also shown.

3.4.3 Influence of Local Environment

While conducting the initial experiments, it was observed that the treatments had a lag time of several minutes before modification of the polymer started to occur and then continued to increase over the treatment time. The influence of the gas flow was tested by flowing the gas for 20 minutes prior to starting the plasma experiments. No lag time was seen when this procedure was used and the starting modification rate was very similar to the ending modification rate for the regular 20 minute experiment. The results of this experiment are shown in figure 3.6 a). The Ar flow from the ring-APPJ must be having an influence on the local environment based on this evidence. Residence time in the chamber used was calculated to be 21.5 minutes based on the volume of the experiment chamber (43 L) and the flow rate of the Ar gas (2 lpm). This calculation was used to determine the average Ar concentration in the chamber over time and was then applied to the time of the experiments mentioned previously and is shown in figure 3.6 b). This suggested that Ar is displacing the local air environment which allows for VUV to be transmitted at atmospheric pressure.

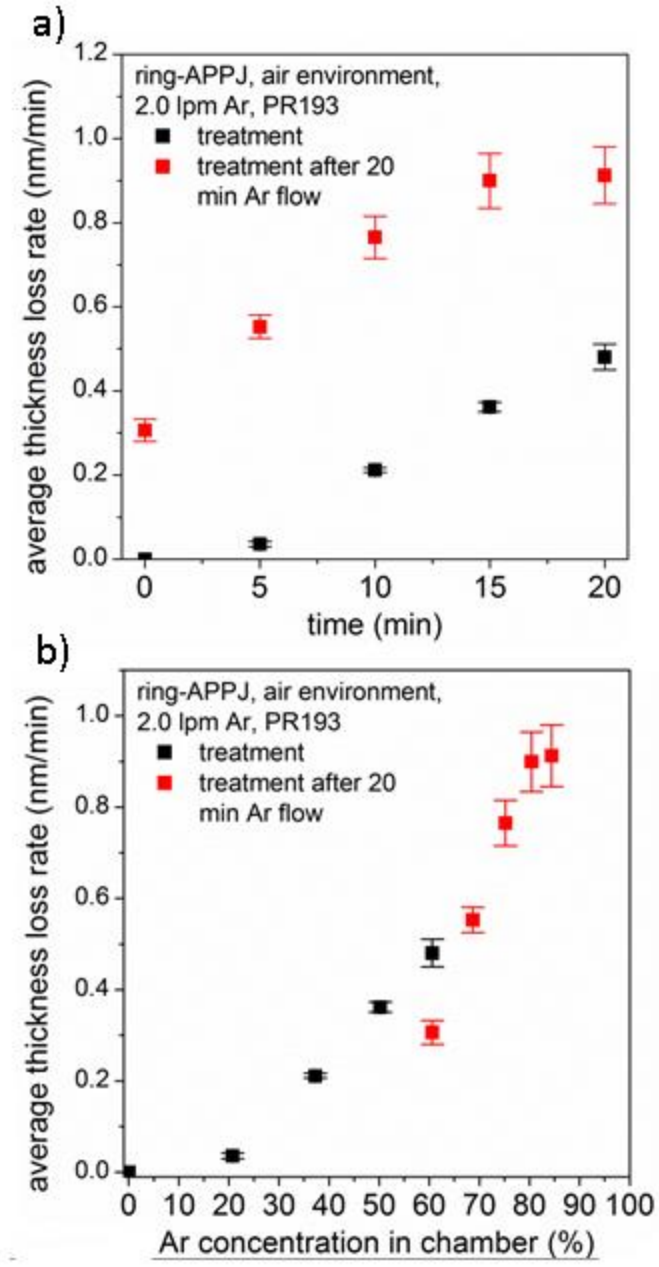

Figure 3.6: (a) Comparison of thickness loss over time with and without gas flow prior to experiment. (b) Influence of chamber argon concentration on average thickness loss rate.

The vacuum chamber housing the ring-APPJ source was evacuated and refilled with various O_2:N_2 mixtures prior to treatments of PR193 as shown in figure 3.7 a).

Modification starts immediately only when there is no oxygen present in the ambient gas. Modification rate also appears to plateau for the treatment with no oxygen after about 10 minutes of treatment. Using the same residence time calculation as done previously the total remaining oxygen in the chamber can be estimated based on the starting oxygen concentration and is shown in figure 3.7 b). We can see here that there is still a slight lag at the beginning of treatments. However, for data 10 minutes and longer we see a very clear exponentially decreasing effect with increasing oxygen remaining in the experimental chamber. Overall it is clear that as more oxygen is present in the ambient gas, less modification occurs to the PR193 sample. High energy photons in the VUV range are most readily absorbed by oxygen species and therefore this provides further evidence that high energy photons must be the dominant reactive species.

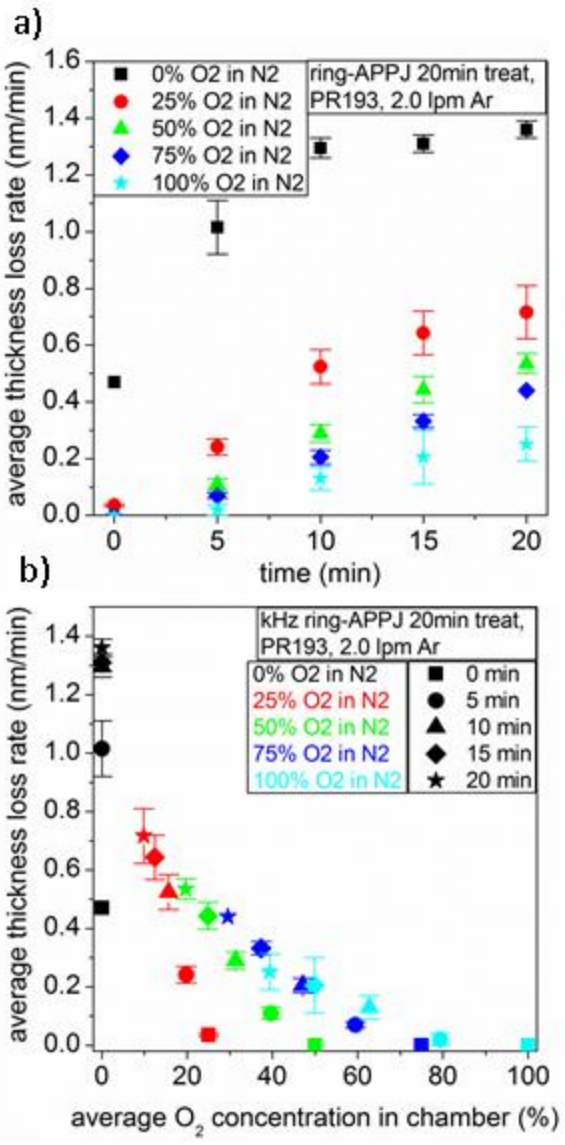

Figure 3.7: (a) Thickness loss rate for various starting chamber ambient gas chemistries over time and (b) the same data shown as a function of average oxygen concentration remaining in chamber.

In order to fully understand the effect of the Ar gas flow from the APPJ on the ambient gas, a finite element model was developed using COMSOL[71]. This model was

developed assuming laminar flow and without consideration for heating of the flow gas. There has been work on other plasma sources that suggests that plasma heating of the flowing gas could lead to turbulent flow, especially for higher flow rates in conjunction with smaller APPJ tube size[72]. For the kHz ring APPJ we did not observe significant gas heating and the gas velocity is lower than reported thresholds for which turbulence occurs[73]. The average ambient oxygen concentration in our chamber is not a good measure of the oxygen absorbing the high energy photons since the Ar flow is concentrated directly between the sample and tube so there will be little oxygen in this region compared to the overall chamber. A simple model was developed based on the diagram shown in figure 3.8 a) to explain this difference. The gas velocity exiting the tube for our flow rate and tube size is about 2.5 m/s to start and is slowed as it approaches the sample before spreading out to the sides. This profile is shown in figure 3.8 b) and is kept constant for the concentration modeling. Since the average oxygen concentration in the chamber is known at any given time point, the modeling was performed at a number of static ambient concentrations. The results for the oxygen concentration over the distance between the jet nozzle and the sample are shown in figure 3.9 a). This suggests that the local oxygen concentration in the jet effluent is approximately 2 orders of magnitude lower than the ambient chamber surroundings.

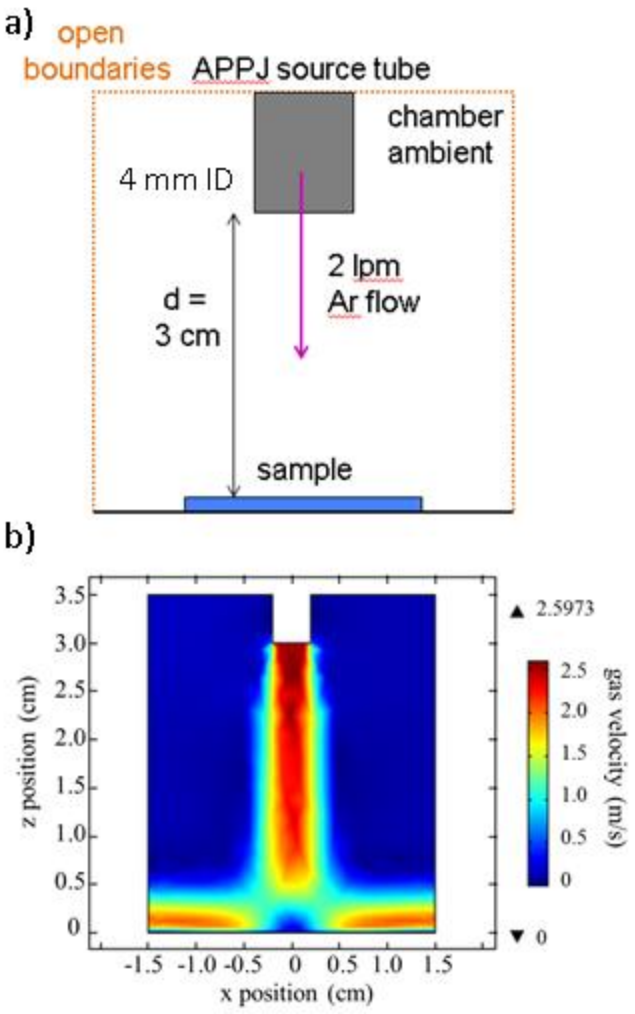

Figure 3.8: Analysis of local oxygen concentration between nozzle and sample. a) diagram of model setup. b) Model steady state gas velocity profile.

The oxygen concentration suggested by the COMSOL modeling was then applied to a Beer-Lambert transmittance calculation to show the expected effect of oxygen attenuation. The equation describing the particular case here is as follows:

$$ln\frac{T}{T_0} = -\int_0^L n_{O_2}(x)\sigma_{O_2}dx \qquad (1)$$

In this equation T_0 is taken to be the maximum polymer modification effect which occurs in a pure Ar/N_2 environment containing no oxygen and will be proportional to the number of VUV photons transmitted for these conditions. T is taken to be the amount of polymer modification at a given oxygen level ambient which is proportional to the actual transmission after some loss to oxygen absorption. This transmission term (T/T_0) is used to represent the number of photons that are interacting with the surface. L is the path length of the VUV photons through the oxygen-containing gas which is 3 cm from the nozzle to the sample, n_{O2} is the oxygen number density based on the oxygen concentration, and σ_{O2} is the oxygen cross section at 125 nm. The oxygen cross section was found from the literature to be approximately 10×10^{-18} cm^2 for 125 nm[35,74]. Water vapor can also absorb VUV photons in this range at a similar magnitude to oxygen but the chamber is refilled with dry compressed air so the concentration of water vapor to oxygen should be small enough to not influence this significantly. The distance was broken up into discrete steps of 1 mm spacing (x) and the oxygen concentration was averaged within these steps.

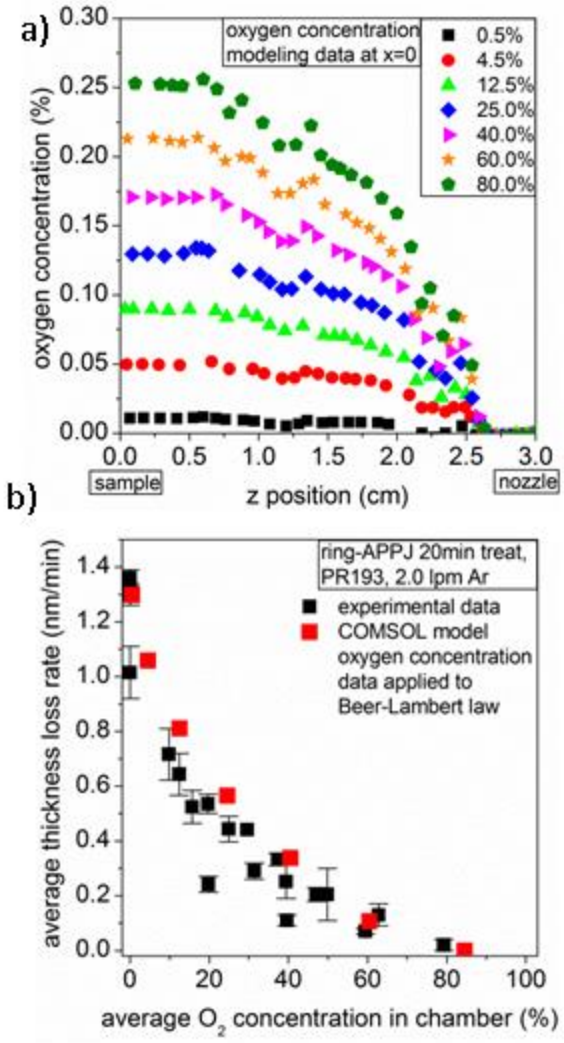

Figure 3.9: a) Extracted oxygen concentration for various chamber ambient oxygen concentrations over y position at discrete points (model output) b) comparison of modeling data with experimental data.

The comparison of the results from this calculation with the experimental data is shown based on the ambient oxygen in the chamber in figure 3.9 b). The comparison here shows the average thickness loss rate at a given time period from the experiment which

corresponds directly to an average ambient oxygen concentration within the chamber. This ambient is then modeled using the COMSOL program and to give concentration over the distance between the nozzle and the sample broken up into steps as described above. The equation 1 is then used to calculate the attenuation of the VUV based on a maximum effect in a nitrogen environment. Comparison of the model to the experimental data suggests that the model gives a fairly good representation of how the Ar flow is affecting the local O_2 concentration near the plasma source, and the effect on VUV induced sample modifications. The only deviation from this trend is showing a lower modification rate (corresponding to a lower transmission) than expected for certain data points. These data points are from the start of the treatments when we see the initial lag in modification where the modeling makes an assumption that the maximum modification rate (T0) is taken from time points after this initial lag. Additionally, the COMSOL modeling is conducted by calculating the steady state condition so that it predicts the maximum modification rate for a given condition. Therefore it is expected that the data and the COMSOL model match best toward the upper end of the modification rate data.

3.4 Conclusions

High energy photons in the VUV range have a strong impact on near-surface modifications for remote plasma treatments of PR193 by a kHz driven ring-APPJ. This modification is highly directional, and takes place through a MgF_2 filter. The nature of the observed changes of the photoresist chemical structure is similar as seen for VUV exposures for low pressure Ar containing plasma. Oxygen in the local environment

readily absorbs the high energy photons but this is displaced over time by the Ar flow from the APPJ. A simple model of the gas flow was used to show that the oxygen concentration between the jet and the sample is dependent on the composition of the average gas environment in the chamber, but much lower. The type of APPJ source is a key factor in the relative importance of VUV photons relative to other reactive species in its contribution to surface modification. The presence of noble gas, along with other design specifications, is important for the generation of VUV and its transmission to the surface. Even small additions of oxygen to the noble gas fed to the APP source can reduce the overall VUV induced effect and in the case of the MHz jet could strongly enhance the mass loss rate through a radical process, most likely atomic oxygen.

3.5 Acknowledgments

The authors thank D. Metzler, C. Li, A. Pranda, B. Nguyen for helpful discussions and other contributions to this work. We also gratefully acknowledge financial support of this work by the US Department of Energy (DE-SC0005105, DE-SC0001939) and National Science Foundation (PHY-1004256, PHY-1415353).

Chapter 4: Polymer Etching by Atmospheric-Pressure Plasma Jet and Surface Micro-discharge Sources: Activation Energy Analysis and Etching Directionality

A. J. Knoll[1], P. Luan[1], A. Pranda[1], R. L. Bruce[2], G. S. Oehrlein[1]

1. Department of Materials Science and Engineering and the Institute for Research in Electronics and Applied Physics, University of Maryland, College Park, MD 20742, USA

2. IBM TJ Watson Research Center, Yorktown Heights, NY, 10598, USA

This work is published and can be found in full by the following citation: A. J. Knoll[1], P. Luan[1], A. Pranda[1], R. L. Bruce[2], G. S. Oehrlein, Plasma Processes and Polymers, 2018;e1700217

Abstract

Treatments of polymer films using either a MHz atmospheric pressure plasma jet (APPJ) or an atmospheric pressure surface micro-discharge (SMD) plasma are investigated. While the typical approach to determine relevant reactive species is to correlate surface effects with gas phase species measurement, this does not capture potential synergistic or other complex effects that may be occurring. Activation energy and directionality of the etching process can characterize what is occurring at the surface for these processes in more detail. The APPJ source shows an apparent activation energy of ~0.18 eV at 8 mm

distance and up to ~0.34 eV at 16 mm distance for a temperature range of 20 to 80 °C tested with thin polymer films. The APPJ source shows directional etching at 8 mm distance with less anisotropy the more distance is increased. The SMD source has an apparent activation energy of ~0.8 to 0.9 eV at a distance of 3 mm. The SMD also only shows isotropic etching behavior. However the SMD surface chemistry changes significantly to less oxidation with increased temperature while the APPJ source induced modifications remain very similar with temperature change. The lower apparent activation energy of the APPJ-induced etching reactions as compared with low pressure work (0.5 eV) and observation of line-of-sight contribution to etching suggests the involvement of a directional species at closer distances facilitating the etching which falls off with increasing distance. The high activation energy of the SMD suggests that species with less capability for etching is responsible compared to the APPJ and low pressure plasma. The high surface oxidation from low temperature SMD treatments shows that the surface is being oxidized but not sufficiently to reach the desorption step of the etching process.

4.1 Introduction

Cold atmospheric pressure plasma (CAP) sources are being applied to increasing numbers of applications due to their versatility. While CAP sources have been used for ozone production since CAP technology was first developed, recently the development of jet style sources with an extended plume near ambient temperature has allowed expansion to new applications,[1] including plasma medicine,[2,3,4] polymer adhesion,[9] thin film deposition,[10] water decontamination treatment,[11] food sterilization,[12] and catalyst

enhancement.[13] Despite the wealth of applications being studied, there is a lack of understanding of the causal relationship between the reactive species that are produced and the surface effects seen. Specifically plasma has been shown to have significant impact on polymers,[75] tissue,[76] biomolecules,[77] and cells[78] but in all of these studies it in unclear what the key variables are that determines the seen surface effect. There has been a significant amount of research dedicated to modeling reactive species and how their densities change with various plasma parameters of sources.[31,32] Additionally effort has been dedicated to measuring various species such as OH,[33] O_3,[34] O,[35] and high energy photons[36] for various plasma sources.

The goal of this work is to understand two distinct CAP sources that behave very differently when interacting with thin polymer films and to understand key variables that determine outcomes at surfaces. Previous studies have shown that there are key differences between the plasma sources with regard to etching polymer films.[79] We seek to compare a MHz APPJ source with a SMD source that between these two types have shown fundamentally different behavior with respect to their interactions with polymers surfaces. The MHz APPJ has been well characterized[80,32] to determine which gas phase species it produces and these have been correlated to the amount of etching of polymer films.[81,82] The SMD has also been characterized[83] and shown to produce some similar gas phase species however it does not cause significant etching of polymer films at room temperature. Additionally we found that the total amount of surface modification is significantly higher for the SMD than for the MHz APPJ, consistent with the plasma surface interaction mechanism being very different between these two sources. It has been assumed previously that all the etching seen at room temperature is due to short-lived highly-reactive chemical

neutral species which travels from the plasma source to the sample when there is no visible contact between them.[81,82] This work seeks to explain these differences by investigating the behavior of the species that are responsible for etching and surface modification by looking at directionality and activation energy.

A first question this paper will seek to answer is why two different styles of CAP sources cause completely different behaviors when interacting with polymer films with regard to etching and surface modification, and how this difference may be useful in understanding the etching mechanism. This question can be investigated by looking at numerous different operating parameters of the various sources such as gas chemistry, distance, and sample temperature. Additionally we can compare the behavior of the CAP sources with low pressure plasma systems treatments on the same surfaces to better understand these differences. The next question is can we understand if there are differences in the reactive species being generated by the different CAP sources by investigating specific surface effects such as activation energy and directionality. Understanding the cause of this difference would allow for better design considerations of sources toward specific applications.

Our approach to answer these questions will be to use methods that have been previously used in low pressure plasma environments to investigate polymer etching. The first measurement of surface interactions will be to examine the activation energy characteristic of polymer etching for each plasma source. The polymer film used here is a 193 nm photoresist which has been analyzed at low pressure so the activation energy in oxygen plasma systems is well documented.[84] Aside from this comparison, the polymer film is based on poly-methyl methacrylate (PMMA), a commonly used polymer and our

results can therefore be related to these.[85] In general, a lower activation energy suggests that etching species carry energy to the surface and initiate polymer etching.[86] Higher activation energy suggests that the etching species have less energy and more thermal energy is needed for etching to occur. Another method that will be utilized is investigation of the directionality of the etching species produced by the plasma sources. This will be done using 3 dimensional structures with stacked layers of polymer films which can be etched and a layer of hard mask which should not be etched by any plasma produced species.

4.2. Experimental Procedures

4.2.1 Plasma sources

Two primary plasma sources were utilized in this work. They were chosen due to their completely different principles of operation and operating environment, and the variances in surface effects such as modification and etching seen from previous work.[81,17,82]

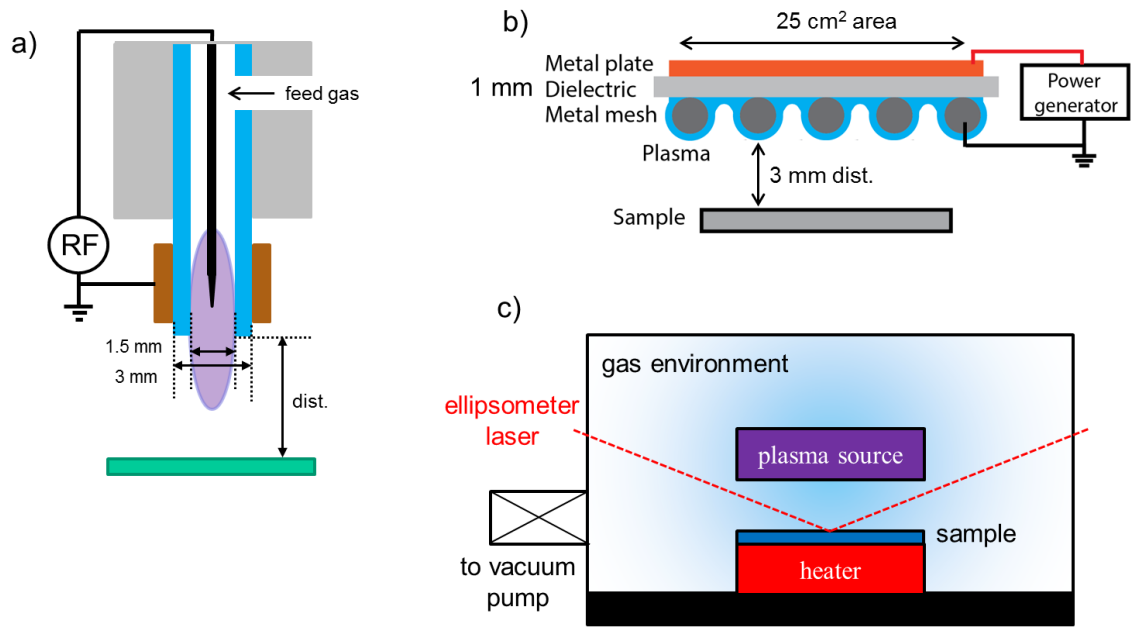

Figure 4.1: a) Schematic designs for RF jet, b) schematic design for SMD, and experimental chamber setup with ellipsometry and gas control.

The MHz driven APPJ source was designed by Bruggeman *et al*. and has been extensively characterized[38,32,39] and is shown in figure 4.1 a). The design uses a 1 mm diameter tungsten pin electrode mounted inside a quartz tube (1.5 mm inner diameter (ID) and 3 mm outer diameter (OD)) with a grounded copper ring electrode (5.3 mm length, 3 mm ID). The original design is based on the atmospheric pressure plasma jet proposed by Park and Selwyn.[87] The standard operating conditions of the MHz jet are a 13.5 MHz modulated driven frequency with a 20% on/off duty cycle (20% on time, 80% off time), a time-averaged power dissipation of 2 watts, a gas flow of 1.5 slm (which corresponds to a gas velocity of 3.5 m/s), and a distance from jet nozzle to sample that ranged from 8 mm to 16 mm. Details of how the power was calculated for this source can

be found in previous work.[40] Operating conditions were kept as close to previous work as possible to make the conditions comparable.[82,81]

The kHz driven surface microdischarge source (SMD) is shown in figure 4.1 b). The powered electrode is a 25 cm^2 square copper plate, the ground electrode is a stainless steel mesh with 50% of opening, and a 1.6 mm-thick quartz plate separates these electrodes. The source is operated at 42 kHz, 6 kVp-p applied voltage using a PVM500 power supply, in ambient air, with 3 mm distance from the metal mesh to the sample. The SMD style source, due to its different design and operation, operates at about 6.5 watts total dissipated power but over a much larger area of discharge compared to the MHz-driven APPJ source. The design of this source is based on the work by Morfill.[78] There is a wealth of literature looking at sources similar to this one for use in disinfecting surfaces. Li, Y. et al. (2012) shows a several log reduction in colony forming bacteria units from as little as 2 seconds of treatment operated in ambient air.[88] Maisch, T. et al. (2012) uses a surface microdischarge source to look at the disinfection of several varieties of bacteria in ambient air.[89]

4.2.2 Experimental Setup

This work was conducted by placing the atmospheric pressure plasma sources in a sealed chamber in order to accurately control the ambient environment surrounding the plasma source. The chamber was pumped to remove ambient air and then refilled with nitrogen or oxygen gas depending on the experiment. The ellipsometer is mounted on this sealed chamber to monitor the sample properties during treatment or immediately post treatment. A custom built heating unit was installed into the chamber that utilized a thermocouple to monitor sample temperature and a proportional–integral–derivative (PID)

controller to keep the temperature of the sample at a precisely controlled value. The APPJ plasma source is mounted on a custom built x and y-axis stage[81,82] to uniformly treat a large area of polymer so that the sample properties can accurately be measured using ellipsometry. This x-y axis stage was tested in this previous work to ensure that the sample area was uniformly treated.[82] The SMD plasma source was mounted on a custom built z-axis stage to precisely control the height of the SMD above the polymer sample and to move the SMD to allow for ellipsometric measurement immediately following sample treatment. The SMD treatments are generally done for 7 minutes and the APPJ source was scanned over the surface at a speed of 2.4 mm/s.

4.2.3 Materials

A PMMA-based 193 nm photoresist (PR193) thin film polymer of 140 nm thickness was used for the apparent activation energy and etching behavior study. A stacked structure of photoresist, Si-containing Anti-Reflective Coating (SiARC) hard mask, organic planarization layer (OPL), and tetraethyl orthosilicate were used to investigate etching directionality. This polymer film was used to provide comparisons to literature values in similar etching studies at low pressure[90,61] and because its behavior is generally similar to PMMA films[91] which are common to numerous applications.

4.2.4 Characterization

The APPJ has been characterized to show the flow dynamics,[72] gas temperature,[40] electron density,[72] density of NO,[92] and O.[93] The electrical behavior of the SMD plasma source as well as the types of reactive species that it produces has also been characterized.[94,83]

Ellipsometry was conducted in situ and ex situ using an automated rotating compensator SOFIE STE70 ellipsometer in the polarizer-compensator-sample-analyzer (PCSA) configuration using a He-Ne laser (λ = 632.8 nm) at a ~72° angle of incidence. The measurement of amplitude ratio after reflection (psi) and the difference in the phase shift (delta) are converted into film thickness and modification through multilayer optical modeling.

X-ray photoelectron spectroscopy (XPS) characterization was done using a Vacuum Generators ESCALAB MKII system for surface chemical composition analysis. High resolution spectra of the C 1s, N 1s and O 1s were obtained at 20 eV pass energy at an electron take-off angle of 20° with respect to the sample surface to look only at the sample surface. Samples were transferred through air environment immediately following plasma treatment and were scanned within ~30 minutes following treatment.

Scanning electron microscopy (SEM) analysis was done to investigate damage done to polymer surfaces as well as to determine the directionality of etching for the patterned samples. The analysis was performed on a Hitachi SU-70 Schottky field emission gun scanning electron microscope and was done at the Maryland NanoCenter AIMLab. The combination of top down and cross sectional images allows for analysis of 3 dimensional trench structures.

4.3. Experimental Results

4.3.1 Activation Energy for APPJ

The room temperature etching of the APPJ source was investigated at various plasma conditions before the effects of increasing temperature were investigated and is displayed in Figure 4.2 a). The etching behavior of the APPJ changes significantly with feed gas chemistry, distance, and local environment interactions which are critical to understand prior to understanding the sample temperature effect.

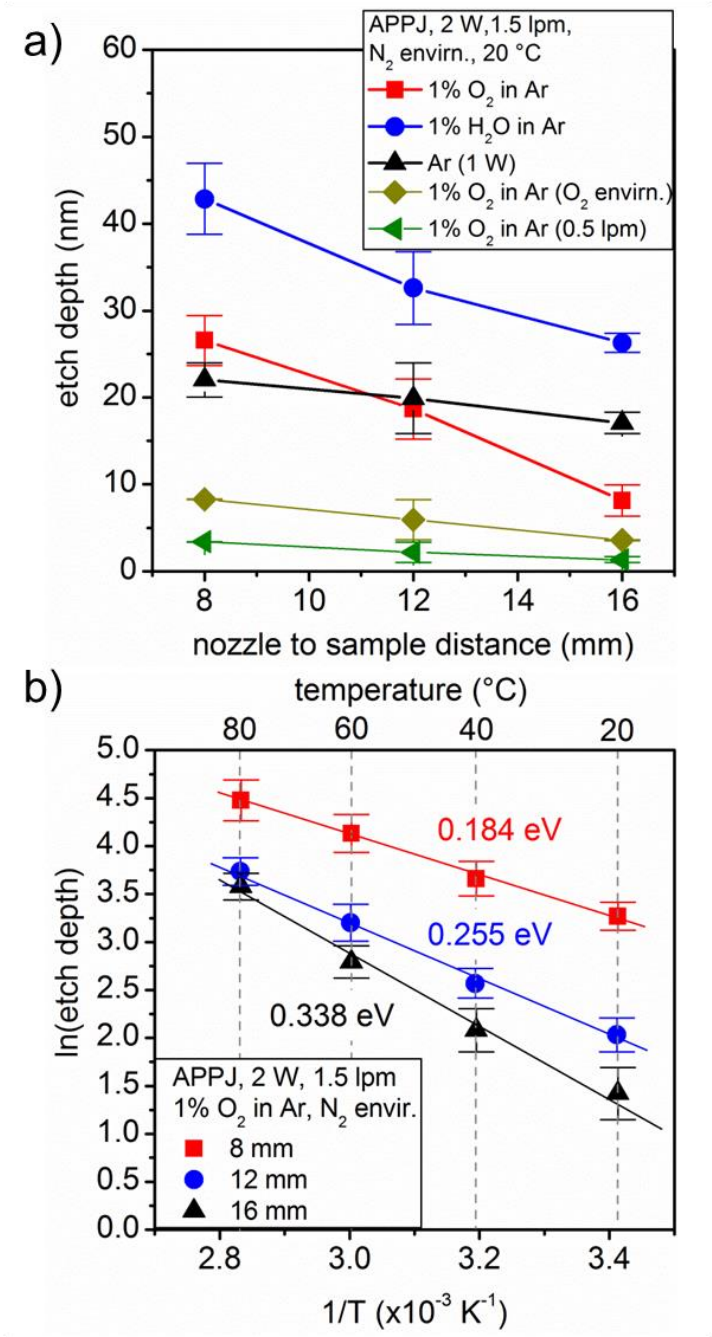

Figure 4.2: a) Etching behavior of PR193 by APPJ at room temperature for various feed gas chemistries and different feed gas flow rates and local environment gas chemistries. b) Example Arrhenius plot of log of etch depth vs 1/ temperature for APPJ treatment and showing activation energy relationship to slope for one condition.

All conditions show a nearly linear decrease in etch depth with increasing treatment distance from 8 mm to 16 mm in a controlled N_2 environment. The magnitude of etching caused by 1% H_2O admixture to Ar is greater than the 1% O_2 admixture and the pure Ar feed gas chemistries. The pure Ar chemistry plasma power had to be decreased from 2 Watts to ~1 Watt in order to shorten the plasma plume length to a similar magnitude as the 1% admixtures, though the Ar plume length was still slightly longer than 4 mm. Pure Ar shows a smaller rate of thickness loss with increasing distance compared with the 1% H_2O and O_2 admixtures which have very similar magnitudes in the loss rate. This could be due to the slightly longer plume length which would likely involve charged or metastable species causing the brunt of the etching here since there should be very little if any oxygen based species for this case. For the 1% O_2 admixture changing the environment to pure oxygen gas significantly decreases the etch depth. [81]

This etching behavior is likely due to reactions of atomic oxygen produced in the plasma plume with surrounding oxygen in the gas phase which produce ozone that is less oxidative than atomic oxygen and therefore causes less etching.[81,95] For a pure N_2 environment, this reaction pathway does not exist and therefore the atomic oxygen can have a longer effective mean free path. Lowering the gas flow rate from 1.5 lpm to 0.5 lpm also greatly decreases the etch depth. The reduction of flow rate did not have an impact on the plasma jet plume length for the oxygen admixture cases. Additional information on the behavior of the APPJ source at room temperature has been published in more detail elsewhere.[81,82]

The etch depth of the polymer films rises with increasing temperature. This has also been shown for low pressure plasma treatment of polymer films.[96,97] The apparent

activation energy is derived from the overall etch rate of the polymer film which involves multiple reactions. This is obtained using an Arrhenius rate equation:

$$\boldsymbol{k_{ER} = A_{ER} \cdot exp(\frac{-E_a}{k_b T})} \quad (4.1)$$

In this equation k_{ER} is the rate constant for the overall etching reaction which we assume to be proportional to the etch depth of the polymer films. For this etching reaction, it is assumed that the etching reaction that occurs for the polymer films is a activated surface process for neutral gas species. Therefore an exponential dependence on temperature is expected as shown in equation 4.1. From this equation the activation energy E_a can be extracted from the slope of an Arrhenius plot which consists of the log of the etch depth vs. *1/T*.

The apparent activation energy is related to the contribution of thermal energy to the etching process. If there is only one etching species produced by the plasma source then the activation energy should not change with changing plasma conditions such as distance, gas flow rate, and gas chemistry. By using polymer thin films that have been investigated at low pressure the apparent activation energy seen from that work can be compared to the apparent activation energy achieved from the atmospheric pressure plasma sources. Lower apparent activation energy is directly related to the presence of higher energy species which more easily break the carbon backbone bonds that give rise to etching. The change of etching activation energy by adding more energetic species has been studied fairly extensively at low pressure plasma systems, particularly for the addition of fluorine to oxygen plasmas.[86,98,97,84]

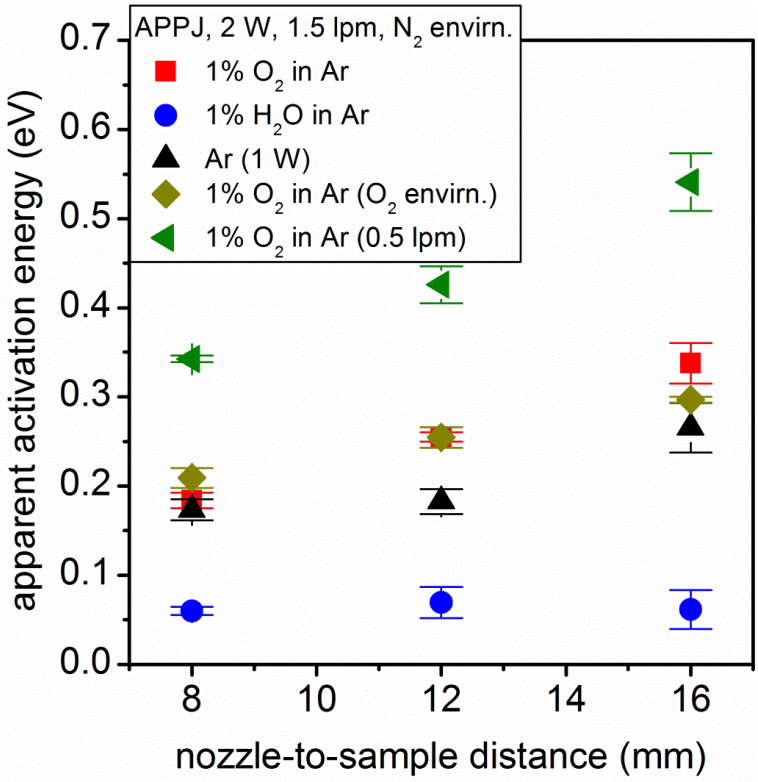

Figure 4.3: Apparent activation energy vs nozzle to sample distance for various APPJ feed gas chemistries and various environment gas chemistries and feed gas flow rates.

The apparent activation energy calculated from an example Arrhenius plot for 1% O_2 in Ar is shown in figure 4.2 b). The temperature range of the experiments is from 20 °C to 80 °C. It is clear from this plot that the activation energy is increasing with increasing treatment distance. The calculated apparent activation energy for each distance and plasma condition is shown in figure 4.3. The 1% O_2 admixture shows a distinctive increase from 0.18 to 0.34 eV over an 8 mm to 16 mm distance. Changing the local environment to oxygen from nitrogen had very little effect of the activation energy for 1% O_2 admixture. However, decreasing the flow rate from 1.5 lpm to 0.5 lpm increased the apparent activation energy for 1% O_2 admixture, though the trend with distance

stayed the same, increasing from 0.35 eV at 8 mm to 0.54 eV at 16 mm. 1% H_2O admixture shows low apparent activation energy for all distances compared with all other conditions.

4.3.2 Activation Energy for SMD

The SMD source operates in a significantly different manner than the APPJ source. The plasma produced is contained around the grounded mesh without a directional gas flow toward the surface so there is no plasma plume and it relies on diffusion for species transport. The SMD plasma source shows a thickness increase at room temperature and causes etching once the temperature is increased to approximately 60 °C. The complete thickness change of the polymer film for SMD treatment conditions is shown in figure 4.4 a). The maximum effect at all temperature is seen for the 15% N_2 in O_2 gas chemistry condition. This corresponds also to the gas chemistry that causes the maximum surface modification condition seen in previous work by the same plasma source.[17] Etching occurs in increasing amounts above 60 °C, whereas below this temperature some thickness increase is seen for the SMD treatment. This thickness increase falls off once treatment has stopped in an exponential manner with respect to time. The thickness falls to consistent value within ~2 minutes following the end of the treatment and this occurs regardless of temperature. The only condition that does not show any thickness increase is for the pure N_2 gas chemistry condition; however this condition still shows etching at higher temperatures. Figure 4.4 b) shows the distance effect of SMD treatment for the 15% N_2 in O_2 gas chemistry condition. Etch depth falls off exponentially with distance in contrast to the distance behavior observed with the APPJ source. This is likely explained by the lack of a convective flow and is discussed

later in the discussion section. In the case of the SMD, the apparent activation energy of the etching reaction was only measured for 3 mm distance because the etching effect falls off so rapidly with distance that the activation energy was too difficult to measure accurately.

Calculation of the apparent activation energy for the SMD source was done in the same manner as for the APPJ over the range of temperatures from 60 °C to 90 °C. The Arrhenius plot showing the calculation of the activation energy is seen in figure 4.5 a). The appearance of the slopes is fairly similar over all treatment conditions. The calculated apparent activation energy is shown in figure 4.5 b) for all gas chemistries explored. The activation energy for conditions containing oxygen is in the range of 0.8 to 0.9 eV with little change. This activation energy drops slightly for the pure N_2 case.

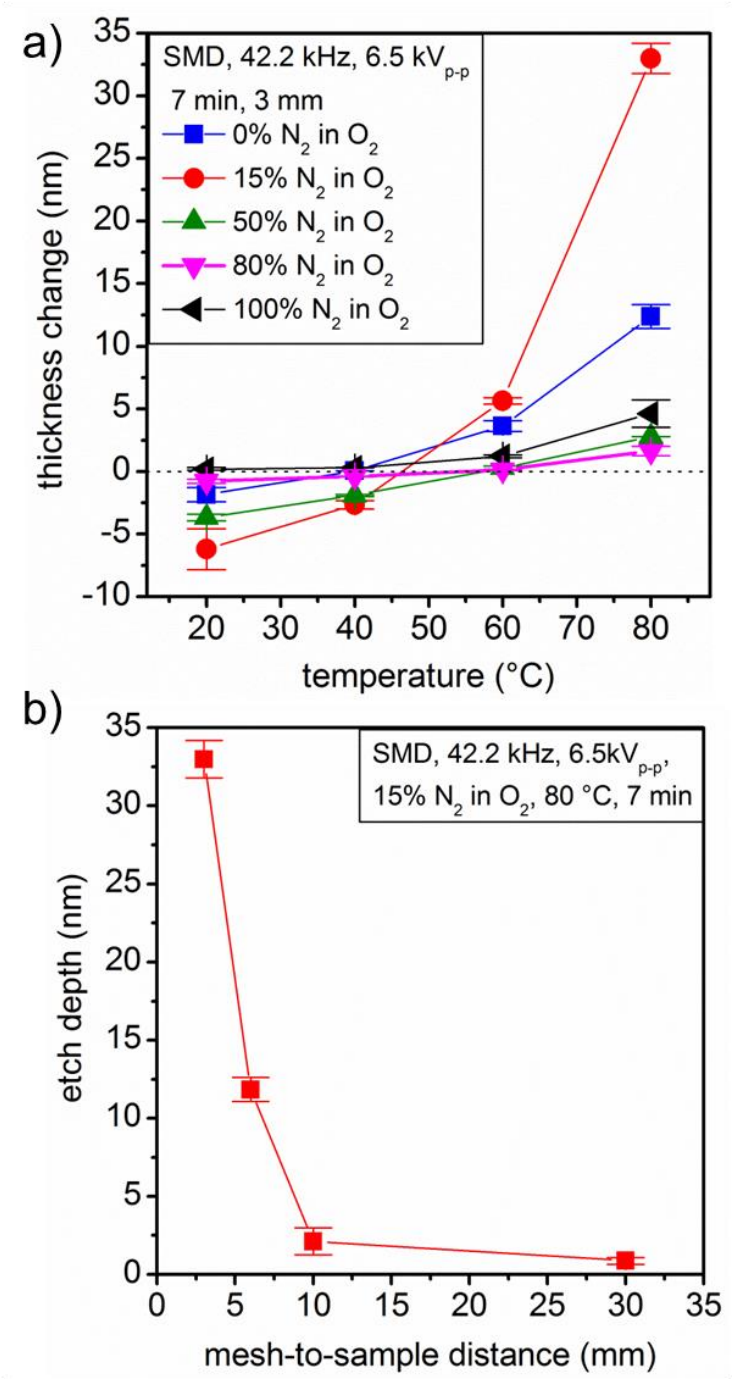

Figure 4.4: a) SMD treatment of PR193 at 20-80 °C for different gas chemistries and b) SMD treatment over various distances for most etching condition.

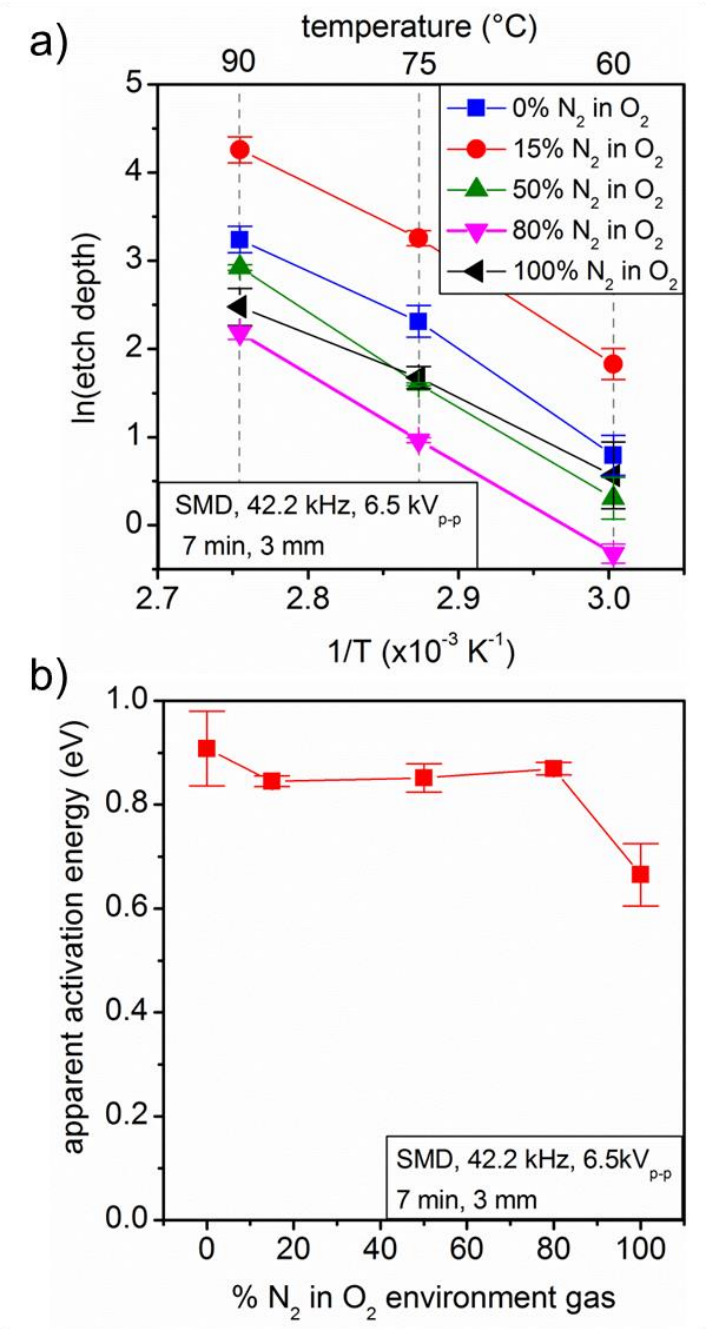

Figure 4.5: a) High temperature (60-90 °C) Arrhenius plot of SMD treatment and b) apparent activation energy (Ea) of SMD for various N_2:O_2 gas chemistries.

4.3.3 Etching Directionality

The directionality of the etching of the APPJ and the SMD plasma sources was investigated using three dimensional structured samples as described in the materials and methods section. The goal of using these samples was to examine the etching behavior in both the vertical and lateral directions of a polymer photoresist layer above the hard mask layer and an organic planarization layer located under the hard mask layer. A schematic of the SEM cross section image of an untreated stack sample is shown in figure 4.6 a). In this schematic, the PR is the photoresist, the SiARC is the hard mask layer, and OPL is the organic planarization layer.

The etching behavior of the APPJ source shows some anisotropy depending on the treatment conditions. Figures 4.7 a) and b) show the cross sectional SEM images for two example treatment conditions for the APPJ source treatment. Figure 4.6 b) show samples treated at 8 mm distance and at 20 °C. These conditions show a vertical etch depth of 13.3 nm with an undercut etch of 6.0 nm. However, when the treatment distance is increased to 16 mm and the temperature increased to 80 °C as shown in figure 4.6 c) the vertical etch is 15.5 nm compared to an undercut etch of 12.8 nm. The APPJ treatment conditions for the OPL and PR layer are shown in figure 4.7 a) and c) respectively. Here we see that the ratio of lateral to vertical etching increases with increasing treatment distance and temperature. This data suggests that there is anisotropic etching for the APPJ source that becomes more isotropic with increasing treatment distance.

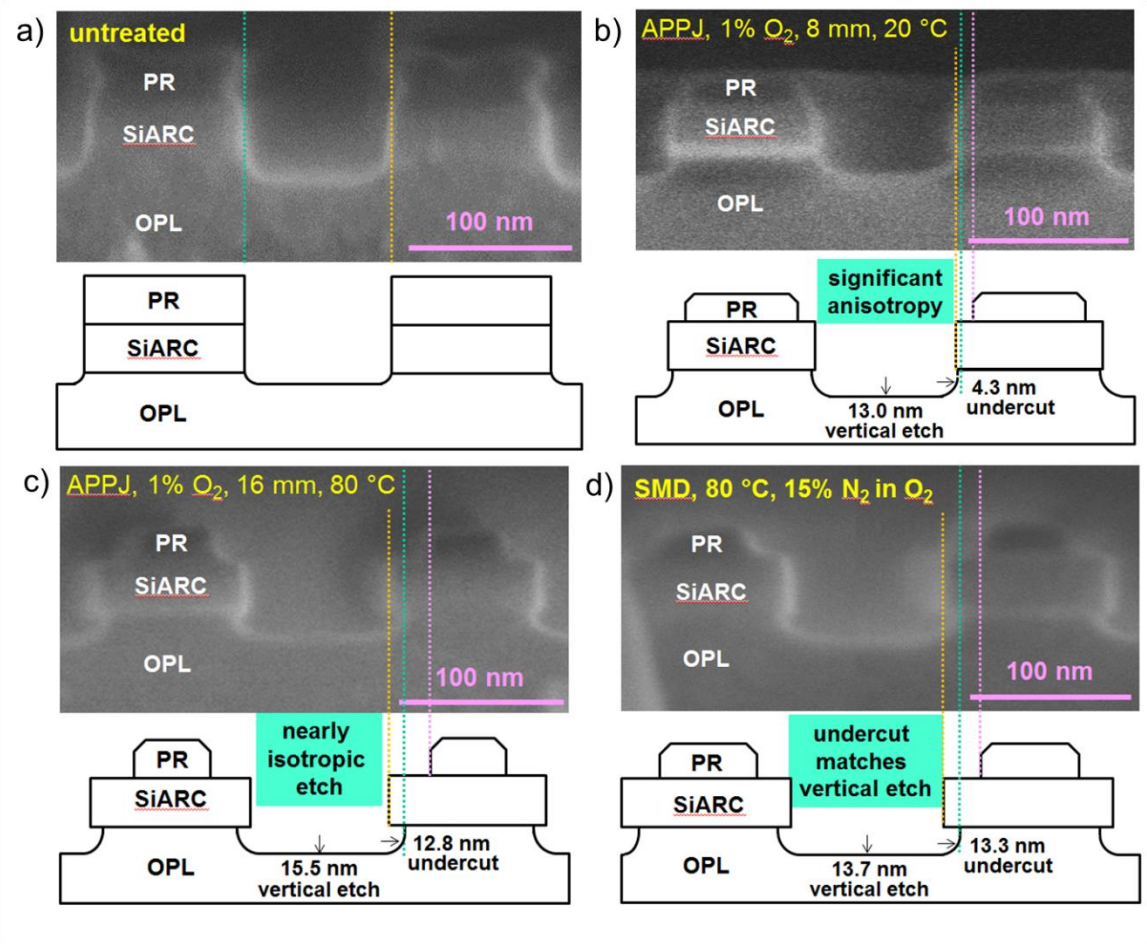

Figure 4.6: a) untreated patterned sample with 100 nm trench feature taken by SEM, b) example SEM image of APPJ treatment showing most anisotropy, c) example SEM image of SMD treatment showing most isotropic condition, and d) example SEM image of SMD treatment showing top down etch and undercut etch.

The etching behavior of the SMD source is generally isotropic. Figure 4.6 d) shows an example cross sectional SEM image for SMD treatment at 15% N_2 in O_2 gas chemistry at 80 °C and 3 mm distance. For this condition we see an average vertical etch depth directly between the trench structures of 13.7 nm and we see a lateral etch depth

under the hard mask, also known as undercutting, of 13.3 nm. The SMD treatment of the three dimensional structures samples ratio of undercut to top down etching for both the OPL and PR layer are shown in figures 4.7 b) and 8 d) respectively. We see that the ratio of lateral to vertical etching is approximately 1 for all treatment conditions which is characteristic of isotropic etching.

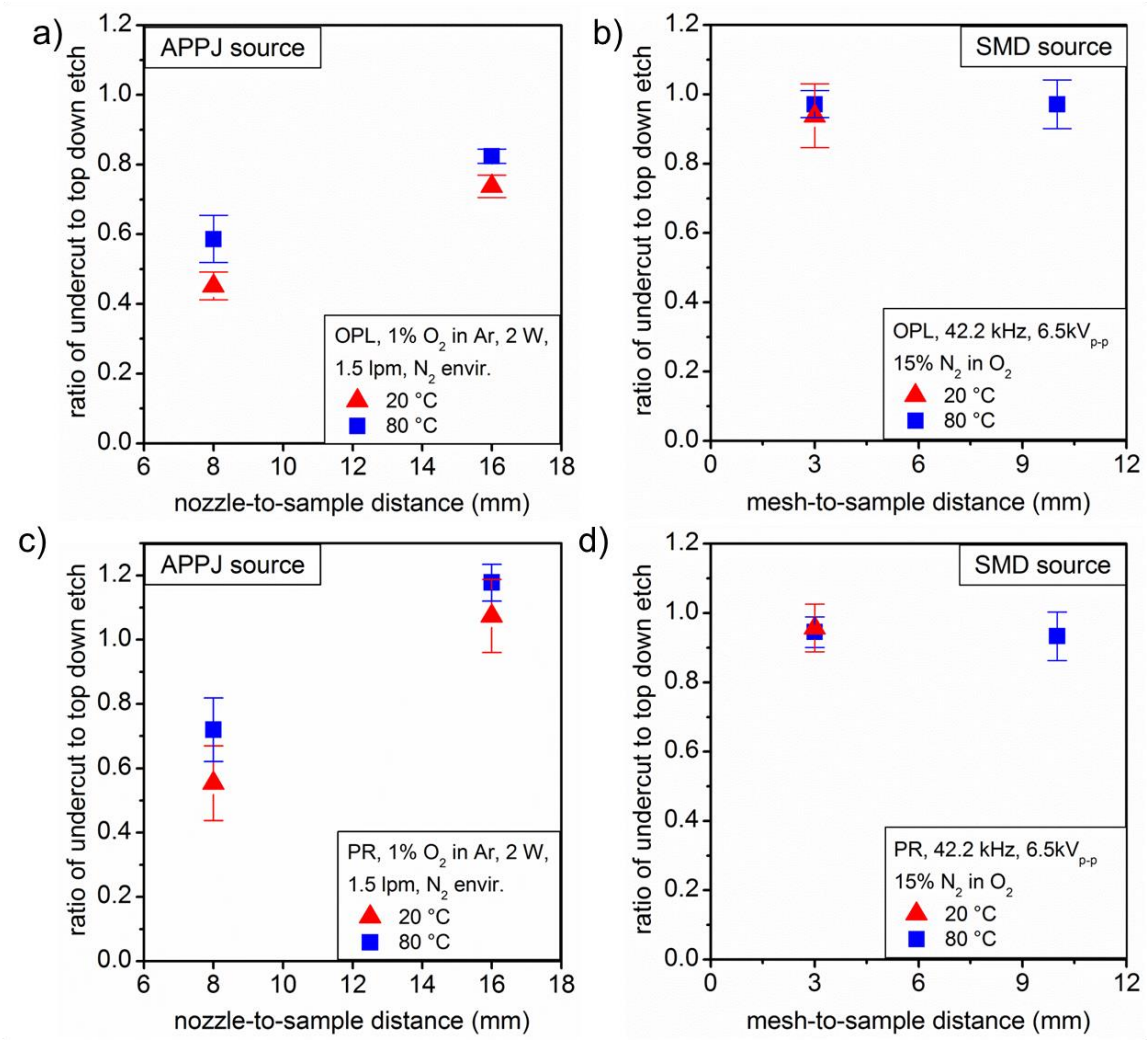

Figure 4.7: APPJ treatment of patterned samples showing ratio of lateral to vertical etch depths of organic planarization layer for various treatment conditions.

4.3.4 Surface Chemistry

The surface chemistry was measured using XPS directly following plasma treatment of polymer films. The first critical example of this was demonstrated in previous work on these plasma sources and is summarized in figure 4.8. The previous work compares the surface chemistry of a model polymer directly after treatment by both sources.[15] It is clear that the SMD treatment creates significantly more oxidation in general as can be seen by the reduction in the C1s spectrum C-C/H bonding and increase in the O1s spectrum total counts. Additionally, a peak appears in the N1s spectrum at a 408 eV binding energy that corresponds to NO_3 attachment to the surface. The difference in surface chemistry along with the large variation in etch rate suggests that the etching mechanism must be different between the two plasma sources.

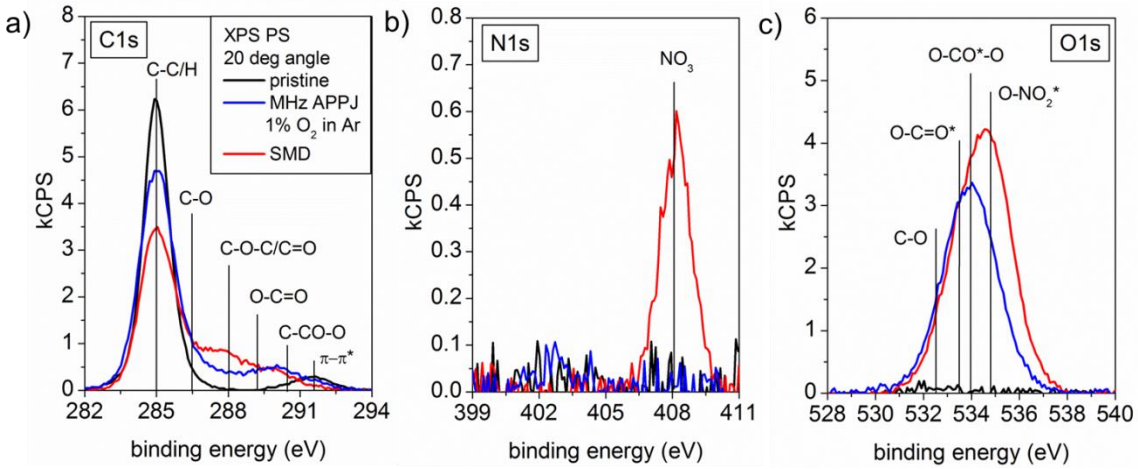

Figure 4.8: Comparison of MHz APPJ and SMD surface chemistry changes showing high resolution spectrum of a) C1s, b) N1s, and c) O1s.

The SMD surface chemistry is measured post treatment for low and high temperature treatments at the same gas chemistry to highlight the difference between etching and non-etching cases. Figure 4.9 shows this comparison of the surface chemistry after SMD treatment at 20 °C and 80 °C. The surface chemistry at the lower temperature shows very high amounts of surface oxidation. In particular the total counts of the O1s spectrum are significantly higher than the pristine sample as well as the addition of a peak corresponding to NO_3 in the N1s spectrum. When the treatment is done at higher temperature and etching takes place at a rate of up to 5 nm/min the amount of oxidation is less and closer in magnitude to the pristine samples. However, the total amount of the NO_3 peak stays the same at both temperatures.

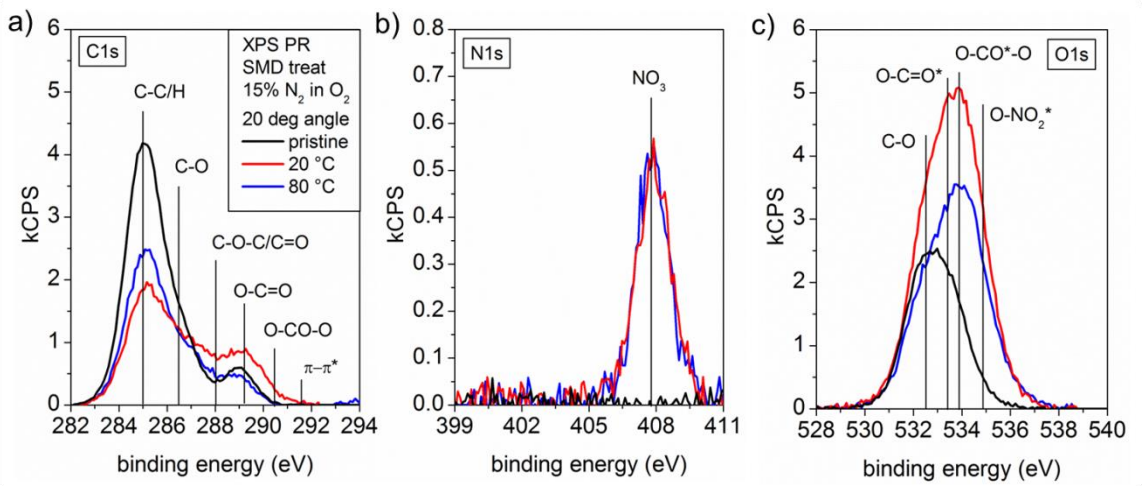

Figure 4.9: XPS of SMD treatment at varying temperatures showing high resolution spectrum of a) C1s, b) N1s, and c) O1s.

The APPJ surface chemistry was also measured post treatment for low and high temperature treatments under the same operating conditions, The results of these

treatments are shown in figure 4.10. The higher temperature treatment shows a decrease in oxidation which can be seen in both the C1s and the O1s spectrums respectively. This coincides with an increase in the etching amount that occurs during this same temperature increase similar to the surface oxidation behavior seen for the SMD source. It should be noted that surface chemistry of the photoresist material shows a small concentration of fluorine in addition to the carbon, oxygen, and nitrogen species. For the pristine polymer this concentration is around 1 % of the total XPS counts. Following treatment this concentration increases to a maximum of 7% of the total XPS counts. Contamination from the APPJ treatment or from XPS analysis chamber has been discounted since no fluorine peaks are seen for polystyrene samples treated and measured during the same time period. We believe this increase seen is due to a buildup of fluorine from the bulk polymer on the surface as carbon and oxygen species are being etching away while the fluorine from the sample is not. Therefore this fluorine percentage should scale with the amount of total etching that has occurred, which is what we see for the two cases shown in the data in figure 4.10. Due to the low concentration of fluorine, it is unlikely that the fluorine has a significant impact on the value of the apparent activation energy measured and/or etching behavior of the polymer.

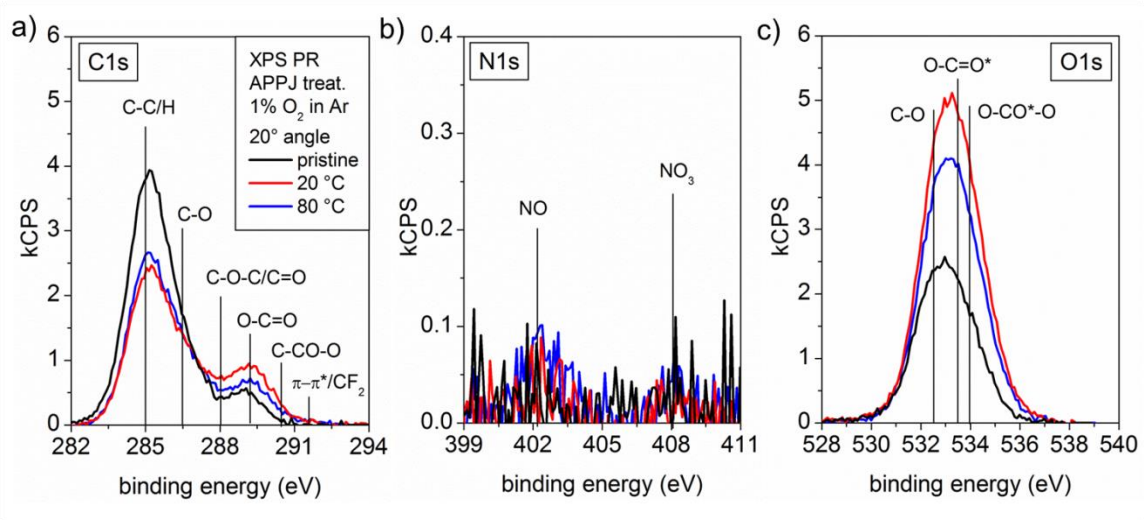

Figure 4.10: XPS of APPJ treatment at varying temperatures showing high resolution spectrum of a) C1s, b) N1s, and c) O1s.

4.4. Discussion

The APPJ and SMD plasma sources interact with polymer surfaces in very different ways. The APPJ source is operated in the MHz regime utilizing a 20% on, 80% off duty cycle to maintain a low operating temperature. The APPJ requires primarily noble feed gas, in our case Ar, with typically 1% of reactive gas admixture to change the chemical species produced. The primary transport mechanism for the APPJ source is convection of the gas flow toward the sample and the plume chemistry is typically influenced by small amounts of diffusion of gas from the ambient gas chemistry into the plasma plume that extends toward the surface. The extended plume, due to the combination of noble gas flow and strong electric field, contributes to the unique behavior seen for the etching of materials by the APPJ. The SMD source, besides using

O_2/N_2 chemistry, is operated in the kHz regime which gives many distinct breakdown events per voltage cycle similar to a corona source. The SMD operates by ionizing the air or local environmental gas that is directly near the grounded mesh electrode. This source relies entirely on diffusion to transport reactive species from the plasma region to the sample as there is no active gas flow involved.

It is clear that the mechanisms for etching are different between these two sources due the ability of the APPJ to etch at room temperature compared to the SMD. Additionally, the surface chemistry clearly shows that different mechanisms are occurring which lead to the vastly increase surface oxidation for the SMD following treatment. It should also be noted that for all this work the visible portion of the plasma produced by either source is not in contact with sample surface, a configuration which we refer to as remote plasma treatment regime. This allows us to compare the work more directly to remote low pressure plasma treatments[84] where the samples are removed from the visible glow regime of the plasma at low pressure as well. When the visible portion of the jet plasma plume is in direct contact with the surface of a polymer sample we see a distinct pattern emerge. This is characterized by impacts of electrical filaments on the surface which leave behind damage areas and lead to highly non-uniform etching of the polymer based around where these filaments strike the surface.[62] For the treatments conducted by the APPJ in this work, this clearly destructive mode of interaction with the surface is checked for and avoided so that we can rule out filament effects for the explanation of the experimental results.

4.4.1 APPJ Behavior

The etching behavior of the APPJ can be explained by the production of reactive chemical species. For instance, the effect of local environment has been explored in detail previously[81] and described how additional oxygen in the environment may react with chemical etching species produced in the jet to reduce the overall effectiveness of etching. One of the primary etching species produced by the MHz APPJ is atomic oxygen and it has been shown to correlate well with polymer etching.[81] Additionally this work shows how oxygen present in the local environment causes the total etching of the APPJ to drop which is likely due to atomic oxygen reacting with the local oxygen in the environment to produce ozone. However, it should be noted that an oxygen environment may also reduce the path length of some charged species as well. Oxygen is an electronegative gas and has a strong electron affinity which may reduce the plasma density. For instance, a streamer breakdown process is always influenced by the presence of an electronegative gas due to the reliance on electrons to propagate.[99] This may also contribute to the reduction in etching seen for an oxygen environment in the case of the MHz APPJ etching. Additionally, we see that water addition to the plasma increases the effectiveness of etching at room temperature which is likely due to the higher reactivity of OH species by about two orders of magnitude compared with O reactive species.[100] Previous work using the MHz APPJ has correlated the amount of measured atomic oxygen produced to the amount of carbon removal due to etching for a number of polymer films.[81]

4.4.1.1. Activation Energy of APPJ Etching

The simplest assumption therefore is that the polymer etching would be due entirely to chemical etching species for situations where the visible plume of the jet is not in contact with the polymer film. One would then expect the APPJ to behave very similarly to a remote low pressure oxygen plasma, which is entirely due to chemical reactive species etching. Indeed this is the assumption that is made by several previous works on APPJ sources which correlate reactive neutral species with etching amount.[101,19] However the apparent activation energies that are found for the APPJ are different from published values for low pressure work. For low pressure remote oxygen plasma treatments, the measured apparent activation energy values for the photoresist thin film polymer used in this work are approximately 0.5 eV.[84] The cited work states that this should primarily be due to atomic oxygen and related chemical species, the same primary reactive species that have been well characterized for the APPJ source.

Therefore, because the activation energies for the typical oxygen admixture plasma treatment in this work are much lower than this value, and also depend on treatment distance and other source operating parameters, O atoms alone cannot explain our observations. Next to O atoms, one or more additional species must be playing a role in the etching seen. Because activation energy represents the amount of thermal energy required to induce significant etching, a lower activation energy suggests that the etching process seen here does not require as much thermal energy. This means that the etching mechanism must involve species that have greater energy than atomic oxygen.

The apparent activation energy also increases with increasing treatment distance. If the etching were due to a single species then the activation energy should be constant with changing distance as the etching change with thermal energy input would stay consistent. This suggests that as distance increases, the species causing etching are changing in relative importance, and the results indicate that the more energetic species that contribute to etching decay at a faster rate in the plasma effluent than the less energetic etching species. Lowering the flow rate would significantly increase the fraction of ambient gas that diffuses into the plasma jet plume which could then change the dynamics of the discharge.

4.4.1.2. Directionality of APPJ Etching

The directionality of the etching suggests that there is a directional component to the etching seen from the APPJ source, which is absent polymer etching induced by the SMD source. This directionality is seen for both polymer film layers in the stacked patterned samples. Specifically, directionality refers to there being more etching in the line-of-sight-of-source direction compared with the lateral shrinking of the photoresist layer or the undercut etching of the OPL layer under the hard mask layer. The amount of directionality of etching changes for the APPJ source with changing sample to nozzle distance. This behavior suggests that the species which are contributing to the directional etching is falling off more quickly with distance than the species causing the isotropic etching. This observation further supports what has been seen for the activation energy: that the ratio of different reactive species contributing to etching is changing over our treatment distances studied. There are several possibilities for what these directional species may be but there is currently no direct evidence that could be used to identify it

(them). Possibilities include high energy photons, which are unlikely due to the reasons discussed below, or charged species moving toward the grounded substrate below the sample.

4.4.1.3. Photon Directionality

Photons are known to cause significant directional modification of the polymer films studied in this work based on low pressure plasma processing experiments which can lead to an overall thickness reduction in the films.[70,102] At atmospheric pressure, high energy photons are known to cause a directional-effect based on line of sight to the plasma source and has been suggested to contribute to applications such as bacteria disinfection.[58] However, it is unlikely that the enhancement of the APPJ etching at closer distances is due to photons. While the MHz APPJ source has been shown to produce some VUV photons, the addition of oxygen to the feed gas typically quenches the photon effect seen at the surface.[79] Additionally, the modification of photoresist by high energy photons leaves a very distinct densification of the polymer film which is not seen in the ellipsometry data for this etching.

Photons with wavelengths higher than 140 nm have been shown in previous work to not directly cause modification of the polymer film used in this study. However, it is still possible that lower energy UV photons may contribute to the etching process through hydrogen abstraction or other processes. This lower energy UV light would still have the same directional effect as higher energy photons so it is possible that the results seen are due to UV enhanced chemical etching of the polymer film. These higher wavelength UV photons could be produced by collisions of atoms or molecules.

4.4.1.4. Charged Species Directionality

The MHz APPJ, however, has a gas flow which helps carry reactive species to the surface, though over a larger distance of 8 to 16 mm. The gas flow is held constant at 1.5 lpm which gives a gas velocity of the jet of approximately 14 m/s. This corresponds to a travel time from the exit nozzle of the APPJ to the sample of 0.57 to 1.14 μs, depending on distance, which is several orders of magnitude shorter travel time than the SMD. While one could consider that there may be a contribution from the convection of the gas flow from the APPJ source since this gas flow is directional to some degree, based on gas flow kinetics for a laminar flow, this Ar flow stagnates approximately 1-2 mm above the top of the sample. This result was found as part of a finite element model of the APPJ gas flow which are described in previous work.[79] This would suggest that the Ar gas flow should cease to contribute to the directionality of species once it reaches this point.

Charged or other high energy reactive species seem to be the more likely candidate for contributing to the enhanced etching of the APPJ source at close treatment distances. These charged species seem to be present most significantly at closer distances and then the flux to the surface falls off significantly with distance due to the increasing activation energy and decreasing directionality of etching. Charged species have been measured for this exact plasma source beyond the visible plasma plume.[80] By using molecular beam mass spectrometry it was possible to measure positive ions out to 10 mm from the nozzle of the jet which falls within the treatment range of our samples in this work making them a possible candidate for the cause of the directional etching. Another work suggests the charged species may be able to permeate significant distances from various APPJ sources. Sobota, A., et al. measured the electric field from a He APPJ and

showed that it increased to a maximum point approximately 8 mm from the exit of the tube though this varied with gas flow and other parameters.[103] Additionally it should be considered that if charged species are responsible for the enhanced etching at room temperature then the sample may become charged over the duration of the APPJ treatment. Because the polymer film is an insulator, the charged species arriving at the surface may contribute to charging which may then influence the electric field in the vicinity of the treatment area.[104] Ionization waves produced by APPJ sources have been measured at upwards of 10 km/s travel velocity, significantly higher than the surrounding gas flow and suggesting that the plasma is greatly accelerated due to the electric field generated within the plasma source. For this specific APPJ source used in our work these ionization waves have been measured at 30 km/s.[105] Overall the most critical takeaway from the APPJ research is that there must be a directional energy flow to the polymer surface. This may be due to kinetic/potential energy deposition at the surface, e.g. by accelerated ions or electrons or due to high energy photons.

4.4.2 SMD Behavior

The etching behavior of the SMD is much more consistent with a neutral reactive species causing both surface modification and subsequent etching which only occurs at higher temperatures. The plasma source design is more consistent with keeping the plasma contained to a small area while still creating reactive species. The SMD has been characterized for several reactive species measured at the surface of the active electrode for the plasma source such as 500 ppm O_3, less than 1 ppm NO, ~3 ppm NO_2, and 25 nW/cm^2 UV photons (all within the UVA spectrum).[89] This paper also mentions the presence of O and OH in small values that are not measured. Sakiyama, Y. et al. 2012

also uses a surface microdischarge to investigate the species produced by it through modeling and measurement using FTIR for humid environments.[83] They find the evidence of O_3, HNO_3, N_2O, and N_2O_5 from FTIR measurements and hypothesis the presence of H_2, H_2O_2, and NO_3 in addition to the measured species using modeling.

Our experimental results show when at room temperature there is only a thickness increase of the polymer films that is of a smaller magnitude than the eventual etching seen at higher temperatures. The ambient gas chemistry changes the amount of observed surface chemical changes and these changes correlate very well with the thickness increase of the polymer films seen at room temperature for SMD treatments. The fact that there is such significant surface chemical modification along with a thickness increase for room temperature treatment suggests that species are being adsorbed on the polymer surface from the plasma treatment, and chemically react. These species likely have enough energy to adsorb and cause chemical changes but not complete the last step in the etching process which is desorption of the product which is needed for thickness loss. The fact that at room temperature the species produced by the MHz APPJ and incident on the polymer surface have more energy than the species produced by the SMD, as evidenced by high-speed etching and the much lower activation energy that characterizes polymer etching for the APPJ.

The absolute activation energy seen for the SMD is significantly higher than the experimentally found 0.5 eV for low pressure atomic oxygen systems. This along with the large amount of nitrogen species found to be involved in the surface modification from previous work and also seen here seems to suggest that the primary species produced by the SMD is either NO_x or some combination of NO_x and reactive oxygen

species. This is further supported because the largest amount of absolute etching is when the SMD is operated using 15% N_2 in O_2 which corresponds to the greatest amount of NO_3 species seen bonded to polymer surfaces post treatment using x-ray photoelectron spectroscopy in previous work.[17]

The surface chemistry of the polymer post SMD treatment shows very high amounts of surface oxidation when the treatment is done at low temperatures. When the treatment is performed at higher temperature and etching occurs, the amount of residual oxidation is less and closer to the pristine samples state. This suggests that at room temperature the species produced by the SMD plasma treatment have enough energy to oxidize/nitridize the surface but the degree of modification is insufficient for etching of the polymer. The final step in the etching process, removal of the oxidation product in the form of volatile species does not occur significantly. Instead, what likely occurs is that a once a reactive site is created, the site is oxidized in such a manner that terminates the etching process instead of propagating the reactive site. The original species that created the reactive site likely do not have enough energy to remove this oxidation to allow for etching to occur. The etching steps of adsorption, product formation, and product desorption are theorized and described in detail in the work by Coburn, J. W. and H. F. Winters.[106] The SMD process likely involves the adsorption of etching species which modify the surface which takes up both oxygen and nitrogen species. However the formation of volatile produce is hindered by a lack of energy from these oxidizing species and this allows the NO_x species in the polymer to build up. Etching of polymers is inhibited unless enough energy to activate the etching process is provided in the form of thermal energy.

The SMD source relies entirely on diffusion to transport species produced at the plasma source to the surface, a distance that is fixed generally at 3 mm for most experiments in this work. Based on the average diffusivity coefficients of neutral reactive species which ranges from ~0.1 to 0.2 cm^2*s^{-1} in air[107], the average travel time of the species would be between 0.2 and 0.4 seconds. This travel time is several orders of magnitude longer for the SMD than for the APPJ source. The plasma also is very close to room temperature which means that there is no thermally activated diffusion or convection either. Indeed, the overall surface effect seen for the SMD source drops off very rapidly with increasing distance which is consistent with the diffusion theory.

The response of the SMD to increased temperature which is much greater than the relative effect of changing the local gas chemistry suggests a thermally activated process. One possibility for this temperature response is the activation of chemical reactions which allow for the production of more low molecular weight and volatile species due to the same flux of reactive species to the polymer surface. It is possible that increased evaporation of some low molecular weight species created at the surface at elevated temperature is responsible for this, whereas evaporation rates at room temperature would be very slow and therefore limit loss of polymer material near room temperature. Another important note is that at higher temperatures any ozone flux to the surface may decompose into atomic oxygen which would have an increased oxidation reaction with the polymer surface. Further investigation into the exact nature of this interaction will be carried out in future studies.

The SMD source also creates NO_x species in the gas phase which may contribute to the difference in operating mechanism. These species have been measuring using FTIR

for a similar SMD type source where the authors found that the primary species seen are O_3, N_2O_5, N_2O, and HNO_3 for a humid air environment.[83] In particular, the HNO_3 species are believed to be a key reaction species with water from that work. For SMD treated polymers a pronounced NO_3 peak is seen for polymers following O_2/N_2 SMD treatment. This is in contrast to the species we see produced by the MHz APPJ source. Here the primary species is almost always atomic oxygen depending on the treatment conditions, followed by singlet oxygen, ozone, and then NO at a much lower magnitude.[108] The critical species is believed to be atomic oxygen for this jet because of its high density and behavior change with distance which correlates well with various effects of the plasma treatment.

Nitrogen and oxygen gas mixtures have been studied in some detail at low pressure for the plasma processing of various surfaces. Yun Y. B. et al (2007) studied enhancement of SiO_2 etching by adding NO to a fluorine containing plasma. This enhancement is caused by the removal of oxygen from the SiO_2 to form NO_2 or HNO_3 species which made the formation of the etching species SiF_4 easier.[109] However, in the case of polymers more oxygen is generally required for etching to occur by transforming the carbon into a volatile species so it is possible that this NO_3 acts as a source of oxygen once the temperature is increased. Kastenmeier, B. E. E., et al. (2001) looked at the etching of Si_3N_4 using a NO and F containing plasma. They found that while the NO enhanced the etching reaction, the primary etching product was N_2 which leaves a oxygen molecule on the surface bonded to the remaining Si. It seems more likely that a reaction pathway similar to this occurs for our system where oxygen may be added to the surface from N_xO_y species in the gas phase which leads to the surface oxidation we see from the

XPS results. Fujimura, S., et al. (1990) studied the activation energy of photoresist ashing and showed that adding nitrogen to the gas chemistry did not change the activation energy from 0 to 25% N_2 in O_2 gas.[110]

4.5. Conclusions

The APPJ source has a high etch rate at room temperature with low surface oxidation whereas the SMD source does not etch at room temperature but highly oxidizes the polymer surface. The apparent activation energy and directionality of etching species for a polymer film by two plasma sources has been investigated in order to clarify the origin of the different etching mechanisms. The APPJ source shows an apparent activation energy that increases from ~0.18 eV up to ~0.34 eV with increasing nozzle-sample distance from 8 mm to 16 mm which suggests a change in the etching mechanism over this distance and is lower than comparable values for low pressure plasma etching. The APPJ also shows directional etching at closer treatment distances moving toward more isotropic etching at further treatment distances. The APPJ apparent activation energy and directionality suggests a potential contribution by a more energetic etching species the relative importance of which is reduced as treatment distance is increased. This is likely due to a charged or metastable species which flux falls off a higher rate than other chemical neutral oxygen etching species. The SMD shows a very high apparent activation energy compared to literature values for plasma oxygen etching. Additionally the SMD shows no change in apparent activation energy over different gas chemistries despite a change in absolute etch depth which suggests that the etching mechanism is not

changing. The SMD shows only isotropic etching behavior over all treatment distances. Therefore the SMD treatment is consistent with only neutral reactive etching species. The surface chemical oxidation of the polymer surface post plasma treatment is significantly higher for low temperature treatments than for high temperature treatments. This behavior is also the case for the APPJ treatment as well. The etching behavior shows a competition with surface oxidation which is explained by the etching process occurring through created reactive sites which either are propagated to remove material through volatile products or terminated with oxidative species and hinder the etching process.

4.6 Acknowledgements

The authors gratefully acknowledge financial support by the US Department of Energy (DE-SC0001939) and National Science Foundation (PHY-1415353). We also thank Prof. P. J. Bruggeman, S. Kondeti, C. Li, K.Y. Lin, T. Dabrow, and K. Lin for their helpful discussions and collaborations on this project.

Chapter 5: Understanding Plasma Surface Interactions in Enhancement of Methane Decomposition by Plasma Catalyst Systems

A. J. Knoll, S. Zhang, M. Lai, P. Luan, and G. S. Oehrlein

Department of Materials Science and Engineering and the Institute for Research in Electronics and Applied Physics, University of Maryland, College Park, MD 20742, USA

Draft of this article to be submitted to Journal of Physics: D.

Abstract

Catalyst enhancement by atmospheric pressure plasma is a recently emerging field of research that embodies a complex system of reactive species and how they interact with surfaces. In this work we use a well characterized atmospheric pressure plasma system integrated with a commonly used nickel catalyst material to decompose methane gas by partial oxidation reaction. We use Fourier-transform spectroscopy (FTIR) analysis of the gas phase post reaction to measure the loss of methane and the production of CO, CO_2, and H_2O. We find reduction of methane by both plasma alone, catalyst alone, and an increase with both plasma and catalyst. The production of CO appears to be due primarily to the plasma source as it only appears above 2.5 W plasma dissipated power and decreases as catalyst temperature increases. CO_2 production is enhanced by having the catalyst at high temperature and H_2O production depends on both plasma power and temperature. The catalyst surface is monitored *in situ* using diffuse reflectance Fourier-transform spectroscopy (DRIFTs). Using this technique we differentiate changes which occur on the surface due to heating alone of the catalyst and those which are due to plasma exposure

during catalysis. We see formation of NiO due to heating of the catalyst and is enhanced slightly by having very high power plasma treatment of the catalyst. We also find that both heating and plasma treatment remove absorbed water on the surface of the catalyst. Plasma treatment alone however leads to the formation of carboxylate groups and CO bonded to the catalyst surface. These species both have a regime of plasma treatment where they are formed on the surface and then a higher energy regime where they are significantly removed from the catalyst surface. This research highlights the potential for plasma regeneration of catalyst materials already used for methane decomposition as well as showing enhancement of the catalytic behavior under plasma treatment.

5.1 Introduction

In this work we seek to obtain an understanding plasma-surface interactions related to the emerging CAP application of enhanced catalytic reactivity by plasma exposure.[20,111] Atmospheric pressure plasma synergistic enhancement of catalysts is a recently emerging field of research with potential for reducing catalyst energy demands, allowing new materials to be used as catalysts, and even regeneration of catalysts currently used catalyst materials to extend their lifetimes. The study of atmospheric pressure plasma sources interacting with polymer surfaces has been shown to be critical to the understanding of applications and leading guided improvement of these applications based on this increased understanding. This emerging technology has so far been applied to several applications toward environmental solutions such as the destruction of chlorofluorocarbons,[111] removal of volatile organic compounds such as toluene and NO_x which are air pollutants.[25,21] The application we investigate in this work is the decomposition or oxidation of methane into

hydrogen gas and CO_x species. This process is being investigated for the goal of capturing the hydrogen for efficient syngas production[112] and also for the goal of removal of methane from the environment prior to release into the atmosphere where it acts as a very strong greenhouse gas.[113]

In the field of atmospheric pressure plasma interactions with catalyst materials, catalyst plasma synergistic effects are of great interest. One specific effect seen from plasma treatment of catalyst is the shift of the curve of targeted decomposition of material vs temperature to a lower temperature range.[111,114,115] Whitehead et al. (2010) takes this study one step further to show that the amount of temperature difference between the plasma and non-plasma treatment converted to the same amount of electrical energy would take far more energy than the plasma treatment requires.[111] For the 50% decomposition point they calculate that for the heating saved requiring 60 Watts of energy, the plasma source only consumes 1 Watt of energy. They also confirm from separate plasma and thermal catalysis treatments they only achieve ~20% decomposition whereas when the plasma is brought in contact with the catalyst the decomposition increases to ~65%. Another effect of the plasma catalysis is the changing of the selectivity of the reaction products. Pietruszka et al. (2004) demonstrated that increasing the input power of the plasma treatment during catalysis lead to an increase in the CO_2 vs CO selectivity for a methane decomposition reaction.[116] They attribute this to moving closer to the thermodynamic equilibrium for CO_2 production using plasma input energy which normally requires a much higher temperature than used for the plasma treatment.

While some effects of the plasma on catalysis are clear, there is a much more limited amount of research focused on the actual surface reactions that occur in order to cause these

synergistic effects. The possible synergistic effects at the surface of the catalysts are outlined by a review paper by Neyts et al. (2015).[117] The surface morphology[118] and dispersion of the catalyst material[119] on the support structure has been shown to change post plasma treatment which could help with the catalyst reaction by leading to more reactive sites. The plasma can also change the chemical state of the catalyst material such as the reduction of NiO to the more reactive Ni which has been shown to possibly occur[120,121] or simply changing the oxidative state of the metal. Additional surface processes can also be modified by plasma exposure such as the reduction of catalyst poisoning by deposition of unwanted surface species. Wang et al. (2013) has shown an increase in NH_3 conversion efficiency using a Fe catalyst from ~7 % for both plasma and catalysis alone to a 99% conversion efficiency due to the plasma prevention of surface bound nitrogen which destroyed catalyst reactive sites.[122] There are also potential catalyst effects on the plasma that may occur for some systems which can help synergistic effects though these effects are less likely to occur for our experimental system. We believe that our investigation into specific surface effects by observing the plasma directly interacting with the surface will further the understanding of what synergistic effects are occurring for our plasma catalysis system.

There are several approaches to conversion of methane over catalyst materials. The most commonly used one for hydrogen production currently is reacting methane with steam to produce CO, CO_2 and H_2 which is an endothermic process requiring 206 kJ/mol of energy and is shown in equation 3. Another reaction is the typical combustion reaction which methane reacts with 2 O_2 species to produce CO_2 and H_2O, however this reaction is highly exothermically releasing ~800 kJ/mol of energy and is shown in equation 2.

Methane can also be reacted with CO_2 to produce CO and H_2 but this approach requires a large energy input of 247.4 kJ/mol which is larger than steam reformation and is shown in equation 4. The approach that is most desirable for our work which can be done at lower temperatures is the partial oxidation of methane is which is mildly exothermic releasing 35.6 kJ/mol and is described in equation 1.[25]

$$CH_4 + 0.5O_2 \Rightarrow CO + 2H_2 \quad (1)$$

$$CH_4 + 2O_2 \Rightarrow CO_2 + 2H_2O \quad (2)$$

$$CH_4 + H_2O \Rightarrow 2CO + 3H_2 \quad (3)$$

$$CH_4 + CO_2 \Rightarrow 2CO + 2H_2 \quad (4)$$

$$CO + H_2O \Rightarrow CO_2 + H_2 \quad (5)$$

It should be noted as well that any CO produced can undergo several reactions as well with oxygen and water vapor to form CO_2. The first is simply a reaction with oxygen which only produced CO_2 and the other reaction is shown in equation 5 which produces both CO_2 and H_2. This means that CO is one of the more difficult species to produce generally as it can react to form the other products of the partial oxidation reaction as well. However, the above reactions generally do not take into account a plasma environment which is highly non-equilibrium and may provide energy to produce reactions not typically seen for methane conversion. Some of these species include atomic oxygen which is reactive enough to break the bonds between many other molecular species, CH_x species where the x is less than 4 which normally occur at a surface but can happen in the gas phase with a

plasma environment, and metastable species such as excited CO_2 which can absorb significant energy in vibrational states.

The goal of this work is to establish the methodology that allows for careful study of catalyst materials as they are exposed to plasma based reactive species and undergoing catalyst reactions. Using DRIFTs we can monitor any changes to the surface that are sensitive to IR absorption and observe these changes as they occur in real time. This setup is then connected to a gas cell which uses IR absorption to monitor several critical species involved in the reactants and the products of the methane partial oxidation reaction. While CO is expected to as a product from this reaction it is also possible to form CO_2 and H_2O depending on the available oxygen, catalyst surface states, and energetic particles produced from the plasma source. We are able to monitor how these species are produced relative to one another based on plasma and catalyst conditions and also monitor the reduction in methane amount which reveals the effectiveness of the methane conversion by this system. Enhancement of the catalyst reaction by plasma will be investigated through methane reduction and looking at the difference between how the plasma behaves alone compared to the plasma interacting with the catalyst material. The gas phase results are then compared to what changes occur on the catalyst surface which may help suggest possible enhancements mechanisms. For instance, carbon deposition on a catalyst surface which is strongly bonded and is not removed quickly by the catalytic reaction can lead to a loss of reactive sites on the catalyst material called catalyst poisoning. This can be monitored by the DRIFTs to see under what conditions this may occurs for the catalyst material and if it is possible for the plasma to remove any of these species to regenerate the catalyst. Additionally it is critical to understanding the behavior of these changes to the catalyst

surface in detail to be able to suggest further catalyst materials which may work well plasma enhancement in the future.

5.2 Experimental Procedures

5.2.1 Plasma source

The plasma source used in this work is a MHz driven design created by Bruggeman *et al*. and has been extensively characterized for plasma species produced, heating, and gas flow parameters.[38,32,39] The design uses a 1 mm diameter tungsten pin electrode mounted inside a quartz tube (1.5 mm inner diameter (ID) and 3 mm outer diameter (OD)) with a grounded copper ring electrode (5.3 mm length, 3 mm ID). The original design is based on the atmospheric pressure plasma jet proposed by Park and Selwyn.[87] The standard operating conditions of the MHz jet are a 14.4 MHz modulated driven frequency with a 20% on/off duty cycle (20% on time, 80% off time). Details of how the power was calculated for this source can be found in previous work.[40] The gas flow in this work has been reduced from the original standard flow of 1.5 lpm to 0.4 lpm Ar flow through the jet in order to increase the residence time of the reactant gasses in the proximity of the catalyst material. The plasma source cannot be lowered below this gas flow point because this will lead to greatly increased heating of the plasma source and ignition of the jet becomes difficult below approximately 0.4 lpm. Additionally, lowering the gas flow to lower values will lead to a larger discrepancy between previous work where this plasma source has been characterized.

5.2.2 Materials

The catalyst material used in this work is a nickel based catalyst supported on a combination of Al_2O_3 and SiO_2 and is in the form of a fine powder. The weight percentage of nickel is 65% and has a surface area of ~175 m^2/g. This catalyst was purchased from Sigma Aldrich. The methane used for this work has a purity of 99.99%. The catalyst is in the form of a powder with a particle size ranging from 100-500 μm. The catalyst specifically used was sifted through metal meshes of 150 μm and 250 μm to narrow the size distribution of the powder used. The exact morphology of each powder molecule is assumed to be spherical and unchanged by the plasma treatments but was not studied directly in this work. Due to the experimental setup involving a slanted gas flow from the plasma jet and the powder being very fine, the powder was pressed into a ball shaped pellets around a ceramic center approximately 6 mm in diameter which is the diameter of the inner reaction chamber of the DRIFTs reaction chamber. Tests were done to show the catalyst material is stable under the gas flow conditions of the plasma jet and that no catalyst materials were removed from the pellet. This material configuration was used for both gas phase and DRIFTs results for consistency.

5.2.3 Characterization and Experimental Setup

The characterization setup is based on the FTIR system called the IRTracer-100 made by Shimadzu with a mercury cadmium telluride (MCT) style liquid nitrogen cooled detector installed for all measurements taken with the system to increase signal to noise ratio. For the gas phase measurements taken with this system a custom built gas cell was used as shown in Figure 5.1 which is made from quartz and uses ZnSe windows for the IR beam. All gas phase measurements are done at 0.5 cm^{-1} resolution and with 3 scanned averaged together to allow for good time resolution investigating changes. The optimized

signal for the gas cell was approximately 150 E on the monitor setting of the Shimadzu FTIR software.

The surface characterization setup is a DRIFTs unit named the Praying Mantis made by Harrick Scientific which integrated with the IRTracer unit. In addition to the praying mantis DRIFTs unit, a high temperature reaction chamber (HVC-DRM-5) was used for temperature and environment control around the catalyst sample. The reaction chamber uses two KBr windows for IR light and has a 3rd viewport which was converted into ceramic piece integrating the plasma source into the reaction chamber dome as pictured in Figure 5.1. All measurements done with the DRIFTs cell use 4 cm^{-1} resolution and 20 scans averaged for each measurement. The optimized DRIFTs signal was approximately 10 E based on the monitor setting of the Shimadzu FTIR software.

The experimental setup for the plasma catalyst interaction was kept consistent between the gas phase and the DRIFTs experiments to ensure consistency. The distance of the viewport window where the APPJ is located to the middle of the DRIFT heated reactor is approximately 8 mm and at an angle of 40°. The distance of the plasma jet is changed by changing the ceramic feedthrough piece so that the distance from the tip of the nozzle to the catalyst is the only parameter changing with changing distance. The distance from the end of the plasma nozzle to the grounded electrode and the high voltage pin are kept the same for all experimental conditions as shown in Figure 5.1. The gas through the plasma jet is 0.4 lpm Ar with a 0.5% admixture of O_2 gas and there is another gas flow from the bottom of the high temperature reaction chamber which is 0.2 lpm Ar with 1% of total gas mixture CH_4. The gas is then mixed in the reaction chamber above the catalyst prior to entering the heated catalyst area. The entire high temperature reactor is water

cooled to keep the metal, windows, and plasma jet cooled so that no melting occurs during experiments.

The experimental procedure for all experiments involved a conditioning step of the plasma source prior to use with the catalyst to remove any contaminants which may have been deposited in the source. The gas lines used in the experiments are also pumped using vacuum systems at 1×10^{-5} torr pressure for removal of any atmospheric air prior to opening of the gas bottles to ensure purity. The catalyst pellet is then added to the reaction chamber and then the reaction chamber is flushed with the Ar and O_2 gas flows for 20 minute prior to experiment start to remove any residual air from the reaction chamber. The total volume of the reaction chamber is approximately 8.0 cm^3 and the total volume of the reaction chamber where the catalyst is present is 0.45 cm^3. Since all the gas must flow through the catalyst reaction area the gas residence time in this area is approximately 50 ms. There is some distance of gas line between the DRIFTs cell and the gas phase cell for measurement in the FTIR system to ensure that the gas has cooled to close to room temperature prior to entering the gas cell to reduce any heating effects on the measured spectrum. In particular, CO_2 and other FTIR spectrum are subject to broadening and other effects due to heating.

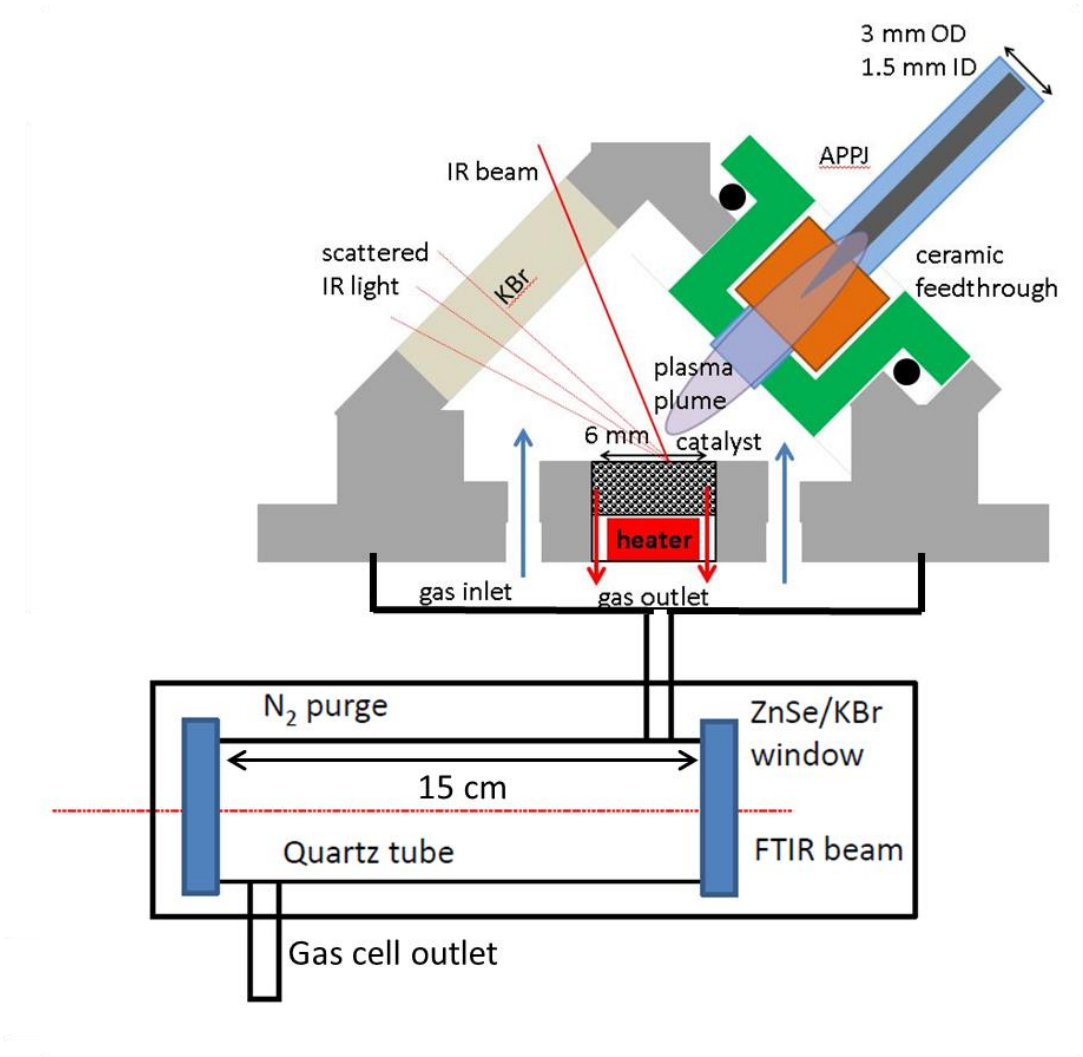

Figure 5.1: Overview of experimental setups of DRIFTs surface measurements where the plasma treatment of the catalyst occurs and gas phase measurements which are conducted post downstream from the DRIFTs setup.

5.3 Experimental Results and Discussion

5.3.1 Gas Phase Results

The first set of experimental results that were collected focus on looking at the gas phase information to determine the effectiveness of the methane reduction by plasma catalysis and investigate what species are produced by this catalytic reaction. Specifically we look at the amount of methane which is reduced by exposing it to the catalyst material, the plasma, or both combined together to see if a synergistic effect occurs by plasma catalyst treatment. The products of this reaction are then examined as well to determine the selectivity of certain species over others, specifically at CO, CO_2, and H_2O which are able to be carefully examined using FTIR.

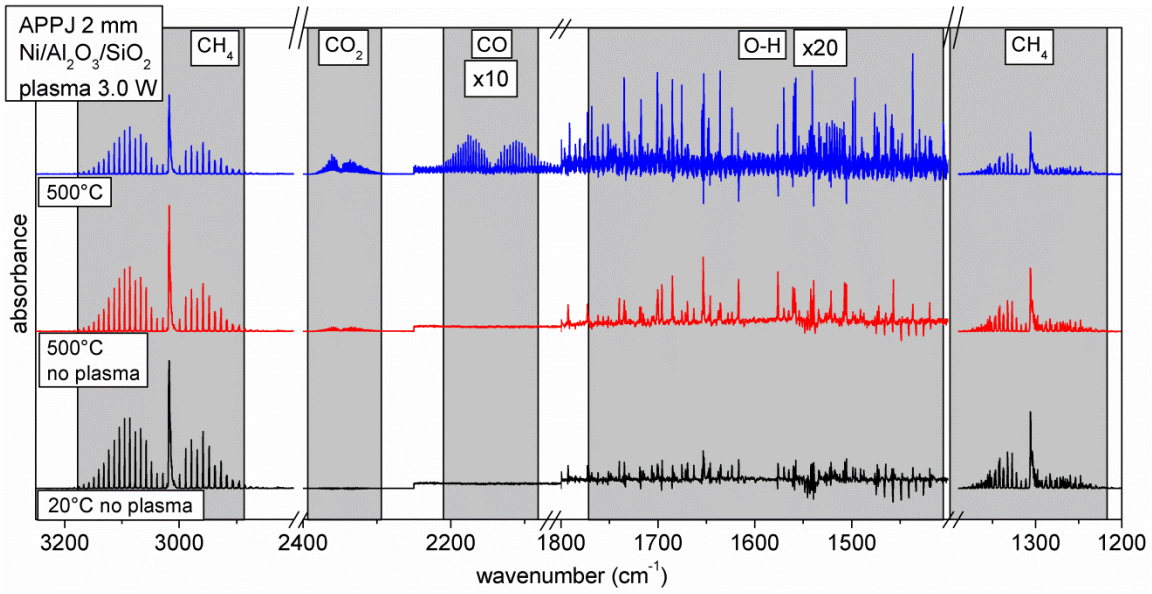

Figure 5.2: Full spectrum gas phase FTIR for 20 °C no plasma, 500 °C no plasma, and 2 mm plasma 3 W case at 500 °C taken with 0.5 cm^{-1} wavenumber resolution showing the primary complete spectrum which highlights the two CH_4 peaks and the CO_2 spectrum, the CO spectrum (x10), and the O-H spectrum (x20).

Figure 5.2 shows the FTIR gas phase results from the 15 cm length gas measurement cell connected to the output from the DRIFTs high temperature reactor setup with the integrated plasma source for the 8 mm plasma treatment distance case. This data shown is for 3 W at 500 °C catalyst temperature compared with no plasma at room temperature. This overview shows the specific regions we will use to calculate the density of each of the product species from the catalysis reaction. In order to quantify these peaks Beer's law of absorbance was applied to the spectrum to convert FTIR absorbance into species density for each of these 4 species observed in Figure 5.2. The conversion from absorbance to density based is given by the equation 1.

$$n = \frac{Abs}{0.4343 * \sigma * l} \quad (1)$$

In this equation n is the density of the species being calculated, Abs is the absorbance measured by the FTIR, l is the path length of the gas cell which for this system is 15 cm, and σ is the cross section of each individual peak. In order to this the cross section was taken from the HITRAN FTIR data base.[123] Additionally the correction factor is also taken from the published work on the interpretation of this data base.

5.3.1.1 CH_4

The first species which is critical for the discussion the catalyst reaction is methane. The dominant peaks shown here are from the methane gas which is added at ~1% concentration to the Ar/O_2 gas flow through the cell and shown in the spectrum as two different peak spectrums; one from 3160 to 2900 cm^{-1} which has numerous smaller peaks to either side of a large central peak and corresponds to the stretching of the C-H bonds in the methane and one from 1370 to 1240 cm^{-1} which has a similar structure

though is smaller in absorbance and corresponds to the bending of the C-H bonds in the methane.[124] A highlight of the higher wavenumber spectrum is shown in Figure 5.3 which is used for the calculation of the CH_4 density. It is immediately clear that while the methane spectrum absorbance is reduced, we are not converting all of the methane present by this method and therefore careful quantitative analysis is needed to measure the change in the amount of methane. We can visibly see the production of several new peaks which correspond to species which are produced by the partial oxidation reaction of methane.

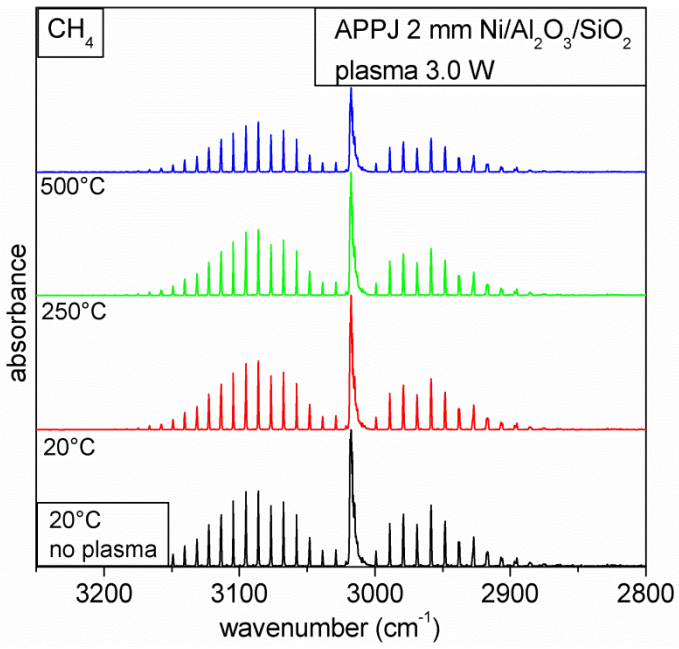

Figure 5.3: Methane spectrum for 3 W case, 20, 250, and 500 °C showing the individual peaks and demonstrating how methane density is calculated.

For the calculation of the methane density 11 different individual peaks from the peaks shown in Figure 5.3 were used to calculate density individually using cross

sections for those specific peaks and then these densities were then averaged. For the methane spectrum densities we were able to then calibrate this calculation using mass flow controllers to precisely flow set amounts of methane into the FTIR gas cell and measure the absorbance given for each concentration of methane. This absorbance was then converted to density and the relationship between the real density and the measured density was found to be linear with an offset factor of ~2. This correction factor was then applied to all data collected with the methane spectrum to give a more accurate measure of the amount of methane present.

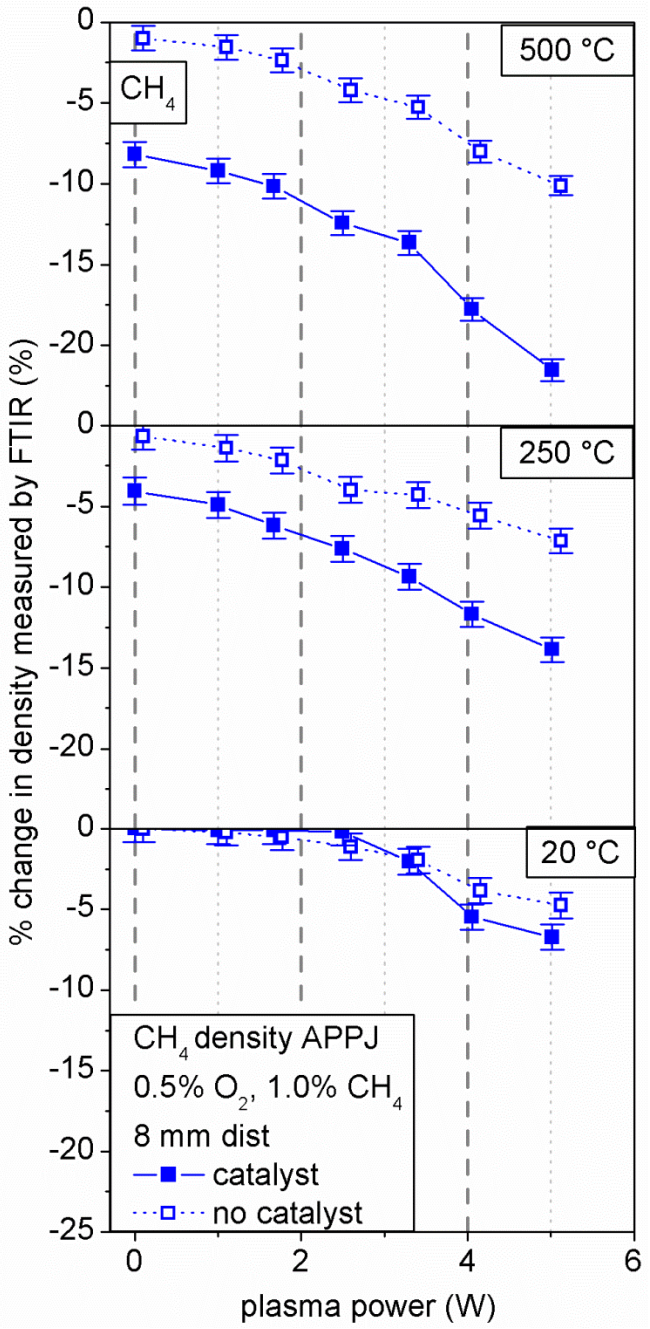

Figure 5.4: Percentage reduction compared to initial methane density for 500, 250, 20 °C temperatures at 8 mm distances with catalyst and plasma only conditions.

.

The amount of methane reduced from the starting methane level in percentage is shown in figure 5.4 for 8 mm distances, catalyst vs no catalyst, 20-500 °C, and a range of plasma powers. In general we see more methane reduction with increasing plasma power. This reduction amount is reduced when there is no catalyst present so the only conversion is occurring by plasma interacting with the gas. Additionally the amount of methane converted increases with temperature, particularly for the case where the catalyst is present.

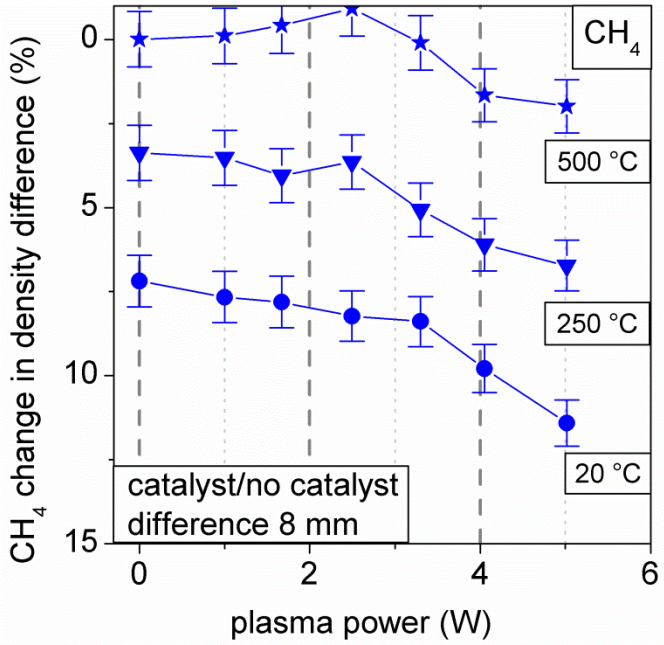

Figure 5.5: Difference between catalyst and no catalyst for percentage reduction compared to initial methane density for 500, 250, 20 °C temperatures at 8 mm distances.

The difference between the methane reduced for the plasma only case and the plasma with catalyst case is critical for understanding if there is a synergistic reaction occurring for the plasma catalyst system and is shown in Figure 5.5. We can see that the

difference between these systems increases significantly with increasing temperature. This is due to the catalyst becoming more active with temperature and playing a more important role. However, at all temperatures we see an increase in the difference between the catalyst and no catalyst cases with increasing plasma power which indicates that the plasma power is playing an important role here. It is important to note that we get a notable difference with increasing plasma power at room temperature as well which indicates that we starting to activate the catalyst material at this condition even though no thermal catalysis occurs here.

5.3.1.2 CO

The first of the species is CO which is shown as a spectrum of peaks from 2220 to 2060 cm^{-1} in the form of two separate humps.[123] The presence of this peak only occurs due to plasma treatment at sufficiently high power treatments.

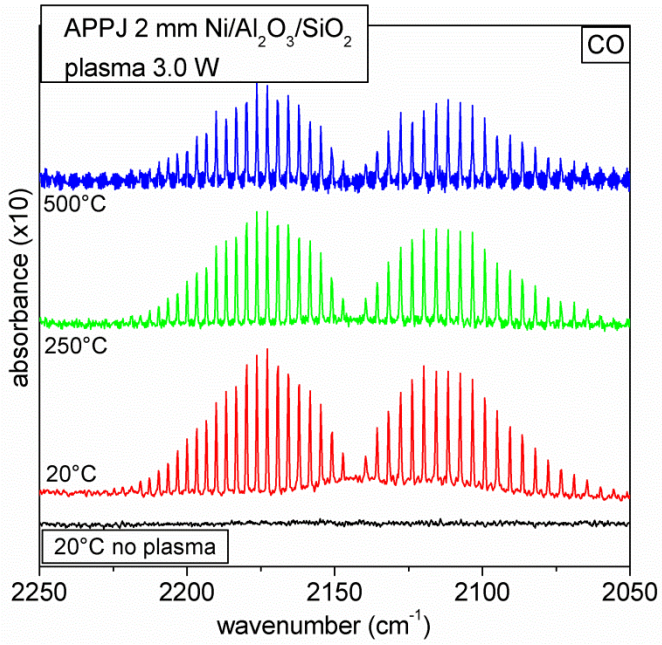

Figure 5.6: CO spectrum for 3 W case, 20, 250, and 500 °C showing the individual peaks and demonstrating how CO density is calculated.

The calculation for the density of the CO was done by using the cross section for 20 individual peaks, 10 from the center of each of the two hump shapes which correspond to the strongest signals from the CO in the gas phase. Each of these individual peaks is highlighted in the spectrum shown in Figure 5.6. The density was then calculated form the average of these peaks.

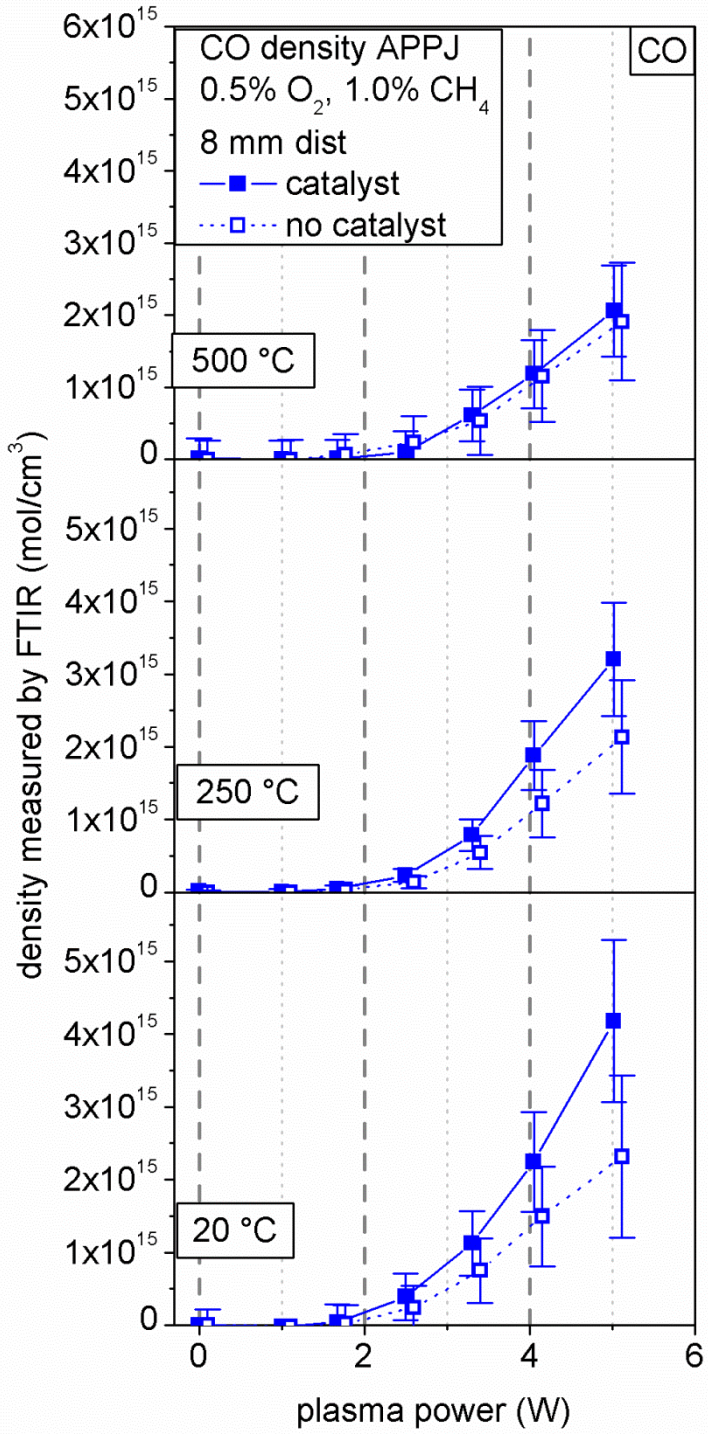

Figure 5.6: Carbon monoxide density for 500, 250, 20 °C temperatures at 8 mm distances with catalyst and plasma only conditions.

.

The results of this density calculation are shown in Figure 5.7 for the same conditions and Figure 5.4. From this data we can see that the density of CO decreases with increasing temperature. In addition, at the highest temperature the difference between the catalyst and no catalyst cases almost completely disappears suggesting that for this case most of the CO produced is coming from the plasma conversion of methane. It is also important to note that there is essentially zero CO production below 2.5 W plasma power for any conditions suggesting that a certain level of plasma energy is required for this reaction pathway to occur.

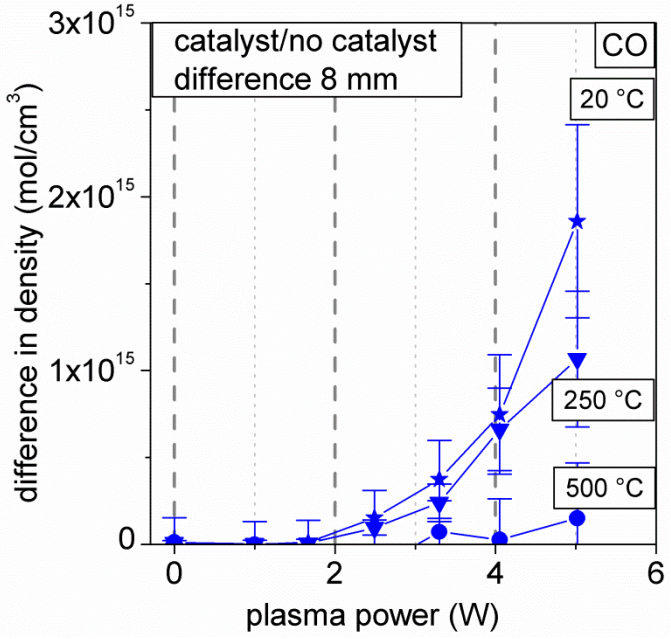

Figure 5.8: Difference between catalyst and no catalyst for CO density for 500, 250, 20 °C temperatures at 8 mm distances.

For the difference plot between the catalyst and no catalyst cases we can see that this shows the opposite trend from the methane, as shown in Figure 5.8. As temperature

increases there is significantly less difference between these cases down to almost no difference at 500 °C. This suggests that the plasma is stimulating the catalyst to produce CO species at a lower temperature but at higher temperatures all the CO species seen are from the plasma conversion only. It is possible as well that the CO species which are produced at lower temperatures undergo further reactions at higher temperatures converting the CO to CO_2 by reaction with oxygen or water vapor. The water shift reaction, shown in equation 5, requires 2.85 kJ/mol energy which is easily supplied by the process at higher temperatures. This would lead to a decrease in CO and H_2O at higher temperatures while seeing an increase in CO_2.

5.3.1.3 CO_2

Another peak that clearly forms from this catalysis reaction is CO_2 which is differentiated from atmospheric CO_2 by having a nitrogen purge around the gas cell to try and reduce the influence of the atmospheric CO_2 from our measurement as much as possible. The CO_2 is shown as a spectrum of peaks from 2380 to 2300 cm^{-1} and is also shown generally as two distinct humps within this spectrum similar to the CO spectrum.[123] We see from this data that generally the CO_2 spectrum increases as temperature increases.

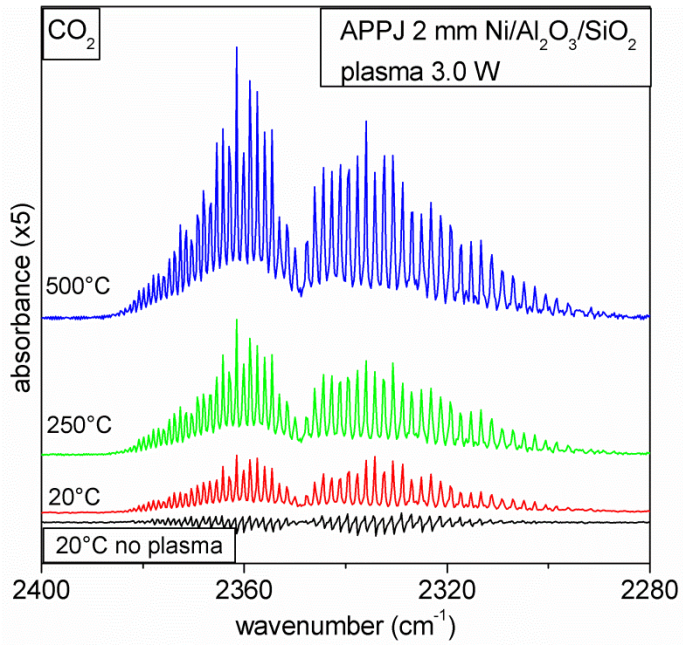

Figure 5.9: CO_2 spectrum for 3 W case, 20, 250, and 500 °C showing the individual peaks and demonstrating how CO_2 density is calculated.

The carbon dioxide calculation was done using 40 peaks from the CO_2 spectrum, 20 from each of the two distinct humps and similar to how CO was calculated. The peaks that were used for this calculation are shown in detail in Figure 5.9. For this calculation it was assumed that we were able to remove most of the CO_2 from the ambient air around the measurement cell through an N_2 purge though there may be some slight residual CO_2 signal. The signal was checked by monitoring the CO_2 peak area while flowing the N_2 gas until the CO_2 was no longer reduced and then the background was taken for these measurements.

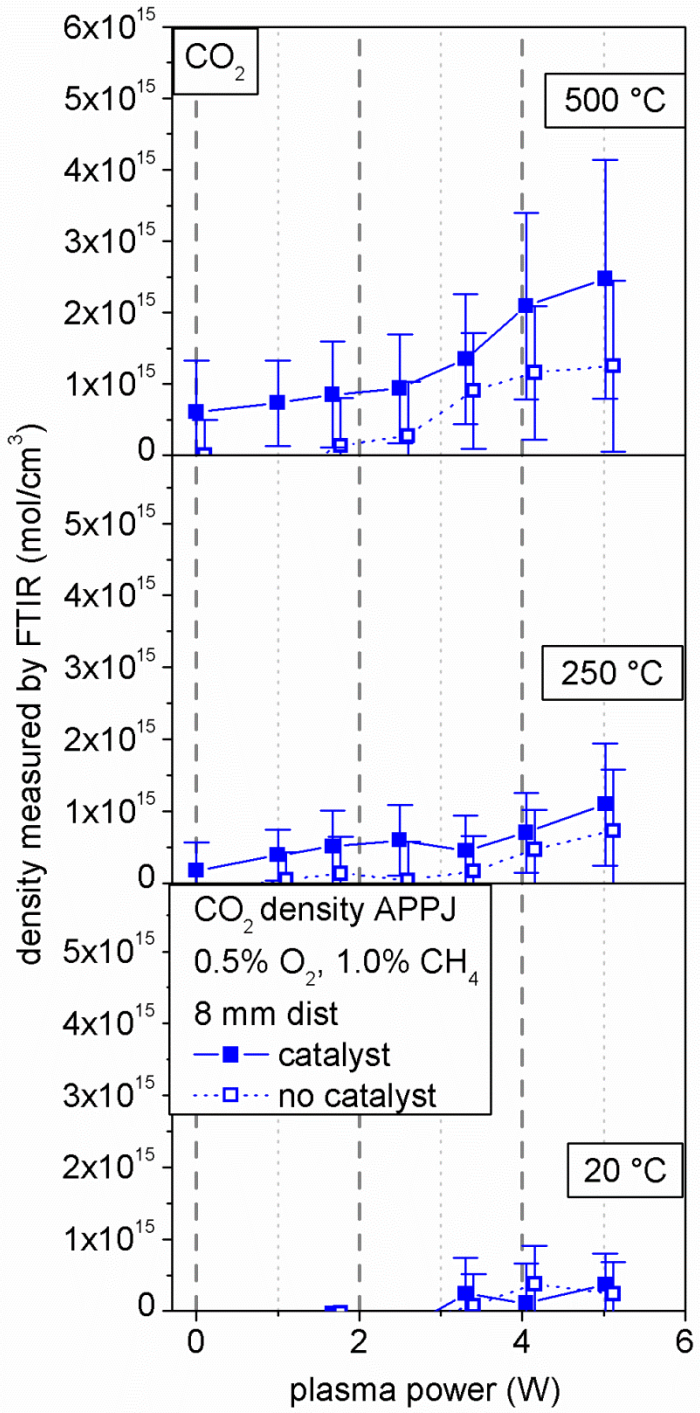

Figure 5.10: Carbon dioxide density for 500, 250, 20 °C temperatures at 8 mm distances with catalyst and plasma only conditions.

The density calculation results for CO_2 are shown in Figure 5.10 and cover the same treatment conditions as Figure 5.4. For CO_2 we see primarily the opposite trend of the CO behavior, which is that the amount of CO_2 drastically increases with catalyst temperature and that plasma power plays very little role in the CO_2 production. The only conditions we get any measureable CO_2 produced with the plasma only case is at 500 °C with a plasma power of above 4 W and even here it is fairly small when compared with the catalyst case.

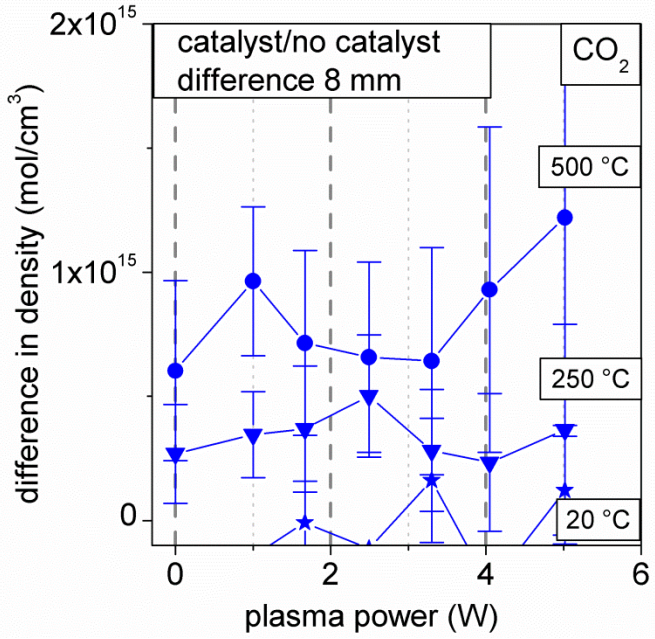

Figure 5.11: Difference between catalyst and no catalyst for CO_2 density for 500, 250, 20 °C temperatures at 8 mm distances.

The difference plot, shown in Figure 5.11, between the catalyst and no catalyst cases shows a slight increase with plasma power overall but generally seems dependent more on the temperature of the catalyst. With increasing catalyst temperature we see an increased CO_2 production when the plasma is used in conjunction with the catalyst. It

seems that the catalyst does not produce CO_2 at low temperature but once it is active at high temperature it is able to efficiently use plasma produced species to convert methane into CO_2.

5.3.1.4 H_2O

The final peaks that we clearly see in the gas phase are from H_2O in the gas phase. Again, due to the presence of atmospheric H_2O, a nitrogen purge was used to try and reduce any influence from the local environmental air as much as possible and was checked by taking spectrum prior to experiment start to ensure H_2O spectrum stability. This spectrum is represented in two different regions and is shown as numerous small individual peaks throughout these two regions without the characteristic continuous shape of the other species. The first of these spectrums ranges from 1800 to 1400 cm^{-1} with a small gas at the center around the 1600 cm^{-1} region and corresponds to the bending of the O-H bonds. The second spectrum is in the region from 3950 to 3550 cm^{-1} and corresponds to the stretching of the O-H bonds.

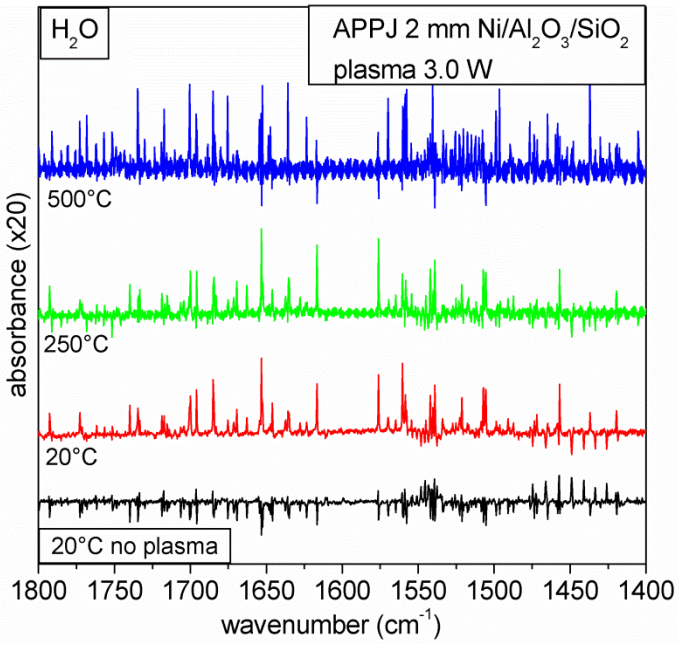

Figure 5.12: H_2O spectrum for 3 W case, 20, 250, and 500 °C showing the individual peaks and demonstrating how H_2O density is calculated.

The H_2O density calculation was the most difficult to perform in an accurate manner due to the non-structured nature of the H_2O peaks in the FTIR range, unlike CO_2 and CO. For this calculation in order to be sure the correct peaks were selected only the most distinct 11 peaks were selected for density calculation. And even for these 11 peaks the combination of intensity and cross section is fairly small compared to the other species measured. As seen in Figure 5.12 all the peaks aside from the few with the highest intensity are subject to a significant amount of noise and therefore difficult to use in a consistent density calculation. In conjunction with the fact that there is was vapor present in the atmosphere and on the wall of the measurement setup it was difficult to get an accurate measurement of H_2O and therefore the error associated with these density

measurements is fairly high. However, there are still some trends which stand out from the data collected.

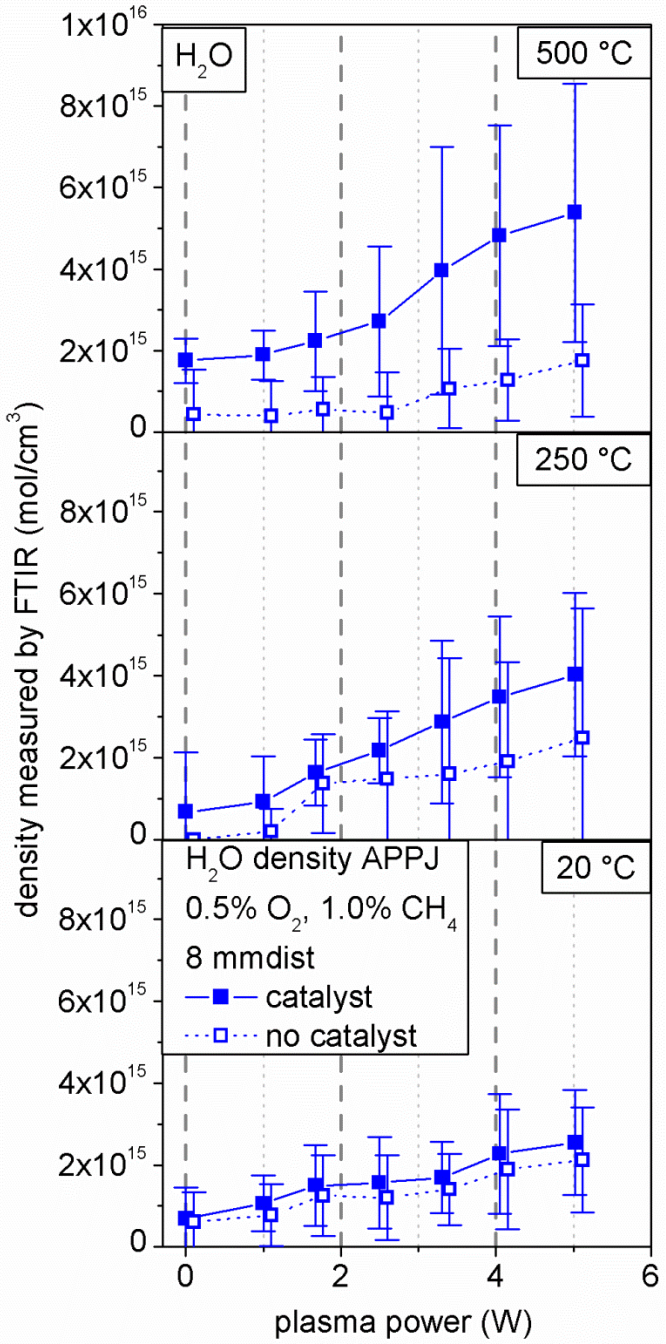

Figure 5.13: Water density for 500, 250, 20 °C temperatures at 8 mm distances with catalyst and plasma only conditions.

The full density measurements are shown for H_2O in Figure 5.13 for the same experimental conditions as shown in Figure 5.4. In general the water density shows an increase with both increasing temperature and increasing plasma power. At 20 °C there is very little difference between the cases with and without catalyst present suggesting that here most of the H_2O production is from the plasma conversion. However, the amount of H_2O produced without catalyst present stays fairly constant over the range of temperatures so it is clear the catalyst starts to play an important role here with increasing temperature.

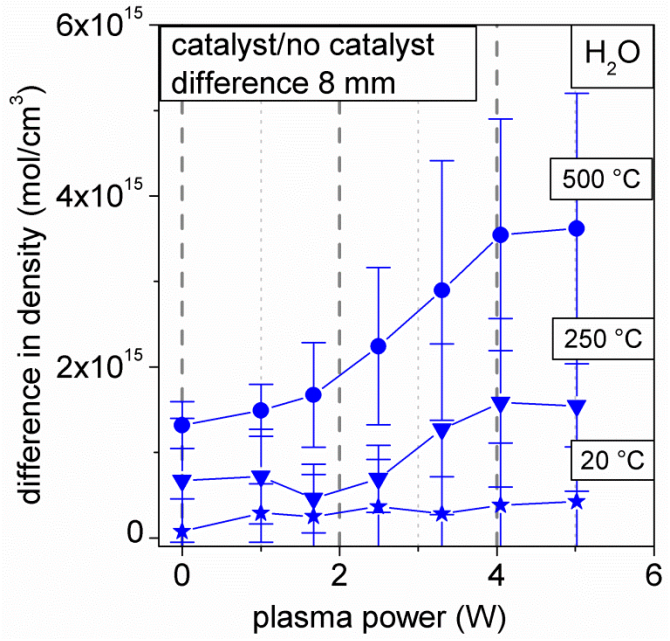

Figure 5.14: Difference between catalyst and no catalyst for H_2O density for 500, 250, 20 °C temperatures at 8 mm distances.

The difference plot shown in Figure 5.14 between catalyst and no catalyst cases looks initially to be very similar to the CO_2 species. However, we can clearly see that the difference scales significantly more with increasing plasma power as well for this

species, especially at higher temperature. It seems that the plasma alone is able to produce H_2O species but that the catalyst significantly increases this amount as it becomes active at higher temperatures. Indeed, once the catalyst is active it seems that the synergistic effect becomes quite clear for H_2O production.

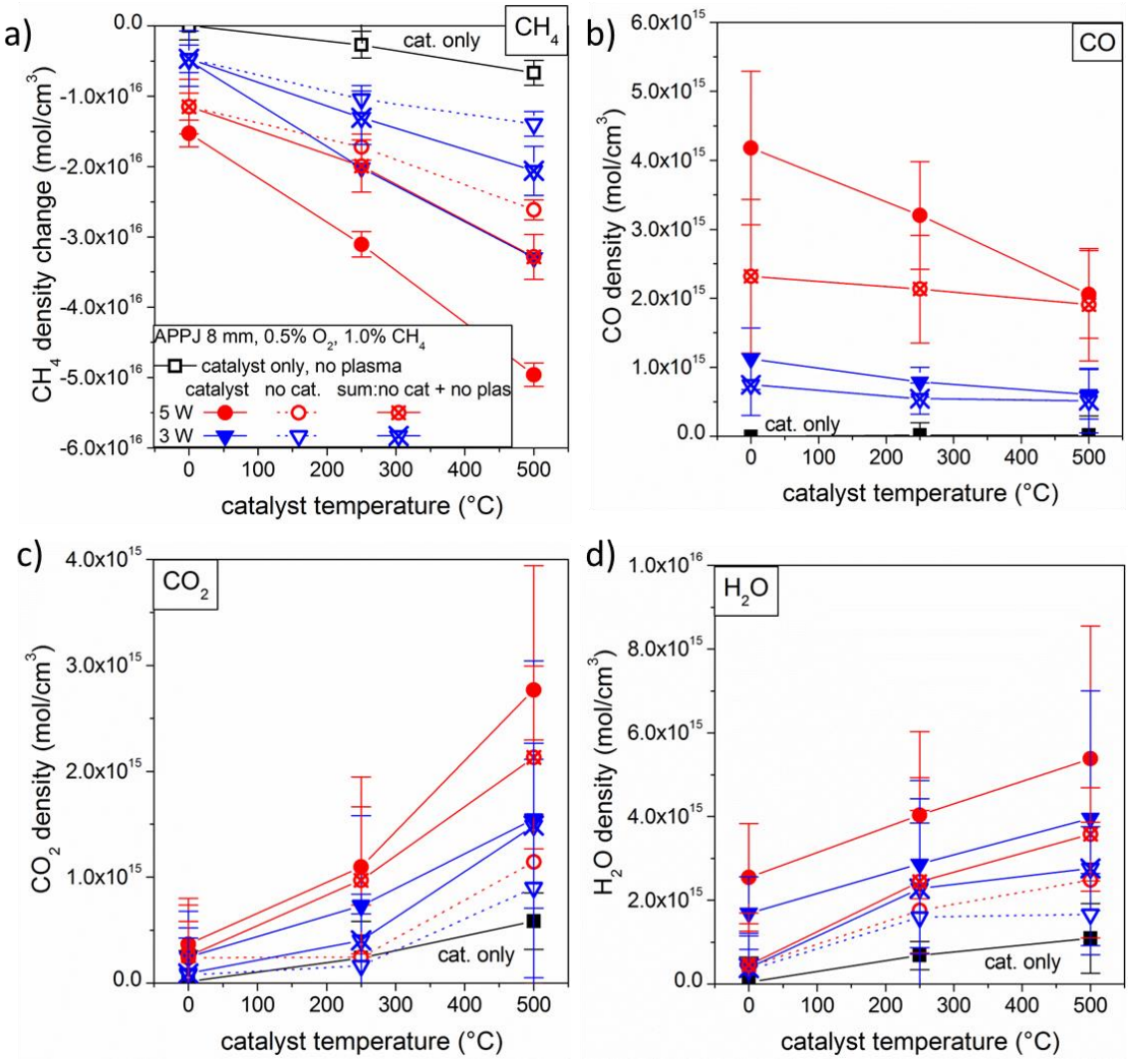

Figure 5.15: Comparison of various densities for two plasma powers for plasma catalyst, plasma no catalyst, catalyst alone, and the sum of catalyst only and plasma only for comparison to the plasma catalyst experimental data over a range of temperatures for a) CH_4, b) CO, c) CO_2, and d) H_2O.

A summary of all of these plasma conditions plotted vs catalyst temperature and compared to experiments with heating the catalyst only are shown in Figure 5.15 where CH_4, CO, CO_2, and H_2O are shown in Figure 5.15 a), b), c), and d) respectively. For methane reduction we can see from Figure 5.15 a) that the catalyst alone is the least effective conversion at all temperatures, followed by the plasma alone, and then with both catalyst and plasma combined giving the largest reduction. Indeed, the catalyst only and the plasma only added together are shown to be less than the plasma catalyst case for both plasma powers and at all temperatures. We see that the actual methane reduction is a factor of 1.51 larger at 500 °C and 1.33 larger for 20 °C for the plasma catalyst system compared to the sum of the catalyst and plasma only effects, suggesting some synergy between the catalyst and the plasma. There also appears to be a clear difference in the slope of the methane reduction with respect to temperature.

The CO density shown in Figure 5.15 b) shows again a reduction in CO density with increasing temperature, opposite the trend of the CO_2 and H_2O species. However, the dominant CO production seems to occur based on higher plasma power. We see that the plasma alone case for the 5 W case is higher than the plasma and catalyst case for 3 W power dissipation. For catalyst alone without plasma present there is clearly no CO produced at any temperature at or below 500 °C. Therefore, without the plasma it seems that all of the catalyst behavior in this temperature range facilitates the production of CO_2 and H_2O over CO. The sum of the catalyst only and plasma only cases is directly overlapping with the plasma only case and clearly demonstrates the increased CO production behavior of the plasma catalyst system above the sum of each parts alone. For 20 °C we see a 1.81 factor increase of the CO production with the plasma catalyst system

over the sum of the plasma and catalyst effects along, though this falls off to a 1.07 at 500 °C which suggesting almost no synergistic production at higher temperatures.

Figure 5.15 c) shows in detail the CO_2 peak signal seen for all experimental cases. Here we see the very sharply increasing behavior with increasing temperature for the CO_2 peak. This occurs regardless of plasma conditions, though it is enhanced by having the plasma active as well. The catalyst alone and the plasma alone cases here produce similar amounts of CO_2 across the plasma power and distance conditions shown here. The sum of the catalyst only and plasma only cases for CO_2 production is only very slightly lower than the experimental plasma catalyst case. The amount of synergy of CO_2 production shows a 1.42 factor increase at 20 °C, a 1.13 increase at 250 °C, and a 1.30 factor increase at 500 °C.

Figure 5.15 d) shows the H_2O peak behavior which also scales with temperature but still shows activity from the plasma treatment as well. This is clear from the nearly zero water vapor produced by the catalyst alone at room temperature but the significant increase in H_2O signal with the addition of the plasma treatment at this temperature. There is still a clear enhancement of H_2O species produced as well for the plasma catalyst experimental case over the sum of the catalyst alone and plasma alone cases. Generally, it seems that these enhancements over the sums occur more significantly at lower temperatures. The factor of this enhancement is approximately 1.5-1.7 over the temperatures investigated here. This seems to be due to the face that at these temperatures the catalyst would have no affect alone, but the plasma produced species may be helping to activate the catalyst significantly here.

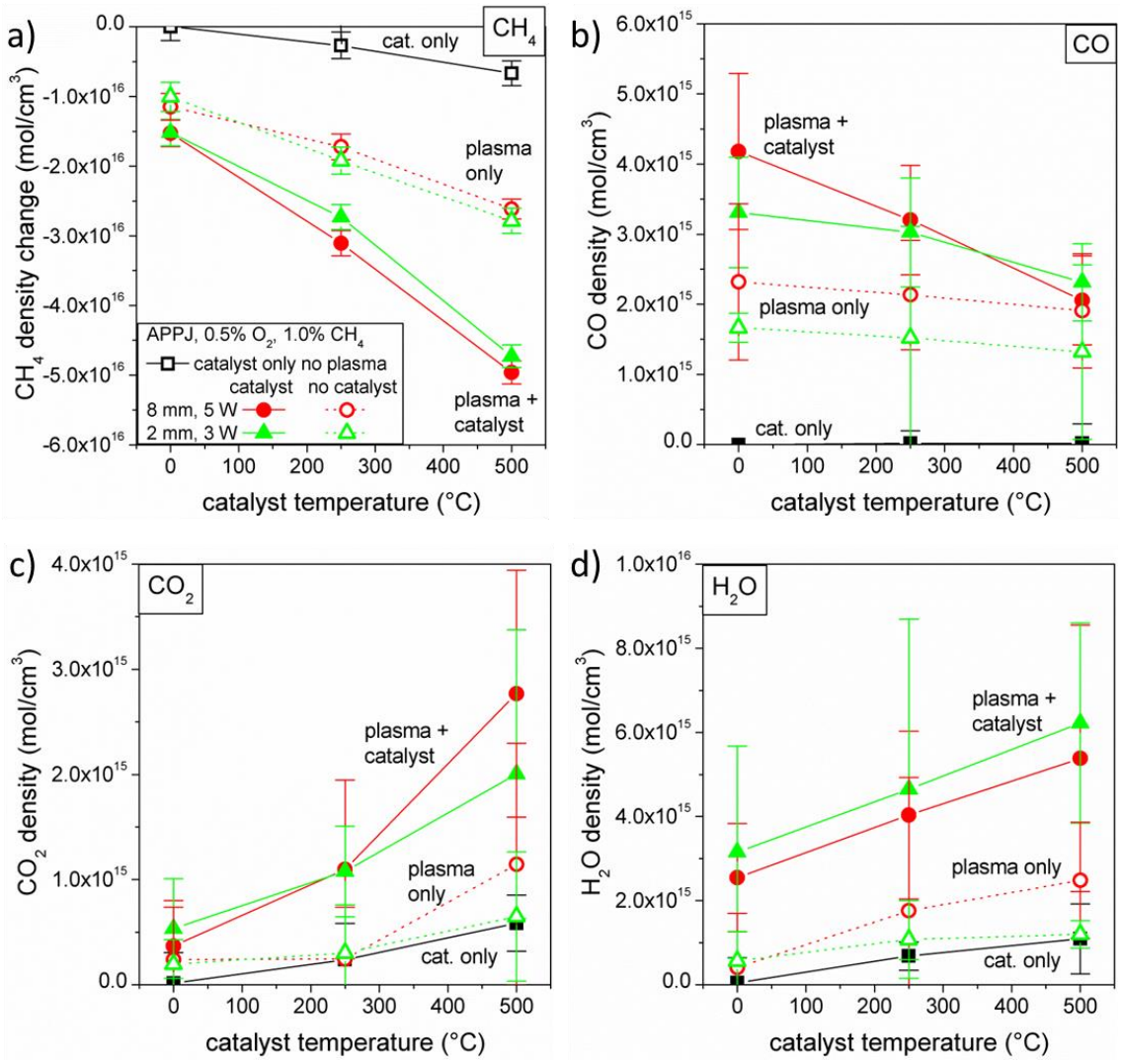

Figure 5.16: Comparison of various densities for two plasma distances for catalyst and no catalyst, and catalyst alone over a range of temperatures for a) CH_4, b) CO, c) CO_2, and d) H_2O.

Figure 5.16 highlights the difference between the 2 mm 3 W plasma case and the 8 mm 5 W plasma cases. For these conditions, the distance between the catalyst and the tip of the plasma plume is nearly identical, just barely above the top of the catalyst

material. Under these conditions, we see in general that the methane conversion results and products produced are very similar. The main difference is a very slight reduction in the amount of methane conversion and products produced for the 2 mm 3 W case compared with the 8 mm 5 W case. However, this is not completely consistent for the H_2O spectrum, and overall these results are very similar for the same plasma plume to catalyst distance regardless of plasma power.

5.3.2 Surface Measurement Results

The surface measurements were preformed using the same plasma setup and same experimental conditions with the DRIFTs cell integrated into the FTIR system so the IR beam can be used to monitor the surface. Therefore, these measurements could not be done simultaneously to the gas phase measurements. However, these measurements are done *in situ* with a time resolution of approximately one minute and therefore we can monitor changes to the surface as they occur. Figure 5.17 shows an example DRIFTs spectrum taken *in situ* showing the surface prior to heating, after heating to 500 °C, during plasma treatment at this temperature, and then after plasma treatment has stopped and the reaction chamber has been flushed with nitrogen gas to remove all gas phase species. This experiment is critical to characterize what changes are seen are due to IR light absorbed on the surface as the light is scattered and absorption of the IR light as it travels through the environment of the high temperature dome. The peaks that are in the negative direction of absorbance indicate that there is a loss of the species that was previously causing the IR light to be absorbed in that wavelength range. We can see from this experiment that the CO_2 peak and the two narrow CH_4 peaks are from IR light absorbed in the gas phase. However there are several other interesting permanent

changes to the catalyst surface that occur and are stable after the plasma treatment has stopped and the local gas removed from the catalyst.

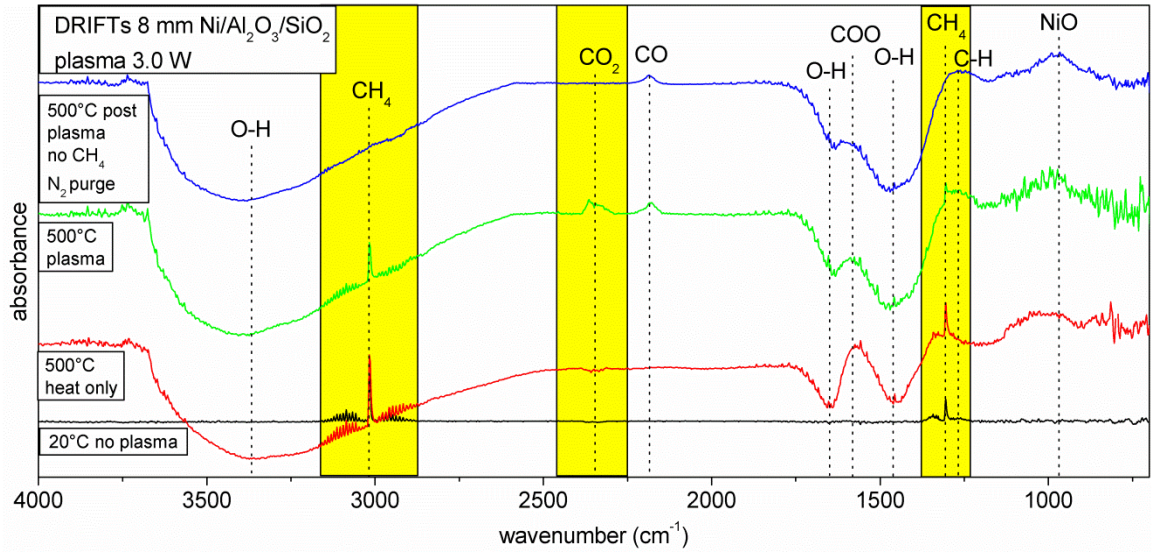

Figure 5.17: *In situ* DRIFTs at 8 mm distance with heating only to 500 °C, plasma treatment of 3 watts at 500 °C taken with 4 cm^{-1} wavenumber resolution with plasma on and then at 500 °C without plasma after purging the reaction chamber with nitrogen gas.

The CH_4 peaks seen here are from the gas phase and correspond to the same peaks seen from the previous spectrum in Figure 5.2 just with a much smaller magnitude due to the significantly smaller path length of the IR beam in the DRIFTs cell. The CO_2 as well is similar to the spectrum seen in the gas phase. It should be noted that the CO_2 seen here may be part of the reactions occurring since we know from the previous data that CO_2 production is maximized at increased temperatures and we see it strongest for the 500 °C plasma case. However, it is possible that this CO_2 is some residual atmospheric CO_2 as well since the DRIFTs beam does travel to the normal IR MCT

detector which cannot be 100% sealed from the ambient environment despite nitrogen flow to fill the DRIFTs unit surrounding the high temperature reaction cell. These are the transient peaks which disappear from the measurement after the nitrogen purge of the catalyst.

There are also several peaks which seem to be caused primarily by the increased temperature of the catalyst surface. The most pronounced of these is loss in intensity of the O-H peak regions at ~3400 cm^{-1}, 1650 cm^{-1}, and 1450 cm^{-1}. This loss is due to adsorbed water on the catalyst surface from exposure to the atmosphere prior to the experiment start being removed. These peaks appear very slightly from having dry gas flow over the catalyst sample for long periods of time such as Ar. They also appear significantly for both plasma treatment and heating of the catalyst sample. However, heating pretreatments to ~100 °C for long periods of time to remove the water from the surface could never fully remove water to plasma treatment. In other words, there is water adsorbed on the surface of our catalyst samples that stays on the surface to very high temperatures but is then removed but intensive plasma treatments. Indeed this has been seen in previous work involving catalysis, one such paper investigating using DRIFTs to investigate a Ni/TiO_2 catalyst saw only a 26% reduction in OH groups by heating to 423 K.[125]

The other peak that appears to show up due to heating only and be stable on the surface is a peak at ~995 cm^{-1} which is marked as number 3 peak in Figure 5.17 and is very broad in nature so it is difficult to get a fixture on the exact center of the peak. There are several possible explanations for this peak. The most likely explanation is NiO formation as the Ni is oxidized by the oxygen from the environment and from the catalyst

support materials SiO_2 and Al_2O_3. NiO studied in the form of nanoparticles has shown a significant and fairly broad peak form around 1040 cm^{-1} which could be this peak just shifted due to the nature of the particles in question.[126] This same peak was seen in previous work on Ni catalysis and described as a broad peak from 930-960 cm^{-1} but was left unassigned as the authors were unsure of the exact species responsible.[125] More evidence for the NiO is that the peak forms around 300 °C-400 °C which is approximately the temperature at which Ni will oxidize with some oxygen present in the ambient air.[127] The other possibilities for this peak assignment seems to be a low end of the alkoxy C-O bonding which is typically from 1050-1150 cm^{-1} which is what would appear from a partially oxidized methane molecule where one H is abstracted. Another possibility is sp^2 C=C bonding such as an alkene molecule which shows absorption in the range of 985-1000 cm^{-1}.[128]

Plasma treatment alone appears to cause the appearance of a CO peak which is bound to the surface of the catalyst material. Specific details of the behavior of this peak will be discussed in the remaining figures. The peak position is primarily at 2190 cm^{-1} though there is some shift apparent depending on the conditions of the plasma treatment and catalyst temperature. We can see that the CO shown here is stable due to it still being present following the end of plasma treatment and then flushing the gas away with nitrogen. Additionally, this peak is broader and has significantly more absorption than the CH_4 and CO_2 peaks as compared to the gas phase data.

The final peaks that displays an interesting behavior is the peak at 1590 cm^{-1} which is marked on figure 5.17 by the number 1. This peak is located in between the two O-H peaks which show significant reduction from heating and plasma treatment.

However, this peak is stable from heating alone, but then shows an increase at weaker plasma treatments and a decrease at more significant plasma power treatments. While this region is difficult to determine exactly what peak this is, it seems that one likely possibility is a C-O-O based species. Based on the literature COO^- or carboxylate groups can form in conjunction with metal ions and one of the strong peaks that is characteristic of COO^- in the IR range is at 1586 cm^{-1}.[129] Indeed, other work that investigates plasma catalyst interactions through DRIFTs have seen this same peak appear based on their work and assigned it to a carboxylate group, though they use a different catalyst material and they look at a different gas species for decomposition.[130,131,132] However, as there is still some uncertainty here, this peak will be referred to by its wavenumber for the rest of this work.

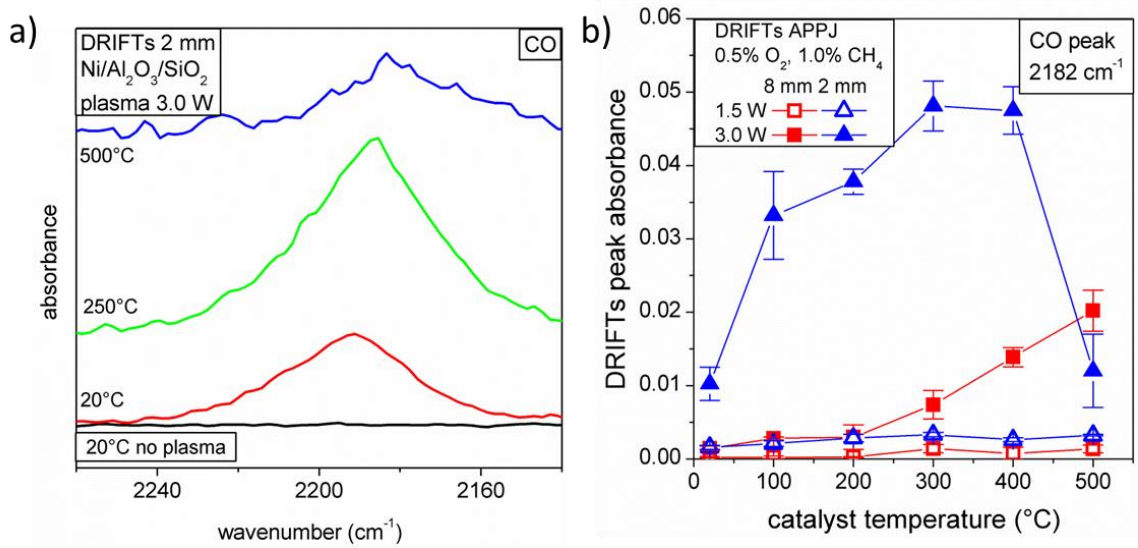

Figure 5.18: a) CO spectrum for no plasma, 2 mm 3 W case, 20, 250, and 500 °C showing the peak evolution b) extracted data from *In situ* DRIFTs of CO peak over 2 to 8 mm and 1.5 to 3.0 W plasma conditions.

Figure 5.18 a) shows the raw spectrum of the CO peak for 2 mm 3 W plasma conditions over various temperatures. The behavior of four of these critical peaks which have been shown to be surface changes on the catalyst are described in more detail starting in Figure 5.18 b) for various plasma conditions. The first of these and probably the most interesting is the CO peak at 2190 cm^{-1} and the behavior for this peak is shown in Figure 5.18. For this peak we see that at the weaker plasma treatment conditions of 1.5 W we see no surface CO formed at all. This corresponds to the gas phase data as well where we see no CO formed for any temperature or conditions if the plasma power is below 2.5 W as well. For a plasma power of 3 W and 8 mm distance we see that a CO peak appears on the surface once we reach a certain temperature of above 200 °C and then the absorbance peak increases with increasing temperature. However, at the 3 W and 2 mm plasma case we see an immediate CO production on the surface at the lowest temperature, the CO peak then initially increases with temperature before then plummeting and being almost completely removed at the highest temperature measured here of 500 °C. This result was confirmed several times by testing the removal of CO by going to higher temperatures and plasma powers after it has been formed. However, removal of the CO was not possible by increasing temperature alone even up to 700 °C; only when there is a plasma condition treating the catalyst surface do we see removal of CO at this high energy case.

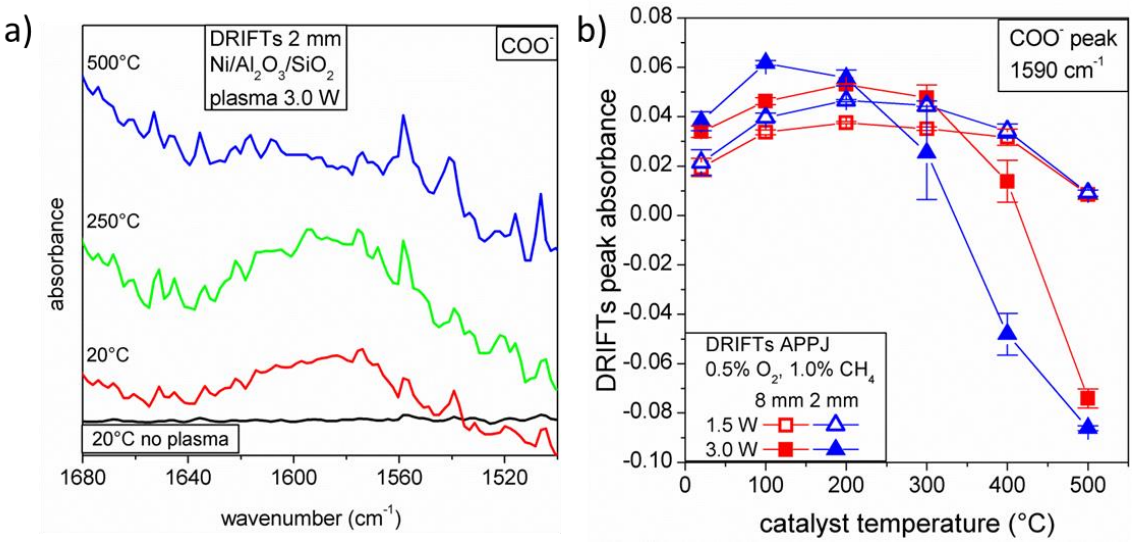

Figure 5.19: a) COO^- spectrum for no plasma, 2 mm 3 W case, 20, 250, and 500 °C showing the peak evolution b) extracted data from *In situ* DRIFTs of COO^- peak over 2 to 8 mm and 1.5 to 3.0 W plasma conditions.

The other peak that behaves in a similar manner is the COO^- peak at 1590 cm^{-1} and the raw spectrum of this peak for 2 mm 3 W plasma conditions over various temperatures is shown in Figure 5.19 a). The extracted data over all distances and powers is shown in Figure 5.19 b). This peak initially shows a slight increase with all plasma treatments at lower temperatures and then above a certain temperature the peak absorbance for this peak drops significantly, particularly for the stronger plasma treatment. The shift from increasing to decreasing seems to occur at about 200-300 °C for the 1.5 W plasma power cases and the 8 mm 3 W plasma case but the shift occurs a lower temperature for the 2 mm 3 W plasma power case. This is likely due to the increased plasma energy and reactive species reaching the surface for this case. Again it seems like

the plasma initially causes this species to be formed on the surface before reaching a sufficient energy to then remove it.

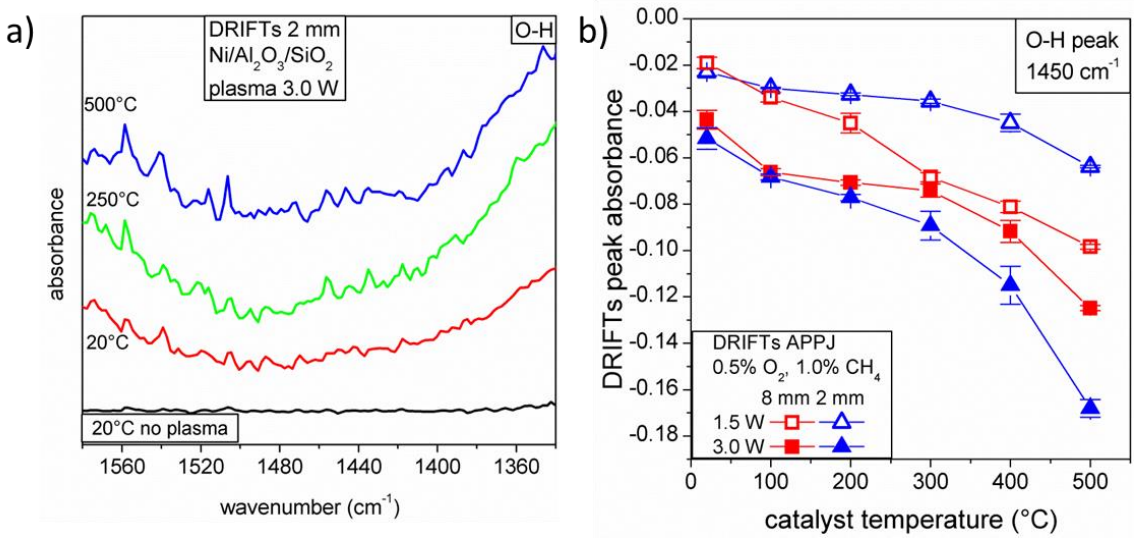

Figure 5.20: a) OH spectrum for no plasma, 2 mm 3 W case, 20, 250, and 500 °C showing the peak evolution b) extracted data from *In situ* DRIFTs of OH peak over 2 to 8 mm and 1.5 to 3.0 W plasma conditions.

The other two peaks of interest are the O-H peaks and the potential NiO peak. The behavior of the O-H peak at 1450 cm^{-1} raw spectrum for 2 mm 3 W plasma conditions is shown in Figure 5.20 a) and behaves similarly to the other O-H peaks. The extracted behavior of this peak over plasma distance and power is shown in Figure 5.20 b). In general the higher the temperature the more this peak is decreased signaling more water removed from the catalyst surface. Additionally increasing plasma power seems to increase the loss of signal for the O-H peak as well.

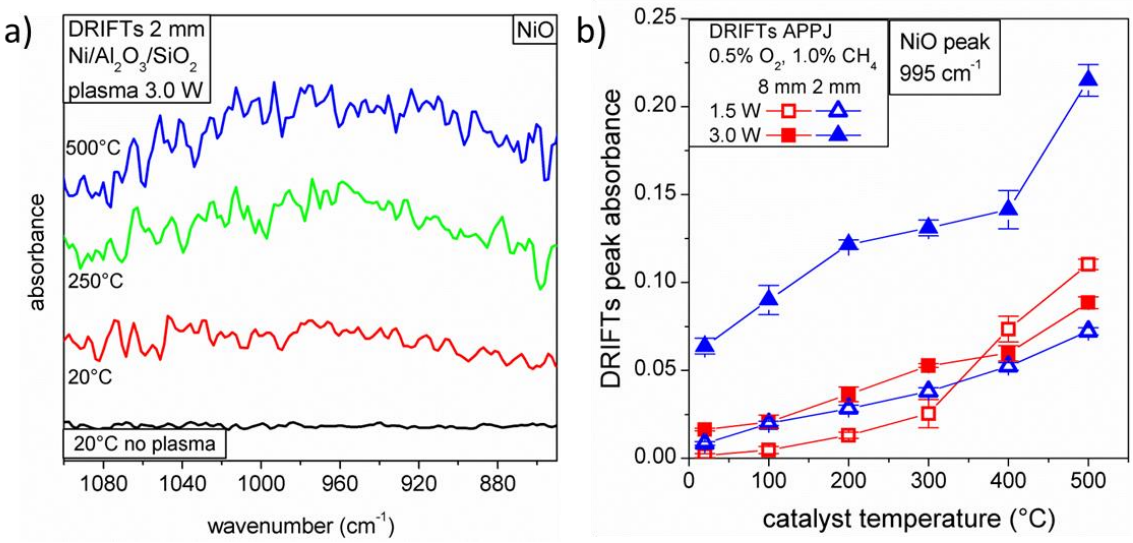

Figure 5.21: a) NiO spectrum for no plasma, 2 mm 3 W case, 20, 250, and 500 °C showing the peak evolution b) extracted data from *In situ* DRIFTs of NiO peak over 2 to 8 mm and 1.5 to 3.0 W plasma conditions.

The behavior of the NiO peak at 995 cm^{-1} raw spectrum for 2 mm 3 W case is over various temperatures is shown in Figure 21 a). The behavior of this peak shows almost the exact opposite behavior of the O-H peak and shows an increasing signal with increasing temperature and is shown in Figure 5.21 b) over plasma powers and distances. For most experimental conditions this peak seems only to scale with increasing temperature more than plasma power which makes sense since we see this peak form from only heating the catalyst without plasma. However, the 2 mm 3 W case does show a significantly higher absorption from this peak. If this peak is indeed NiO than this makes sense since the nickel will oxidize at a certain temperature but also highly reactive oxygen species produced by the plasma jet such as atomic oxygen[108] would also likely

oxidize the nickel so for strong enough plasma treatment this would increase the amount of oxidized nickel.

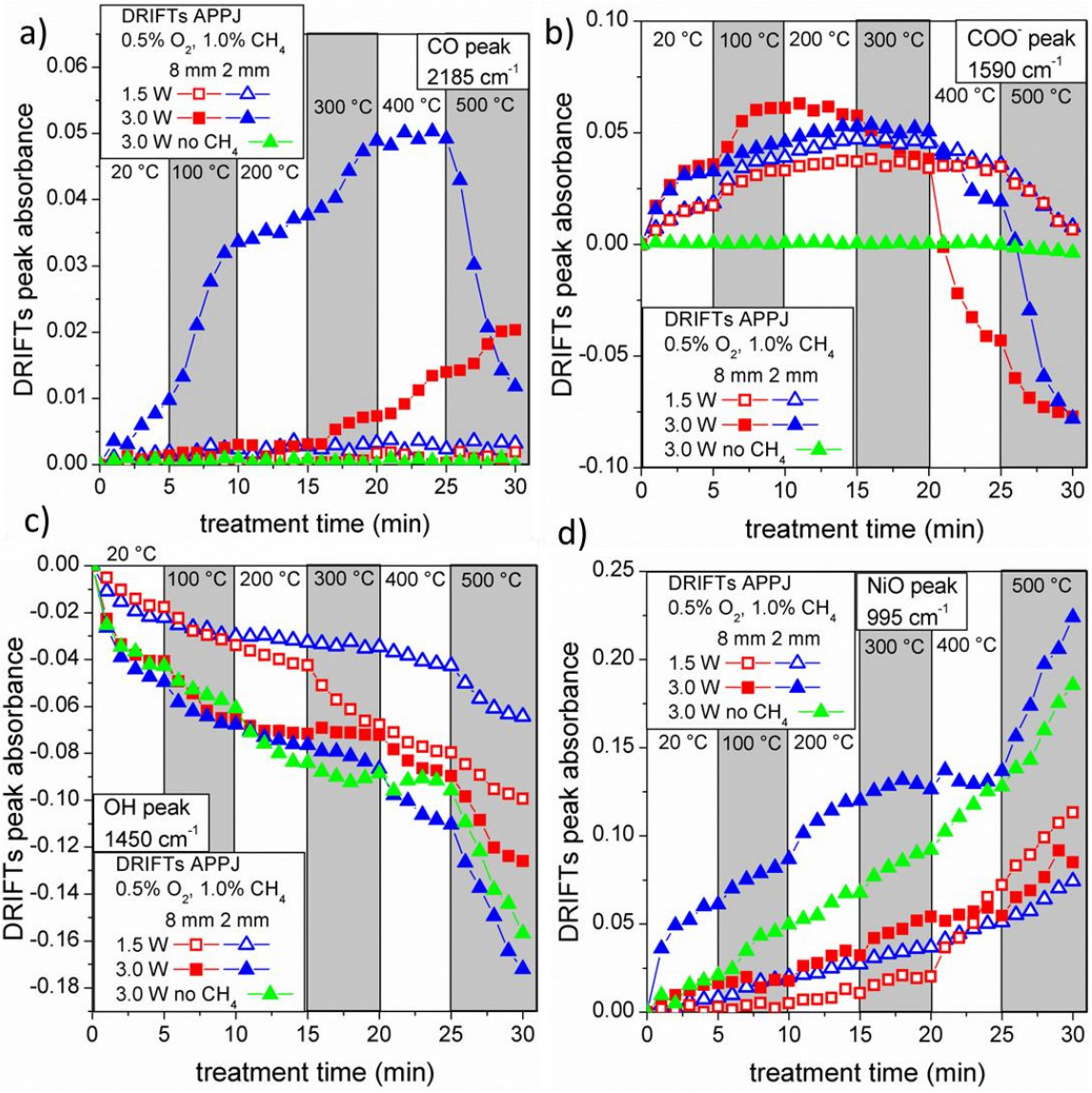

Figure 5.22: *In situ* DRIFTs peak absorbance of a) CO, b) unknown peak at 1590 cm^{-1}, c) OH peak, and d) NiO peak spectrum over time for 1.5 and 3 W at 2 and 8 mm.

Figure 5.22 shows the temporal behavior of each of these critical peak positions as the temperature is increased from room temperature to 500 °C. In Figure 5.22 a) we can see the formation behavior of the CO is fairly stable once it reaches 400 °C prior to dropping off quickly as soon at the temperature is increased up to 500 °C. Additionally we see that if treat the catalyst with plasma without any CH_4 present at 2 mm distance 3 W we do not see any CO production for any temperature. This affirms that the CO bonded to the surface is coming from a reaction of the methane with the oxygen present. Indeed we see a similar effect in Figure 5.22 b) for the unknown peak at 1590 cm-1. Here we see very little impact of the plasma when there is no CH_4 present except once reaching 500 °C where we see a very small reduction in the peak. Similar to the CO peak, this likely means that the production of this peak is tied to the carbon from the methane being decomposed in some manner.

In contrast to the behavior of these peaks the OH peak and the NiO peak behaviors, shown in Figure 5.22 c) and d) respectively, seems to behave similarly regardless of the presence of the CH_4 in the gas phase. This makes sense as the loss of water is likely based entirely on the amount of energy reaching the surface and the change of Ni into NiO relies primarily on temperature and reactive oxygen species reaching the surface. Additionally we can see how across all plasma treatment conditions the amount of NiO that forms takes a significant increase with time once the 500 °C state is reached.

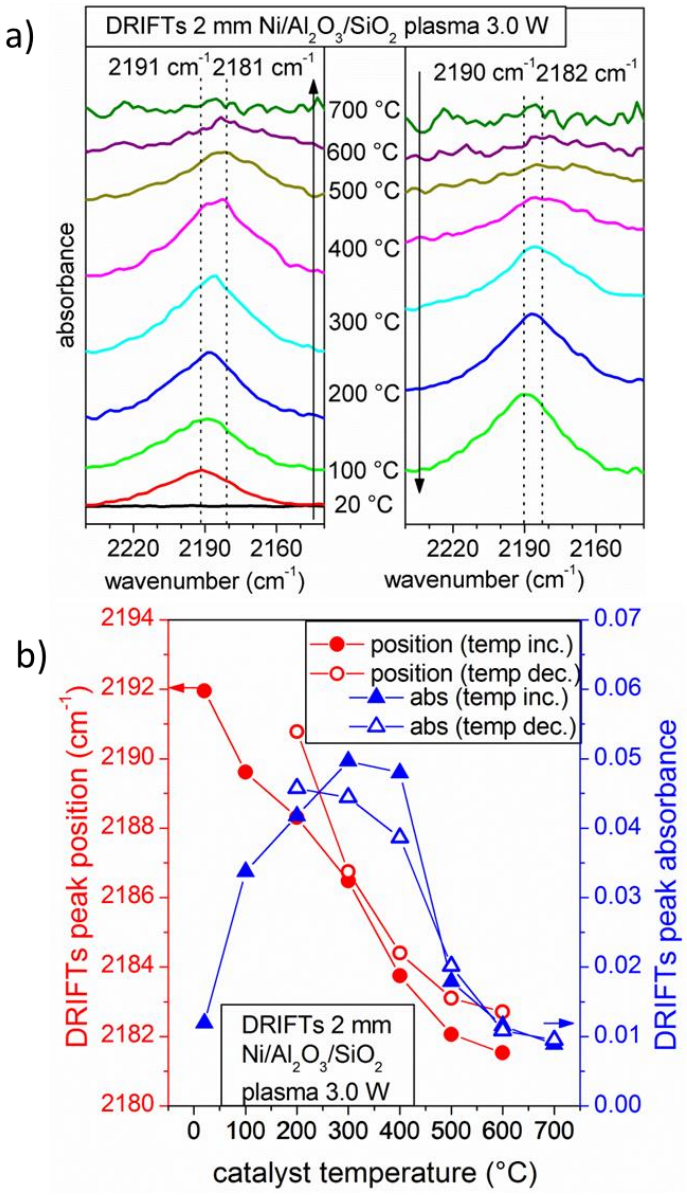

Figure 5.23: a) *In situ* DRIFTs and b) extracted data of 2 mm 3 W plasma conditions showing the CO spectrum for increasing and decreasing temperature up to 700 °C including peak position and peak absorbance.

The behavior of the creation and the removal of the CO bonded to the surface are shown in Figure 5.23 a). The extracted values of the central peak position and the peak absorbance of the CO peak at various temperatures increasing and decreasing is also shown in Figure 5.23 b). We see the creation of this CO peak to its maximum with increasing temperature at approximately 400 °C before it starts to quickly drop off until it is completely gone at 700 °C. From this temperature the catalyst is then cooled while the plasma exposure continues. The peak then seems to form more slowly as the temperature decreases with it maximizing at approximately 300 °C and then it is stable as the temperature drops below this point. However it is clear that there is a threshold point above which the CO is not stable on the surface and is removed and created by the plasma treatment of the catalyst. It is also interesting to see that the peak intensity of the CO peaks appears to shift to a lower wavenumber as the temperature is increased by approximately 10 cm^{-1}.

5.3.3 Discussion

The balance between methane decomposition and production of CO, CO_2, and H_2O seems to depend on numerous factors, more than what can be explored in this work alone. The contribution of the plasma alone is shown for the gas phase results but this is complicated once the catalyst is added in. CO for instance shows a significant increase from having the catalyst and plasma present at low temperature but then drops off at higher temperature. This may be due to the initial reactions in the plasma forming the CO to change to favor CO_2 at higher temperatures. It is also possible that the same amount is

being formed at all temperatures, but the high temperatures favor reactions to occur between CO and oxygen and water vapor in the gas phase. There is evidence of this with how the CO_2 increases significantly with temperature, much more so that H_2O. This could be because H_2O is a reactant and CO_2 is a product of the CO conversion reaction. The increase of CO from adding the catalyst and plasma together demonstrates clearly that while the plasma it critical for CO production, the plasma species combined with the catalyst materials also produced CO.

There are several things that can cause a shift in the peak position in FTIR spectrum as seen in figure 5.23. One paper investigating various species that can absorb onto metal substrates shows that CO absorbed on the metal surface can shift to a lower wavenumber and this shift correlates to an increase in the surface coverage of the CO on the metal surface.[133] Another work looking at CO absorption on nickel surfaces states how CO peak position is a function of dipole-dipole interactions and is therefore dependent on the substrate temperature as well as surface coverage.[134] In general, a lower wavenumber indicates more weakly bonded CO to the surface, which when due to surface coverage is because there are more CO molecules competing for the same surface electrons to bond with.[135] However, in our case it seems that we may have a weaker bonding state due to the increased surface energy since we simultaneously see a weakening DRIFTs CO signal which would mean less CO absorbed on the surface. It seems that for the CO production on the surface that below a certain plasma power there is simply no CO produced in the gas phase and therefore there is no CO to be bonded to the surface. However, once there is CO in the gas phase the surface must reach a certain energy state before CO can be bonded to the catalyst surface in a semi-permanent

manner. Once this occurs there is then another energy threshold above this where the CO can then be removed from the surface via a combination of plasma and thermal energy.

CO production as a product from has been investigated for plasma methane decomposition with catalyst materials other than nickel before. Lee et al. (2015) used a DBD style plasma source with a Pd based catalyst and saw a similar behavior of CO production to this work.[136] They see a distinct reduction in CO production with increasing temperature after a small increase up to 100 °C. It also increases with increasing plasma power which is similar to what we see here in our work.

There has been some significant that has started to investigate the interactions between plasma and catalyst materials. Stere et al. (2015) has investigated a Ag/Al_2O_3 catalyst for the decomposition of toluene and n-octane with a plasma treatment directly onto the catalyst material using a helium based ring style plasma source.[130] They attribute the peak seen at 2165 cm^{-1} to cyanide absorption on the surface and a NCO species absorbed on the surface which has a peak at 2260 cm^{-1}, however they include NO into their feed gas which complicates their system compared to our work since they are trying to simulate diesel exhaust gas. There has been other work looking at the effect of nickel catalyst in conjunction with a plasma reactor but they primarily look at the species produced and do no measurements of the catalyst surface after the plasma treatments.[137,138,139,140]

The most interesting observations that can be made from this work come from comparing the gas phase results to the surface results on the catalyst material. For instance, while we clearly see CO produced in the gas phase for all conditions above 2.5

W we do not see it absorbed on the surface for all of these conditions. In fact, for greater distance plasma treatments we see that CO is absorbed on the surface only after the temperature reaches 300 °C by which point the contribution of CO production from the catalyst seems to be greatly diminished. It is possible that the reason we see the difference between the temperature range for CO in the gas phase is that a certain point the surface becomes active enough to strongly bind the CO to the surface allowing us to see it using DRIFTs even after the plasma treatment has ended. However it is important to remember that CO that is removed from the surface often reacts with surface oxygen to form CO_2.[141] Therefore as the temperature reaches 500 °C and the CO starts to be removed from the surface by the plasma treatment, we may see a spike in CO_2 production and CO production. For the 2 mm 3 W case we actually see that there is still a significant amount of CO produced in the gas phase for this condition, especially compared to the case for plasma only. This could be signal from CO being removed from the surface by the plasma treatment as seen by the DRIFTs measurements.

There are several things that can influence the reactivity of a catalyst surface which can be further explored based on this work. One interesting point for future study is the effect of nickel loading on the reaction pathways of CO on the catalyst surface under plasma treatment. Previous work has extensively shown that for a nickel catalyst materials between 1.8 and 15% weight loading multiple reaction pathways can occur for CO absorbed on the catalyst surface, one for Ni sites surrounded by other Ni and the other for Ni sites surrounded by oxides of the support.[142] Another goal of the future of this work is to apply this technique to new catalyst materials where plasma may be able to make them more effective. For instance, we see that plasma at a high enough

temperature is able to remove critical species from the surface which means that catalyst materials which tend to have issues with carbon deposition due to their affinity for carbon bonding could be viable as catalysts. It may even be possible to create more reactive sites on a catalyst that has issues with not being reactive enough with carbon species. We see with plasma treatment of polymers that the plasma has enough energy to create reactive sites so it may be possible under the right conditions to do the same with certain metal surfaces.[81]

5.4 Conclusions

We have demonstrated a new methodology for investigating how plasma species interact with catalyst surfaces in the catalytic conversion of chemical compounds. We can monitor the surface changes *in situ* and compare them directly to changes we see in the gas phase. For this work specifically the reduction in methane by a plasma and catalyst system was studied and the products of this reaction including CO, CO_2, and H_2O were measured. CO production in the gas phase seemed to be primarily due to the plasma interacting with the catalyst surface and only is significant above a plasma power of 2.5 W. CO_2 production is controlled primarily by the catalyst temperature and H_2O production seems to be a product of both catalyst and plasma. The nickel catalyst surface changes significantly from both heating and plasma exposure. NiO formation occurs from heating of the nickel alone though can be accelerated by plasma treatment and additionally heating and plasma removes the water absorbed on the catalyst surface. An unknown peak which seems likely related to a carbon oxygen bonded species shows an

initial increase with plasma treatment and then a significant decrease once above a certain temperature and plasma power. This behavior is also seen with the CO absorption on the surface of the catalyst though we see both the formation and reduction occur over the range of plasma conditions, though the initial formation is likely due to the production of CO in the gas phase.

5.5 Acknowledgements

The authors gratefully acknowledge financial support by the US Department of Energy (DE-SC0001939) and National Science Foundation (CBET-1703211). I would like to thank C. Li, A. Pranda, K. Lin, L. Shafi, and T. Dabrow for their helpful discussions and support of the project.

Chapter 6: Conclusions and Future Work

Atmospheric pressure plasma has been shown to be very useful across many applications for its production of reactive species and energetic particles which can treat a wide variety of surfaces. This field has been rapidly expanding over the last decade and the need for a critical understanding of how plasma species interact with surfaces has become apparent. This work had advanced this field by using well understood experimental systems and materials in order to carefully breakdown what are the critical plasma produced species under certain conditions. This approach requires careful characterization of the plasma sources used which had led to numerous collaborations with the field of atmospheric pressure plasma science.

In chapter 2, we studied in detail the differences of a plasma source in direct contact with a surface where ions and electrons clearly play an important role vs a more remote condition where only longer lived reactive species dominate. For this work, a thin polymer film of photoresist material was used due to the wealth of knowledge about how the material reacts to plasma treatment for low pressure plasma processing conditions which can be compared directly to effects seen for atmospheric pressure plasma sources. When the plasma directly couples to a polymer surface there is an extremely high etch rate observed and the etching occurs in an uncontrollable pattern around the treatment area and the etching that does occur is non-uniform. However, for the remote treatment regime, the etching is significantly lower and appears to be uniformly treated over the plasma treatment area. The remote case etch rates and surface modifications are highly tunable based on the feed gas chemistry, the plasma source temperature, and how the plasma interacts with the local gas environment around the plasma source.

In chapter 3, the remote regime of plasma treatment of polymer films using a set of different plasma sources is investigated highlighting the importance of UV light for some sources compared with other. In particular we see that the high energy photons in the VUV range have a strong impact on modifying polymer surfaces. This effect is particularly pronounced by one particular kHz driven ring-APPJ plasma source. The modification seen is clearly highly directional and can occur through a MgF_2 filter which allows wavelengths of light through above 112 nm but stopped all other reactive species from traveling to treated area. The chemical changes seen in the photoresist material used are similar to those seen for VUV exposures using low pressure Ar plasma. The transmittance of this VUV light occurs over large distances due to the displacement of oxygen in the environment by the Ar flow from the plasma source. Oxygen in the environment strongly absorbs this VUV light and must be displaced to low levels prior to effect occurring. A simple model of the gas flow mixing with the ambient environment show that the environment oxygen diffuses into the plume based on the ambient concentration of oxygen. The type of plasma source is also shown to be critical to the production and transport of these VUV photons. Additionally, operating parameters such as feed gas chemistry drastically affect this VUV production as seen when oxygen is added directly to the feed gas and the VUV effect on the surface disappears entirely.

In chapter 4 another method is used to investigate the most critical reactive species produced for two different plasma sources. These sources have been shown to have very different interactions with polymers; the APPJ source etches polymers away easily while the SMD source only modifies the top surface of the polymer film without removing any material. The activation energy of polymer etching is measured by

changing the substrate temperature and is able to provide additional critical information about the important reactive species reaching a polymer surface. For a SMD source we find high activation energy compared with atomic oxygen etching suggesting less reactive species reaching the surface causing surface modifications. However, for the APPJ source we find that the activation energy changes over treatment distance, decreasing below the value expected for atomic oxygen as the jet gets closer to the surface. Additionally we find evidence of directional etching for the APPJ at close distances which becomes less directional for further distance treatments suggesting we have a contribution from high energy species at closer distances where there is no visible contact between the plasma plume and the polymer surface. The SMD source however shows no directionality for the etching that is caused on polymer films which occurs at elevated temperatures. Therefore we can immediately tell by looking at the effect on the surfaces that these two plasma sources have critically different mixtures of reactive species.

In chapter 5 we use the APPJ plasma source to enhance the reactivity of a nickel catalyst surface for the decomposition of methane gas. Here we find that the plasma itself is capable of causing some methane decomposition over a range of temperatures and the catalyst material alone is able to cause limited methane decomposition only at higher temperatures ranging up to 500 °C. However we clearly see some enhancement of catalyst decomposition by combining plasma and catalyst together. Additionally we see that CO is produced as a product of this reaction only under certain conditions where the plasma is above a power of 2.5 W, though this is enhanced by having the catalyst present. CO is also strongly dependent on temperature, showing a decrease in the amount of CO

produced at higher temperatures. The CO_2 produced by the plasma catalyst system is only significant at higher temperatures and does not seem dependent on the plasma. H_2O is the last product produced and we see that it increases with increasing temperature and increasing plasma power. The catalyst surface seems to be critically changed by both heating and plasma exposure separately. Heating the surface converts Ni to NiO and reduces the amount of absorbed water on the surface of the catalyst material. Plasma treatment however both induces and removes COO^- and CO species on the surface of the catalyst. At lower plasma powers and temperatures these species are deposited and at higher plasma powers and temperatures they can be removed again. CO in particular shows a strong bonding the catalyst surface but with strong enough plasma treatment at high enough temperature we see initially a shift to a lower wavenumber indicating a weakening of the surface bonding before complete removal of the CO. As temperature is decreased this CO is reformed again on the same catalyst surface with only a slight hysteresis. This leads to the possibility that plasma exposure of sufficiently high power can remove deposited carbon species on the catalyst surface which may block reactive sites allowing for future catalysis reactions to occur.

This research highlights the importance of the difference between plasma sources. Various plasma sources show critically different effects on surfaces based on design and this can lead to vastly different outcomes for applications. Even using the same plasma source in two different modes with the plasma touching the substrate or not touching the substrate can lead to very large differences in treatment effect. The flow of noble gas through a plasma jet allows reactive species to be transported over much larger distances than for dielectric barrier discharge style sources. However, this comes at the cost of

complexity of gas mixing with the local environment which we shown in chapter 3 can lead to the displacement of local oxygen leading to the transport of high energy photons. However, considerations such as frequency and voltage also play a role in this transmission which can differ between sources. Chapter 4 shows evidence for how a plasma jet source allows for very long-distance transport of ionized species as well, significantly past the visible plume. However, for the SMD style source the polymer interaction is completely different, and we see no evidence of directional species where there is a lack of directed noble gas flow to the surface.

The overall research that is presented in this work helps to further the critical understanding of how plasma sources interact with surfaces. Indeed, leveraging previous knowledge of how well characterized surfaces behave under certain conditions can lead to key understandings of what is happening in the plasma phase of the plasma surface interaction. This requires careful surface analysis and understanding. The example emerging field of plasma catalyst interactions is an excellent opportunity to use atomistic understanding to further the field as a whole. This work represents an initial step into the understanding but there are many things that can be investigated further.

There is significant future work that can be done based on the research foundation laid by this dissertation. In general having a single plasma source used for research across numerous facilities would lead to the best experimental results but this does not lead to optimization for the numerous plasma applications which may each require different conditions. Therefore, the most ideal case should be comparison of unique plasma sources for specific applications to other more standard plasma sources used across the plasma research field. This thesis uses this method, using the MHz pin-APPJ plasma jet

as a benchmark source which has been characterized through measurements done at several research institutions but also compares these results with other plasma sources where possible to determine how generic these effects are.

Additionally there are several specific questions raised within each chapter which could be further explored in the future. In chapter 5, different catalyst materials other than nickel will likely behave differently under similar plasma conditions. These will likely bond carbon species differently from nickel. This may allow for materials that previously are unable to be used for catalyst materials to be viable as the plasma changes the bonding affinity of certain critical species in the catalysis process. Additionally, the specific manner in which carbon bonding to nickel surfaces can be further investigated by using other characterization techniques such as ellipsometry. This allows for the monitoring of deposition of species on surfaces in real time as well as being able to monitor the conversion of nickel to nickel oxide. In chapter 4, further understanding of the specific reactive species being produced by the plasma source would be critical for the field of biological plasma interactions. Measurement of these species for the MHz pin-APPJ source using techniques such as mass spectrometry measuring ions would allow for correlation to the effects we see on polymer surfaces with the change of directionality. Ideally, this understanding would also be extended to other plasma sources that are jet style as these seem to be the sources where these species produce dominant effects. In chapter 3, the most critical fact discovered is that under certain plasma conditions and sources a significant amount of VUV photons may be incident on the surface. However, the fact that one plasma source may produce significant VUV photons but another does not means medical devices must be selected carefully to not

induce unwanted cell damage. These studies can help direct modeling of plasma sources and gas phase characterization as a limited number of reactive species are capable of causing certain surface effects seen based on the behavior of the plasma etching or modification of surfaces.

In conclusion, atmospheric pressure plasma has significant potential as a processor of electrical energy into useful chemical species and effects. The specific use of each plasma source must be studied carefully prior to use in applications, as small changes to a source design can lead to significantly different surface results. The contact of the plasma with a surface, the local gas environment, how the gas flow interacts between the plasma source and the surface, the dissipated power, and numerous other considerations should be taken into account when understanding new plasma applications to surfaces.

References

[1] A. Schutze, J. Y. Jeong, S. E. Babayan, J. Park, G. S. Selwyn, and R. F. Hicks, Ieee T Plasma Sci **26** (6), 1685 (1998).

[2] T. von Woedtke, S. Reuter, K. Masur, and K. D. Weltmann, Phys Rep **530** (4), 291 (2013).

[3] David B. Graves, J Phys D Appl Phys **45** (26), 263001 (2012).

[4] M. Keidar and I. I. Beilis, Plasma Engineering: Applications from Aerospace to Bio- and Nanotechnology, 359 (2013).

[5] T. von Woedtke, H. R. Metelmann, and K. D. Weltmann, Contrib Plasm Phys **54** (2), 104 (2014).

[6] D. B. Graves, Phys Plasmas **21** (8), 080901 (2014).

[7] M. Keidar, Plasma Sources Sci T **24** (3), 033001 (2015).

[8] J. Ehlbeck, U. Schnabel, M. Polak, J. Winter, Th von Woedtke, R. Brandenburg, T. von dem Hagen, and K. D. Weltmann, J Phys D Appl Phys **44** (1), 013002 (2011).

[9] T. Desmet, R. Morent, N. De Geyter, C. Leys, E. Schacht, and P. Dubruel, Biomacromolecules **10** (9), 2351 (2009).

[10] D. Merche, N. Vandencasteele, and F. Reniers, Thin Solid Films **520** (13), 4219 (2012).

[11] B. R. Locke, M. Sato, P. Sunka, M. R. Hoffmann, and J. S. Chang, Ind Eng Chem Res **45** (3), 882 (2006).

[12] B. A. Niemira, Annu Rev Food Sci T **3**, 125 (2012).

[13] E. C. Neyts, Plasma Chem Plasma P **36** (1), 185 (2016).

[14] E. A. J. Bartis, D. B. Graves, J. Seog, and G. S. Oehrlein, J Phys D Appl Phys **46** (31) (2013).

[15] E. A. J. Bartis, A. J. Knoll, P. Luan, J. Seog, and G. S. Oehrlein, Plasma Chem Plasma P **36** (1), 121 (2016).

[16] E. A. J. Bartis, C. Barrett, T. Y. Chung, N. Ning, J. W. Chu, D. B. Graves, J. Seog, and G. S. Oehrlein, J Phys D Appl Phys **47** (4) (2014).

[17] E. A. J. Bartis, P. S. Luan, A. J. Knoll, D. B. Graves, J. Seog, and G. S. Oehrlein, Plasma Processes and Polymers **13** (4), 410 (2016).

[18] K Fricke, K Duske, A Quade, B Nebe, K Schroder, KD Weltmann, and T von Woedtke, Ieee T Plasma Sci **40** (11), 2970 (2012).

[19] J. Y. Jeong, S. E. Babayan, A. Schutze, V. J. Tu, J. Park, I. Henins, G. S. Selwyn, and R. F. Hicks, J Vac Sci Technol A **17** (5), 2581 (1999).

[20] E. C. Neyts, K. Ostrikov, M. K. Sunkara, and A. Bogaerts, Chem Rev **115** (24), 13408 (2015).

[21] C. E. Stere, W. Adress, R. Burch, S. Chansai, A. Goguet, W. G. Graham, and C. Hardacre, Abstr Pap Am Chem S **247** (2014).

[22] J. L. Chen, X. Z. Zhou, L. Cao, and Y. D. Li, Natural Gas Conversion Vii **147**, 73 (2004).

[23] A. Aziznia, H. R. Bozorgzadeh, N. Seyed-Matin, M. Baghalha, and A. Mohamadalizadeh, J Nat Gas Chem **21** (4), 466 (2012).

[24] B. Pietruszka and M. Heintze, Catal Today **90** (1-2), 151 (2004).

[25] H. H. Kim, Y. Teramoto, A. Ogata, H. Takagi, and T. Nanba, Plasma Chem Plasma P **36** (1), 45 (2016).

[26] J. W. Lackmann and J. E. Bandow, Appl Microbiol Biot **98** (14), 6205 (2014).

[27] E. Stoffels, Y. Sakiyama, and D. B. Graves, Ieee T Plasma Sci **36** (4), 1441 (2008).

[28] M. Keidar, A. Shashurin, O. Volotskova, M. A. Stepp, P. Srinivasan, A. Sandler, and B. Trink, Phys Plasmas **20** (5) (2013).

[29] E. A. J. Bartis, P. S. Luan, A. J. Knoll, C. Hart, J. Seog, and G. S. Oehrlein, Biointerphases **10** (2) (2015).

[30] G. J. Pietsch and V. I. Gibalov, Pure Appl Chem **70** (6), 1169 (1998).
[31] A. Schmidt-Bleker, S. A. Norberg, J. Winter, E. Johnsen, S. Reuter, K. D. Weltmann, and M. J. Kushner, Plasma Sources Sci T **24** (3), 035022 (2015).
[32] W. Van Gaens, P. J. Bruggeman, and A. Bogaerts, New J Phys **16**, 063054 (2014).
[33] J. Vorac, P. Dvorak, V. Prochazka, J. Ehlbeck, and S. Reuter, Plasma Sources Sci T **22** (2), 025016 (2013).
[34] D. Ellerweg, A. von Keudell, and J. Benedikt, Plasma Sources Sci T **21** (3), 034019 (2012).
[35] S. Reuter, J. Winter, A. Schmidt-Bleker, D. Schroeder, H. Lange, N. Knake, V. Schulz-von der Gathen, and K. D. Weltmann, Plasma Sources Sci T **21** (2), 024005 (2012).
[36] S. Schneider, J. W. Lackmann, D. Ellerweg, B. Denis, F. Narberhaus, J. E. Bandow, and J. Benedikt, Plasma Process Polym **9** (6), 561 (2012).
[37] M. Teschke, J. Kedzierski, E. G. Finantu-Dinu, D. Korzec, and J. Engemann, Ieee T Plasma Sci **33** (2), 310 (2005).
[38] K. Wende, P. Williams, J. Dalluge, W. Van Gaens, H. Aboubakr, J. Bischof, T. von Woedtke, S. M. Goyal, K. D. Weltmann, A. Bogaerts, K. Masur, and P. J. Bruggeman, Biointerphases **10** (2), 029518 (2015).
[39] S. Q. Zhang, W. van Gaens, B. van Gessel, S. Hofmann, E. van Veldhuizen, A. Bogaerts, and P. Bruggeman, J Phys D Appl Phys **46** (20), 205202 (2013).
[40] S. Hofmann, A. F. H. van Gessel, T. Verreycken, and P. Bruggeman, Plasma Sources Science & Technology **20** (6) (2011).
[41] G. M. W. Kroesen, G. S. Oehrlein, and T. D. Bestwick, J Appl Phys **69** (5), 3390 (1991).
[42] X. Pei, X. Lu, J. Liu, D. Liu, Y. Yang, K. Ostrikov, P. K. Chu, and Y. Pan, J Phys D Appl Phys **45** (16) (2012).
[43] M. Laroussi and T. Akan, Plasma Process Polym **4** (9), 777 (2007).
[44] D. Pappas, J Vac Sci Technol A **29** (2) (2011).
[45] Mahmoud Y. Alkawareek, Qais Th Algwari, Garry Laverty, Sean P. Gorman, William G. Graham, Deborah O'Connell, and Brendan F. Gilmore, Plos One **7** (8) (2012).
[46] C. Q. Wang and X. N. He, Surf Coat Tech **201** (6), 3377 (2006).
[47] A. Sarani, A. Y. Nikiforov, N. De Geyter, R. Morent, and C. Leys, Appl Surf Sci **257** (20), 8737 (2011).
[48] Matthew J. Pavlovich, Hung-Wen Chang, Yukinori Sakiyama, Douglas S. Clark, and David B. Graves, J Phys D Appl Phys **46** (14) (2013).
[49] Katja Fricke, Stephan Reuter, Daniel Schroeder, Volker Schulz-von der Gathen, Klaus-Dieter Weltmann, and Thomas von Woedtke, Ieee T Plasma Sci **40** (11), 2900 (2012).
[50] T. C. Manley, Trans. Electrochem. Soc. **84**, 83 (1943).
[51] L. A. Rosenthal and D. A. Davis, Ieee T Ind Appl **IA-11** (3), 328 (1975).
[52] Xian-Jun Shao, Nan Jiang, Guan-Jun Zhang, and Ze-xian Cao, Appl Phys Lett **101** (25) (2012).
[53] R. Brandenburg, Z. Navratil, J. Jansky, P. St'ahel, D. Trunec, and H. E. Wagner, J Phys D Appl Phys **42** (8) (2009).
[54] H. M. Katsch, C. Manthey, J. A. Wagner, and H. F. Dobele, Surf Coat Tech **200** (1-4), 831 (2005).
[55] G. Park, H. Lee, G. Kim, and J. K. Lee, Plasma Process Polym **5** (6), 569 (2008).
[56] Yukinori Sakiyama, David B. Graves, Julien Jarrige, and Mounir Laroussi, Appl Phys Lett **96** (4) (2010).
[57] A. Yu Nikiforov, A. Sarani, and Ch Leys, Plasma Sources Sci T **20** (1) (2011).
[58] S. Schneider, J. W. Lackmann, F. Narberhaus, J. E. Bandow, B. Denis, and J. Benedikt, J Phys D Appl Phys **44** (29), 379501 (2011).

[59] T Dufour, J Hubert, N Vandencasteele, P Viville, R Lazzaroni, and F Reniers, J Phys D Appl Phys **46** (31) (2013).
[60] A. West, M. van der Schans, C. Xu, M. Cooke, and E. Wagenaars, Plasma Sources Science and Technology **25** (2), 02LT01 (2016).
[61] S. Engelmann, R. L. Bruce, T. Kwon, R. Phaneuf, G. S. Oehrlein, Y. C. Bae, C. Andes, D. Graves, D. Nest, E. A. Hudson, P. Lazzeri, E. Lacob, and M. Anderle, J Vac Sci Technol B **25** (4), 1353 (2007).
[62] A. J. Knoll, P. Luan, E. A. J. Bartis, C. Hart, Y. Raitses, and G. S. Oehrlein, Appl Phys Lett **105** (17), 171601 (2014).
[63] Z. M. Xiong and M. J. Kushner, Plasma Sources Sci T **23** (6) (2014).
[64] K. Fricke, H. Steffen, T. von Woedtke, K. Schroder, and K. D. Weltmann, Plasma Process Polym **8** (1), 51 (2011).
[65] T. Dufour, J. Hubert, N. Vandencasteele, P. Viville, R. Lazzaroni, and F. Reniers, J Phys D Appl Phys **46** (31), 315203 (2013).
[66] S. Zhang, A. F. H. van Gessel, S. C. van Grootel, and P. J. Bruggeman, Plasma Sources Sci T **23** (2) (2014).
[67] F. Weilnboeck, N. Kumar, G. S. Oehrlein, T. Y. Chung, D. Graves, M. Li, E. A. Hudson, and E. C. Benck, J Vac Sci Technol B **30** (3), 031807 (2012).
[68] P. Dube, M. J. Kiik, and B. P. Stoicheff, J Chem Phys **103** (18), 7708 (1995).
[69] C. Amsler, V. Boccone, A. Buchler, R. Chandrasekharan, C. Regenfus, and J. Rochet, J Instrum **3**, P02001 (2008).
[70] F. Weilnboeck, R. L. Bruce, S. Engelmann, G. S. Oehrlein, D. Nest, T. Y. Chung, D. Graves, M. Li, D. Wang, C. Andes, and E. A. Hudson, J Vac Sci Technol B **28** (5), 993 (2010).
[71] Comsol Multiphysics (COMSOL AB, 2010).
[72] S. Zhang, A. Sobota, E. M. van Veldhuizen, and P. J. Bruggeman, J Phys D Appl Phys **48** (1) (2015).
[73] D. J. Jin, H. S. Uhm, and G. Cho, Phys Plasmas **20** (8) (2013).
[74] W. F. Chan, G. Cooper, and C. E. Brion, Chem Phys **170** (1), 99 (1993).
[75] N. Vandencasteele and F. Reniers, J Electron Spectrosc **178**, 394 (2010).
[76] R. M. Walk, J. A. Snyder, P. Srinivasan, J. Kirsch, S. O. Diaz, F. C. Blanco, A. Shashurin, M. Keidar, and A. D. Sandler, J Pediatr Surg **48** (1), 67 (2013).
[77] M. Marschewski, J. Hirschberg, T. Omairi, O. Hofft, W. Viol, S. Emmert, and W. Maus-Friedrichs, Exp Dermatol **21** (12), 921 (2012).
[78] Y. F. Li, J. L. Zimmermann, and G. E. Morfill, New J Phys **14** (2012).
[79] A. J. Knoll, P. Luan, E. A. J. Bartis, V. S. S. K. Kondeti, P. J. Bruggeman, and G. S. Oehrlein, Plasma Process Polym **13** (11), 1069 (2016).
[80] B. T. J. van Ham, S. Hofmann, R. Brandenburg, and P. J. Bruggeman, J Phys D Appl Phys **47** (22) (2014).
[81] P. Luan, A. J. Knoll, H. Wang, V. S. S. K. Kondeti, P. J. Bruggeman, and G. S. Oehrlein, J Phys D Appl Phys **50** (3) (2017).
[82] P. S. Luan, A. J. Knoll, P. J. Bruggeman, and G. S. Oehrlein, J Vac Sci Technol A **35** (5) (2017).
[83] Y. Sakiyama, D. B. Graves, H. W. Chang, T. Shimizu, and G. E. Morfill, J Phys D Appl Phys **45** (42) (2012).
[84] R. D'Agostino, Flamm, D. L., Auciello, O., *Plasma Deposition, Treatment, and Etching of Polymers: The Treatment and Etching of Polymers*. (Burlington, Elsevier Science, 1990).
[85] U. Ali, K. J. B. Abd Karim, and N. A. Buang, Polym Rev **55** (4), 678 (2015).
[86] L. Eggert, J. Friedrich, and E. Merker, Acta Polymerica **42** (6), 289 (1991).

[87] J. Y. Jeong, S. E. Babayan, V. J. Tu, J. Park, I. Henins, R. F. Hicks, and G. S. Selwyn, Plasma Sources Sci T **7** (3), 282 (1998).
[88] Y. F. Li, T. Shimizu, J. L. Zimmermann, and G. E. Morfill, Plasma Process Polym **9** (6), 585 (2012).
[89] T. Maisch, T. Shimizu, A. Mitra, J. Heinlin, S. Karrer, Y. F. Li, G. Morfill, and J. L. Zimmermann, J Ind Microbiol Biot **39** (9), 1367 (2012).
[90] S. Engelmann, R. L. Bruce, F. Weilnboeck, M. Sumiya, T. Kwon, R. Phaneuf, G. S. Oehrlein, C. Andes, D. Graves, D. Nest, and E. A. Hudson, Journal of Vacuum Science & Technology B **27** (3), 1165 (2009).
[91] G. S. Oehrlein, R. J. Phaneuf, and D. B. Graves, J Vac Sci Technol B **29** (1) (2011).
[92] S. Iseni, S. Zhang, A. F. H. van Gessel, S. Hofmann, B. T. J. van Ham, S. Reuter, K. D. Weltmann, and P. J. Bruggeman, New J Phys **16** (2014).
[93] S. Zhang, A. Sobota, E. M. van Veldhuizen, and P. J. Bruggeman, Plasma Sources Sci T **24** (4) (2015).
[94] G. E. Morfill, M. G. Kong, and J. L. Zimmermann, New J Phys **11** (2009).
[95] J. Y. Jeong, J. Park, I. Henins, S. E. Babayan, V. J. Tu, G. S. Selwyn, G. Ding, and R. F. Hicks, Journal of Physical Chemistry A **104** (34), 8027 (2000).
[96] M. S. Kuo, X. F. Hua, G. S. Oehrlein, A. Ali, P. Jiang, P. Lazzeri, and M. Anderle, J Vac Sci Technol B **28** (2), 284 (2010).
[97] J. J. Hannon and J. M. Cook, J Electrochem Soc **131** (5), 1164 (1984).
[98] D. Zhang and M. J. Kushner, Journal of Vacuum Science & Technology a-Vacuum Surfaces and Films **19** (2), 524 (2001).
[99] F. Bastien and E. Marode, J Phys D Appl Phys **18** (3), 377 (1985).
[100] R. Dorai and M. J. Kushner, J Phys D Appl Phys **36** (6), 666 (2003).
[101] K Fricke, S Reuter, D Schroder, V Schulz-von der Gathen, KD Weltmann, and T von Woedtke, Ieee T Plasma Sci **40** (11), 2900 (2012).
[102] F. Weilnboeck, N. Kumar, G. S. Oehrlein, T. Y. Chung, D. Graves, M. Li, E. A. Hudson, and E. C. Benck, J Vac Sci Technol B **30** (3) (2012).
[103] A. Sobota, O. Guaitella, G. B. Sretenovic, I. B. Krstic, V. V. Kovacevic, A. Obrusnik, Y. N. Nguyen, L. Zajickova, B. M. Obradovic, and M. M. Kuraica, Plasma Sources Science & Technology **25** (6) (2016).
[104] T. Abuzairi, M. Okada, S. Bhattacharjee, and M. Nagatsu, Applied Surface Science **390**, 489 (2016).
[105] S. Hofmann, A. Sobota, and P. Bruggeman, Ieee T Plasma Sci **40** (11), 2888 (2012).
[106] J. W. Coburn and H. F. Winters, J Vac Sci Technol **16** (2), 391 (1979).
[107] W. J. Massman, Atmos Environ **32** (6), 1111 (1998).
[108] K Wende, P Williams, J Dalluge, W Van Gaens, H Aboubakr, J Bischof, T von Woedtke, SM Goyal, KD Weltmann, A Bogaerts, K Masur, and PJ Bruggeman, Biointerphases **10** (2) (2015).
[109] Y. B. Yun, D. J. Kim, S. M. Park, N. E. Lee, K. S. Kim, and G. H. Bae, J Electrochem Soc **154** (4), D267 (2007).
[110] S. Fujimura, K. Shinagawa, M. Nakamura, and H. Yano, Japanese Journal of Applied Physics Part 1-Regular Papers Short Notes & Review Papers **29** (10), 2165 (1990).
[111] J. C. Whitehead, Pure Appl Chem **82** (6), 1329 (2010).
[112] S. Tang, J. Lin, and K. L. Tan, Surf Interface Anal **28** (1), 155 (1999).
[113] U. Zavyalova, P. Scholz, and B. Ondruschka, Appl Catal a-Gen **323**, 226 (2007).
[114] X. Tu and J. C. Whitehead, Appl Catal B-Environ **125**, 439 (2012).
[115] Q. H. Trinh and Y. S. Mok, Korean J Chem Eng **33** (3), 735 (2016).

[116] B. Pietruszka, K. Anklam, and M. Heintze, Appl Catal a-Gen **261** (1), 19 (2004).
[117] E. C. Neyts and K. Ostrikov, Catal Today **256**, 23 (2015).
[118] Y. F. Guo, D. Q. Ye, and K. F. Chen, J Environ Sci-China **18** (2), 276 (2006).
[119] S. Y. Shang, G. H. Liu, X. Y. Chai, X. M. Tao, X. Li, M. G. Bai, W. Chu, X. Y. Dai, Y. X. Zhao, and Y. X. Yin, Catal Today **148** (3-4), 268 (2009).
[120] H. J. Gallon, X. Tu, M. V. Twigg, and J. C. Whitehead, Appl Catal B-Environ **106** (3-4), 616 (2011).
[121] X. Tu, H. J. Gallon, and J. C. Whitehead, Catal Today **211**, 120 (2013).
[122] L. Wang, Y. Zhao, C. Y. Liu, W. M. Gong, and H. C. Guo, Chem Commun **49** (36), 3787 (2013).
[123] Laurence S Rothman, Iouli E Gordon, Yury Babikov, Alain Barbe, D Chris Benner, Peter F Bernath, Manfred Birk, Luca Bizzocchi, Vincent Boudon, and Linda R Brown, Journal of Quantitative Spectroscopy and Radiative Transfer **130**, 4 (2013).
[124] X. E. Verykios, Int J Hydrogen Energ **28** (10), 1045 (2003).
[125] M. C. J. Bradford and M. A. Vannice, Appl Catal a-Gen **142** (1), 97 (1996).
[126] A. S. Adekunle, J. A. O. Oyekunle, O. S. Oluwafemi, A. O. Joshua, W. O. Makinde, A. O. Ogunfowokan, M. A. Eleruja, and E. E. Ebenso, Int J Electrochem Sc **9** (6), 3008 (2014).
[127] Y. Unutulmazsoy, R. Merkle, D. Fischer, J. Mannhart, and J. Maier, Phys Chem Chem Phys **19** (13), 9045 (2017).
[128] Phil Beauchamp, *Spectroscopy Data Tables: Infrared Tables*. (California State Polytechnic University, 2004).
[129] M. Nara and M. Tanokura, Biochem Bioph Res Co **369** (1), 225 (2008).
[130] C. E. Stere, W. Adress, R. Burch, S. Chansai, A. Goguet, W. G. Graham, and C. Hardacre, Acs Catal **5** (2), 956 (2015).
[131] B. Wichterlova, P. Sazama, J. P. Breen, R. Burch, C. J. Hill, L. Capek, and Z. Sobalik, J Catal **235** (1), 195 (2005).
[132] J. Shibata, K. Shimizu, S. Satokawa, A. Satsuma, and T. Hattori, Phys Chem Chem Phys **5** (10), 2154 (2003).
[133] C. Yang, Woll, C., Advances in Physics: X **2** (2), 373 (2017).
[134] J. Zarfl, D. Ferri, T. J. Schildhauer, J. Wambach, and A. Wokaun, Appl Catal a-Gen **495**, 104 (2015).
[135] K. S. Smirnov and G. Raseev, Surf Sci **384** (1-3), L875 (1997).
[136] H. Lee, D. H. Lee, Y. H. Song, W. C. Choi, Y. K. Park, and D. H. Kim, Chem Eng J **259**, 761 (2015).
[137] J. Kim, D. B. Go, and J. C. Hicks, Phys Chem Chem Phys **19** (20), 13010 (2017).
[138] A. A. Khassin, B. L. Pietruszka, M. Heintze, and V. N. Parmon, React Kinet Catal L **82** (1), 131 (2004).
[139] Y. R. Zhu, Z. H. Li, Y. B. Zhou, J. Lv, and H. T. Wang, React Kinet Catal L **87** (1), 33 (2005).
[140] W. Somers, A. Bogaerts, A. C. T. van Duin, and E. C. Neyts, Appl Catal B-Environ **154**, 1 (2014).
[141] K. H. Hou and R. Hughes, Chem Eng J **82** (1-3), 311 (2001).
[142] K. B. Kester, E. Zagli, and J. L. Falconer, Appl Catal **22** (2), 311 (1986).